Unravelling universal interferometers for ultra-precise probing of matter and realization of a new class of frugal photonic devices

Pooja Munjal

A thesis submitted for the partial fulfillment of

the degree of Doctor of Philosophy

Department of Physical Sciences,

Indian Institute of Science Education and Research Mohali

Knowledge city, Sector 81, SAS Nagar, Manauli PO, Mohali 140306, Punjab, India.

May, 2020

To my family.

Declaration

The work presented in this thesis has been carried out by me under the guidance of Dr. Kamal P. Singh at the Indian Institute of Science Education and Research Mohali. This work has not been submitted in part or in full for a degree, a diploma, or a fellowship to any other university or institute. Whenever contributions of others are involved, every effort is made to indicate this clearly, with due acknowledgment of collaborative research and discussions. This thesis is a bonafide record of original work done by me and all sources listed within have been detailed in the bibliography.

Pooja Munjal

In my capacity as the supervisor of the candidate's thesis work, I certify that the above statements by the candidate are true to the best of my knowledge.

Dr. Kamal P. Singh

Acknowledgment

I wish to express my sincere appreciation to my supervisor, Dr. Kamal P. Singh, who has the substance of a genius: he convincingly guided and encouraged me to be professional and do the right thing even when the road got tough. Without his persistent help, the goal of this project would not have been realized. I would like to thank him for giving me the best piece of career advice that, "Apply as if your work is the best and be prepared for the worst. Work hard and give your 100%, the success will automatically follow you." This advice has made me take decisions which have positively impacted my career. I was nominated in the top 4 for the Young Scientist Innovator Prize to represent India in the BRICS - Young Scientist Conclave held at Rio de Janerio, Brazil. I also won many accolades in national and international conferences. I would like to thank you for encouraging my research and for allowing me to grow as a research scientist. Your advice on both research as well as on my career have been invaluable.

I would also like to thank my committee members, Prof. Sudeshna Sinha, Dr. Sanjeev Kumar, and Dr. Sandeep Goyal for serving as my committee members even at hardship. I also want to thank you for letting my research time be an enjoyable moment, and for your brilliant comments and suggestions, thanks to you. I thank all the Professors at IISER Mohali for their teachings and help throughout. I express my gratitude towards Prof. J. M. Rost, Prof. N. D. Lai, Prof. Jiro Itatani, and Prof. David Hagan for their invaluable discussions during their visit to our lab.

I acknowledge the financial support provided by the IISER Mohali to carry out my research. I acknowledge the financial support (travel, and lodging) from Department of Science and Technology (DST), and Ministry of Science, Technology, Innovations and Communications, Brazil, to participate in the 4th BRICS Young Scientist Forum held in Rio de Janeiro, Brazil. I am thankful to Dr. Arvind from DST for all his guidance and support during and after the BRICS conference. I would also like to acknowledge CSIR and SPIE for the financial assistance to participate in the conference Photonics Europe held in France. I acknowledge the assistance and discussions from all the current and the past members of the Femtosecond Laser Lab, Dr. M. S. Sidhu, Dr. Ankur Mandal, Komal, Sunil, Biswajit, Shivali, Akansha, Ayush, Yateendra, and Gopal.

I would also like to acknowledge the support by Ms. Neetu Sahni. She was just a call away whenever we needed. I thank her for all the parties that she has thrown for us and for the delicious home cooked food that she prepared for us.

This thesis goes incomplete without thanking my school teachers who have been the building blocks of my career. I would like to thank Mrs. Basanti Gupta (my Principal), Ms. Suma Ghosh, Ms. Kiran Bala, Ms. Mamta Arora, Ms. Shagun Shukla, Ms. Renu Verma, Ms.

Indu Kaushik, Mr. Milind Khachane, Ms. Rekha, Ms. Raj Verma, Ms. Seema Chawla, and all the other teachers who have taught me, for all your blessings and teachings. I am sincerely thankful to the entire team of Fiziks, Mr. Atul Gaurav, Dr. Sugam Kumar, Dr. Vivek, and Dr. Alok, for developing my initial interest in Physics and always encouraging me to ask questions whether small, or stupid, or good. It's only because of them that I got into IISER for a Ph.D

I am extremely grateful that I joined IISER Mohali where I met someone who made this journey even more pleasant, with whom I can discuss anything and everything. I am blessed to have Ankit in my life who has always stood by me through thick and thin. I admire him for his strive to learn new things and impart the knowledge to his near and dear ones. Almost everyday I learn something new from him be it Physics, or general knowledge, or some new package/technique in programming. Any journey is enjoyable when you are surrounded by many beautiful people called Friends. I would start with my first ever friend, Chandan, whom I have known since I started my schooling. He has been more like a brother and my partner in crime too. He has been very supportive and has always lend me an ear whenever I needed him. I am thankful to my friend Divya for her interest and reviving my failing spirits many times. She's my sister from another mother. I am also thankful to Ashu, Monisha, Urvashi, Mia Filić, Juliana, Liliana, and Ming for sticking by me through all the time.

I am also grateful to have known Vaibhav, Poonam, Anvi, Ritu, and Vivek who are just wonderful people both from within and outside. I am glad to be friends with all the members of the BRICS family, Aman, Updesh, Afreen, Priyanka, Neha, Ravi, Nivetha, Rohit, Anchal, Charu, Dipak, Rajan, Meenakshi, Mohan, Priyabrata, Seenivasan, and Prerna.

During my Ph.D. I have come across so many amazing people, and I would like to acknowledge the support of a few awesome friends I have made here. My closest friends with whom I have had unforgettable fun Dahlia, Yogesh, Avinash, Arnob, Sudhanshu, Gaurav, Satyam, Swagatam, and Priyanka. They have made each day here more enjoyable. Playing and chatting with them acted like a relaxing therapy which provided me with energy to sustain my enthusiasm over all these years. I have also had the pleasure of being friends with Vishavdeep, Shailesh, Jyotsna, Nupur, Shalini, Sujoy, Jaskaran, Rajneesh, Samridhi, and Ayushi.

I wish to acknowledge the support and great love of my family, my parents Ms. Ritu Munjal, and Mr. K. N. Munjal, my other parents Ms. Veena Devi, and Mr. Krishan Kumar, my sister Richa Munjal, my brothers Dipanshu Munjal and Sunny Munjal, my brother-in-law Shravan, sister-in-law Shweta, my niece Bhumika, and my nephew Heian. This thesis is dedicated to all my family members. They kept me going on and this work would not have been possible without their input. Their unconditional love and support has sustained me

through my graduate work. I am sure that a completion of this work would come as a great relief to them as it is for me.

Abstract

In this thesis, we show a compact single-lens interferometer enabling a real-time self-calibrating picometer resolution on arbitrary surfaces. We demonstrate the performance of our interference lens (iLens) by first obtaining high-contrast fringes from a wide variety of common surfaces such as paper, cloth, cardboard, plastic, human skin, silk fiber, etc., and then we demonstrate a single-pixel based self-calibrated measurement of local surface displacement with sub-20 pm precision induced by another pump laser, for example. We have analyzed optimal design of our universal interferometer and show that it can be 3d printed for stand-alone precision applications offering advantages over conventional interferometers.

Our compact iLens interferometer enables a new class of frugal optical devices matching or outperforming their state-of-the-art counterparts. We demonstrate three examples: (i) a paper-based picogram weighing balance which is 1000 times more precise and faster compared to a seven digit advanced digital balance, (ii) a cloth or hair based broadband acoustic sensor, and (iii) direct measurement of thermal diffusivity of various fragile biological surfaces. Furthermore, the iLens interferometer allows probing nanosecond dynamics of candle-flame plasma and micro-liter liquid droplets suggesting its wide applications in four phases of matter.

Using structured light, in particular with light containing orbital angular momentum (OAM) and a cylindrical iLens, we devise a compact tiwsted interferometer with picometer scale. We exploited the phase-structure of OAM, a feasibility of real-time noise-compensation is demonstrated with our interferometer. Besides, cylindrical lens We also show ultrafast fabrication of large-area, high-fidelity surface nano-structuring of solid surfaces which could serve as optical components in optical devices.

Finally, we discuss the future perspectives of our iLens probes as a generic ultra-sensitive tool to investigate dynamics properties of solids surfaces, complex liquids and gel, as well as precision fundamental physics experiments on nature of photons momentum in medium.

Publications

- **P. Munjal**, V. Vashisht and K. P. Singh, “iLens interferometer probing nanoscale plasma dynamics,” Asian Journal of Physics, 2020. (Accepted)
- **P. Munjal** and K. P. Singh, “Optically probing picometer resolved photo-dynamics of solid surfaces,” *URSI Radio Science Bulletin* **2019**(370), 2019.
- **P. Munjal** and K. P. Singh, “A single-lens universal interferometer: towards a class of frugal optical devices,” *Applied Physics Letters* **115**(11), 2019.
- B. Panda, M. S. Sidhu, **P. Munjal**, S. Sokhi, and K. P. Singh, “Time-resolved nano-Newton force spectroscopy in air and vacuum using a load cell of ultra micro-balance”, *Review of Scientific Instruments*, **90**(4), 2019.
- M. S. Sidhu, **P. Munjal**, and K. P. Singh, “High-fidelity large area nano-patterning of silicon with femtosecond light sheet”, *Applied Physics A*, **124**(1), 46, 2018.
- **P. Munjal**, K. Chaudhary, and K. P. Singh, “Noise self-compensating signal-amplifying twisted interferometer for solid surfaces”. (To be submitted)
- **P. Munjal** and K. P. Singh, "Compact interferometer cavity for sub-nanoscale fluid deformation". (Under preparation)

Patent

- **P. Munjal** and Kamal P. Singh, “An interferometer and method for producing interference pattern”. Filed Indian Patent #201811004064.

List of conference papers

- **P. Munjal** and K. P. Singh, "Picometer-resolved universal single-lens interferometer unveiling ultraprecise frugal devices (Conference Presentation)", *International Society for Optics and Photonics* **11352**, 2020.
- **P. Munjal** and K. P. Singh, Optically probing sub-nanometer photo-dynamics of solid surfaces, In 2019 URSI Asia-Pacific Radio Science Conference (AP-RASC) (pp. 1-3), IEEE, 2019.
- **P. Munjal**, V. Vashisht, and K. P. Singh, Picometer scale single-shot photo-mechanical dynamics of candle flame plasma, In 2019 URSI Asia-Pacific Radio Science Conference (AP-RASC).

Table of contents

List of figures

List of tables

Chapter 1

General Introduction

In 1717 Issac Newton first demonstrated interference pattern created by reflection of light between two smooth surfaces, a spherical surface and an adjacent touching flat surface, known as Newton's rings. Around 1803, Thomas Young described his famous double-slit experiment with white sun-light to show the wave properties of light. An arrangement similar to Newton's ring was proposed by Fizeau about 1862, that is still used today, to precisely measure curvature of various surfaces. While these interferometers played a key role to understand wave or corpuscular nature of light, in 1887, Michelson-Morley designed a new interferometer and obtained the famous null result on the existence of ether [1]. These examples led development of a wide variety of ultra-precise optical interferometers in the 19^{th} century, such as Jamin interferometer (1856) [2], Mach-Zehnder interferometer (1890) [3], and Fabry-Perot interferometer (1899) [4]. In addition, the invention of lasers around the middle of 19^{th} century made the interferometers as tools with unmatched precision for various fundamental and technological applications [5–7], including detection of gravitational waves with Michelson and Fabry-Perot interferometers [8, 9].

Modern interferometers exploit coherence of laser light to performs precision measurements. In spite of their immensely distinct designs, the interferometers are commonly based on the superposition of two or more beams. Generally, an incoming light is split into two parts, *viz.* reference beam and object (or measurement) beam, and then recombined together to produce the fringes. In order to obtain high-quality fringes, interferometers require multiple high quality optical components, a beam splitter, series of mirrors, lenses, and a smooth optical quality sample. In addition, a CCD camera, or a photo-detector is used to record and analyze the fringes. Depending upon the design and the application these interferometers may require additional optical components as well as sophisticated signal processing algorithms. However, the necessary requirement of multiple optical components not only makes most interferometers bulky devices but also make them sensitive to align and stabilize against the

various non-fundamental mechanical and thermal noises [6, 10, 11]. Although monolithic assembly of interferometer allowed miniaturization, it is challenging to devise a compact interferometer capable of achieving real-time picometer scale precision.

Most existing interferometers rely upon the fringe formation from smooth optical quality surfaces, such as of the reference mirror. If the smooth surface is replaced by a rough test surface, in Michelson interferometer for example, no fringes are formed on the screen due to several following reasons. The rough surface randomly scatters the light in all the possible directions, i.e. a speckle field is formed on the screen. It then becomes difficult to collect light to form high-contrast interference fringes. Additional components are required to collect light, such as in Zygo's equal path white-light interferometer with transmission sphere (a combination of lenses), which leads to feeble fringes from rough surfaces [12]. Another key problem in performing interferometry with arbitrary surfaces is how to calibrate the fringes to achieve picometer precision, which is beyond the reliable displacements caused by state-of-the-art piezo-stages.

Although several promising optical techniques have been devised to probe rough or nano-patterned surfaces, for example, electronic speckle pattern interferometry[13–15], diffuse optical tomography and imaging [16], interferometric scattering microscopy (iSCAT) [17–19], two-wavelength heterodyne speckle interferometer [20], and holography [21]. The vertical scanning white-light interferometry, based on Mirau or Zygo interferometers, has been able to probe patterned surfaces by processing white-light fringes [6, 22]. Besides being multi component systems most of these interferometric methods use optimized protocol, whereby dynamic fringes are recorded with a camera, which are analysed frame by frame using a dedicated processing toolkit to filter out the unwanted noises, thus, limiting the detection speed. Moreover, the precision achieved by such approaches is limited by the pixel size of the camera and its frames per second. One may wonder if it is possible to design an interferometric technique to directly probe arbitrary rough surface with the picometer precision in real-time.

On the other hand, the applications of universal interferometry to advance frugal science, i.e., to realize low-cost devices analogous to foldscope or paper-fuge has remained elusive [23–25]. Application of precision interferometers for arbitrary surfaces could open new path in devising the ultra-precise frugal optical devices, using paper, cloth or hair etc. Furthermore, such techniques can measure photo-mechanical dynamics on solid surfaces, candle flame plasma, and liquid samples, in real time with picometer precision.

In this regard we focus on the following questions that we attempt to answer in this work:

- Despite the recent progress in the design of present day interferometers, there still remain a few "stringent prerequisites" associated with obtaining interference fringes

which limit its potential. For instance, most interferometers require multiple high-quality optical elements, which demand tedious alignment and stabilization against various non-fundamental noises for precision measurements. We wonder if it is possible to design an interferometer with just one component that would considerably simplify alignment and robust stabilization. If such an interferometer could be designed, is it possible to develop a simple analysis procedure for real-time detection of sample displacement without the need of any external calibration standard.

- Most of the conventional interferometers work best with optical quality surface and have difficulty with common rough surfaces such as paper, cloth, unpolished metal surfaces, etc. Though there are many techniques to do precise measurements with rough surfaces, they require additional optical attachments. Importantly, most of these technique do not render interferometric precision on in situ rough surfaces. Thus, one may ask, is it possible to design a universal interferometer which produces high contrast fringes with arbitrary solid surfaces, including for plasma and liquids. A related question would be then how to analyze the fringes obtained from common surfaces for picometer resolved measurements.

- While advancement in modern interferometry has allowed unparalleled precision in fundamental measurements and for various technical applications. Considerable efforts have been invested in design and development of inexpensive frugal optical instruments without compromising the precision can prove to be a boon. Several examples exist such as a paper based foldable microscope (foldscope) or a paperfuge [23, 24]. However, it is still not possible to design ultra-sensitive frugal optical instruments using optical interferometers. How can one design frugal optical instruments for different applications, for example in weighing and force sensing using everyday items with sensitivity matching with their commercial counterparts at low-cost.

- Most optical interferometers exploit a Gaussian laser beam. With the recent development in capability to create structured light, such as light carrying orbital angular momentum or light sheet, there is a great interest in exploiting structured light in an interferometer. In this regard, one may wonder how can one design compact interferometers for twisted light. What are the advantages of such interferometers over the ones that use the Gaussian beam? One may also wonder, if light-sheets offer any capability in controlling light-matter interaction for nano-structuring solid surfaces.

To answer these questions we have chosen the following thesis plan:

In the second chapter, we unravel a universal single interference lens (iLens) interferometer. We first present the key idea that allows us to combine three different functions of an

interferometer into a single-lens thus making the interferometer compact. We present theoretical analysis on the formation of fringes and analyze the optical beam-splitting coating for producing high-contrast fringes with various surfaces. We then experimentally demonstrate our interferometer on a wide variety of common surfaces and establish a self-calibrating picometer resolution in real-time. We also show that our interferometer can be 3D printed for various stand alone applications.

The third chapter deals with various applications of iLens interferometer. We demonstrate that iLens enables a new class of frugal optical devices that are fabricated with common materials such as paper, cloth, human hair. Three illustrative examples of the device are shown for measurement of weight, acoustic vibration, and force using paper, cloth and human hair with matching or superior precision than the state of the art counterparts.

We also demonstrate applications of iLens interferometer in fundamental measurements. For example, we show that iLens interferometer enables measurement of properties of candle flame plasma with picometer precision and to probe intriguing phenomenon arising due to the interaction of ns pump laser with candle flames. The applications of iLens in measuring properties of fluids is also demonstrated.

The fourth chapter is aimed at exploring the potential of twisted light in the cylindrical iLens interferometer. We theoretically design and demonstrate a cylindrical iLens that makes a compact twisted iLens interferometer. The interferometer produces a daisy-flower pattern and we show how this can be used for picometer resolved measurements. We also introduce a concept of real-time differential noise-cancellation by exploiting the unique phase-structure of the twisted light. We analysis different noises and also show that simultaneous multiple-point measurement leads to real-time noise averaging. Finally, we discuss a related application of ultrafast light-sheet produced by a cylindrical lens in large-area nano-patterning of solid surfaces.

In the end of this thesis, in **chapter five** we present summary of our results and discuss future directions in which this work can possibly be extended.

Chapter 2

A Universal Single-lens Interferometer

2.1 Introduction

Over the past centuries, a wide variety of ultra-precise optical interferometers have been invented for various fundamental measurements and for a variety of technological applications [1, 4, 5, 3, 6], including null-result on the presence of ether to recent detection of gravitational waves with Michelson and Fabry-Perot interferometers [8, 9]. Modern interferometers are sophisticated devices enabling ultrahigh precision in various applications such as surface tomography, material properties, etc. The precision in these interferometers comes at a cost of multiple high-quality components such as beam splitter, reference mirror, collimator optics, and optical quality test-surfaces.

In addition, most interferometers demand tedious alignment and stabilization of its multiple components against non-fundamental mechanical and thermal noises [6] to achieve sub-nanometer resolution. However, common materials around us such as paper, cloth, rubber, skin, etc., lack optical quality finish and therefore, cannot presumably be used directly to build optical interferometers. In other words, the standard interferometry cannot be directly applied to in situ common surfaces. It will be of broad interest if one can find new approach to achieve interferometric precision with such common surfaces.

There are many challenges to extend applications of optical techniques to arbitrary surfaces (paper, rubber, plastic, bio-materials viz. flower, leaf, skin, etc.). For example, how to efficiently collect back-scattered light from the rough surface, how to calibrate the interferometer, and how to develop simple computational strategies for analysis of interference pattern in real-time without the requirement for sophisticated toolkit.

Although, several promising optical techniques have been devised to probe rough or nano-patterned surfaces, for example, electronic speckle pattern interferometry [13], diffuse optical tomography and imaging [16], interferometric scattering microscopy(iSCAT) [18, 19], and

holography [21]. The vertical scanning white-light interferometry, based on Mirau or Zygo interferometers, has been able to probe patterned surfaces by processing white-light fringes [6, 22]. The multi-component geometry of these techniques makes them difficult to align and stabilize them against various non-fundamental noises. Moreover, the precision and speed in such techniques is limited by the pixel size of camera used to record the interferogram, scanning speed of the sample or the signal-processing algorithms. In white-light Zygo interferometer, a so-called transmission sphere [12] comprising of two or more lenses, is used in conjunction with the interferometer to obtain interference fringes from rough surfaces. One may wonder if it is possible to devise a compact interferometer capable of achieving real-time picometer scale precision by direct interferometry on arbitrary surfaces without requiring any sophisticated measurement toolkit.

In this chapter, we demonstrate the ultimate miniaturization of interferometers by integrating the three essential functions of an interferometer provided by a beam splitter, a reference mirror, and light collection optics into a single interference-lens (iLens) enabling stable, high-contrast fringes with various surfaces including paper, plastic, wood, metal, rubber, human skin, hair, etc. The fringes obtained with these surfaces appear randomly oriented and contain the information about the sample surface structure. We will validate our setup for different rough samples from our day-to-day life including paper, rubber, plastic, hair, skin, etc. Analyzing the high-contrast fringes from our universal interferometer one can achieve a real-time precision of sub-20 *pm* ($\sim \lambda/30000$) with a simple detection of interference intensity using a high-speed photodiode. The compactness of our iLens interferometer allows us to further miniaturize the setup by 3-D printing for stand-alone portable applications.

2.2 Schematic of Experimental set-up

The key element of our compact interferometer is the iLens which when combined with a sample surface forms a functional interferometer. The iLens is a bi-convex glass lens whose one side is partially silver-coated (denoted by red-surface). iLens is a three-in-one component which combines functions of three basic optical elements required in any interferometer, as shown in Figure 2.1(a). (i) It acts like a beam-splitter, wherein, it splits the incoming light beam into two beams, *viz.* reflected and transmitted beam. (ii) The partially coated side of the lens also act as the reference mirror of the interferometer, hence the light reflected from this surface is our reference beam. (iii) It collects a small portion of the back-scattered beam from the sample, forming the object beam. Hence, the last function performed by the iLens is of the light collector. In effect, the iLens with the sample surface becomes a compact interferometer which can produce high contrast interference fringes with a wide variety of

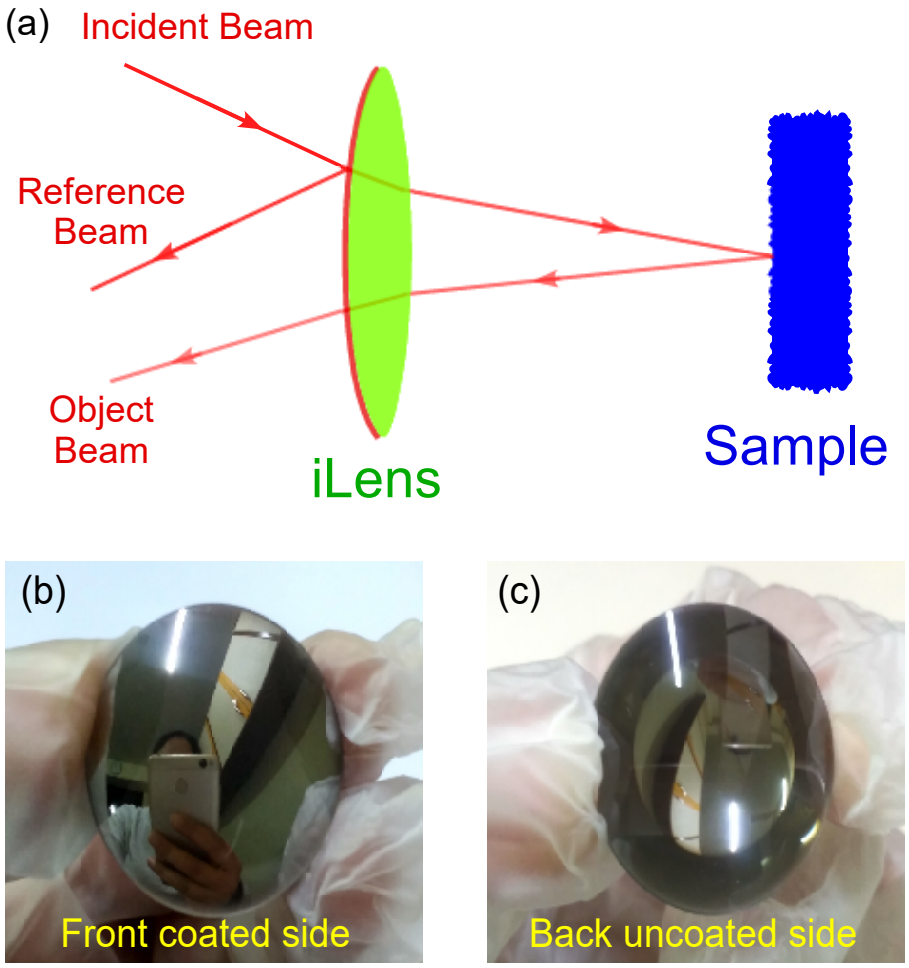

Fig. 2.1 **Key components of single-lens interferometer.** (a) The figure shows the interference lens (iLens) which performs the functions of a beam splitter, reference mirror, and light collector in the interferometer. This when combined with any rough sample forms an interferometer. (b,c) the front coated and the back uncoated side of the iLens respectively.

surfaces. The real picture of the front coated and the back uncoated side of the iLens is shown in Figure 2.1(b-c).

Figure 2.2 shows the schematic diagram of the iLens interferometer set-up. The iLens was chosen such that its front surface was partially silver-coated. We used a low power He-Ne laser as the light source. The incident He-Ne laser (10 mW, $\lambda = 632$ nm, and $1/e^2$ full waist $\simeq$ 1.0 mm) is partially reflected from the coated surface of the iLens (reference beam), and the transmitted beam goes to the sample from where it is scattered in all the possible directions (object beam). This beam is then collected by the iLens, where it is superimposed collinearly with the reference beam to produce a high-contrast interference pattern on the screen. In effect, the iLens with any test surface forms a single-lens interferometer.

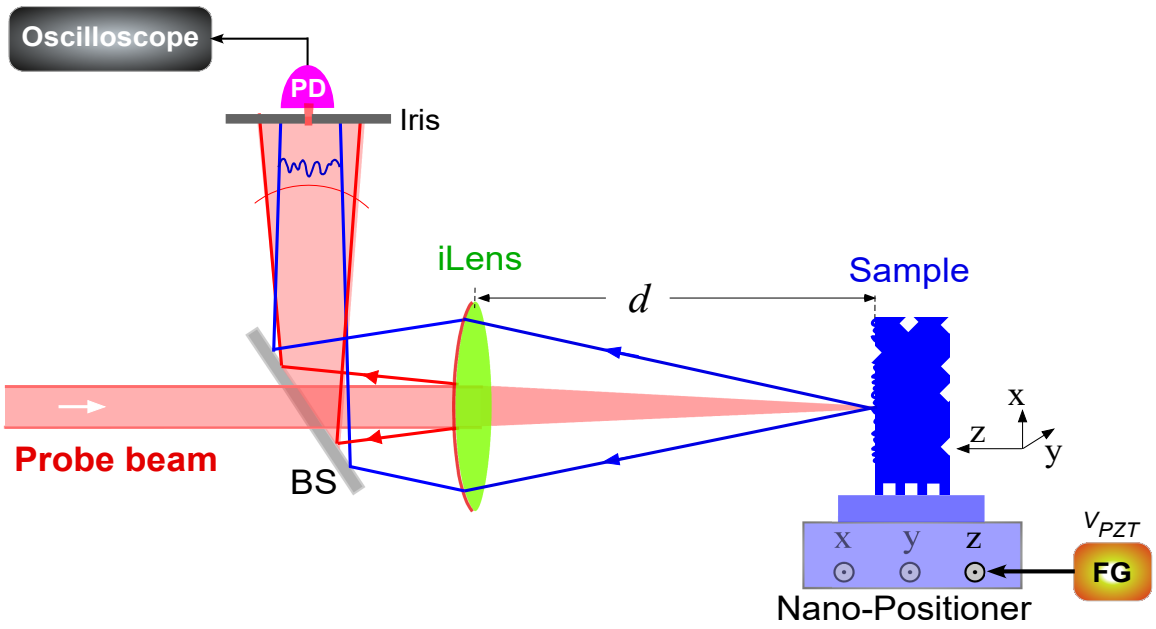

Fig. 2.2 **Schematics of iLens interferometer.** An iLens produces high-contrast structured fringes from a surface using a low-power He-Ne probe laser (10 mW, $\lambda = 632$ nm). The z-position of the sample from the iLens, $d(t)$, is controlled by a piezo-positioner driven by V_{PZT} from a function generator (FG). The central intensity of fringes is detected with a photodiode (PD).

The sample was mounted on a 3-axis nano-positioner piezo stage (Thorlabs) with 20 μm travel range to introduce an optical path difference in the object arm of the interferometer. An arbitrary function generator (Keysight 33500B) was used to drive the piezo stage with a minimum possible signal amplitude of 1 mV. Application of a voltage to piezo-stage changes the iLens to sample distance thus causing the interference fringes to evolve. Since, we focus on using our common-path interferometer for measuring z-displacement (shown in Figure 2.2) we moved the sample in this direction only by providing a voltage to the z-axis of the piezo stage. The dynamic interference pattern was then recorded with a low-cost webcam and a CCD camera at 30 fps. In addition, the fringe intensity was detected using a photodiode (1 ns rise time, Thorlabs DET10A) through an iris and observed on an oscilloscope (Tektronix). The intensity at a point on the evolving interference pattern follows the Michelson-like dependence as will be derived theoretically in the next section.

In order to use iLens with different surfaces of varying reflectivity and color, we fabricated many iLenses having different coating thickness in order to vary ratios of reflected to transmitted intensity (50:50, 30:70, 20:80, 60:40), of diameters from $10-25.4$ mm and of focal lengths ($f = 12, 25, 50$ mm). A detailed discussion on the optimal coating on the iLens, in order to obtain high-contrast fringes depend upon the surface reflectivity will be discussed

later. Besides, we will also validate our technique for various biological and non-bio samples and will show the picometer resolved self-calibration of our iLens interferometric technique.

2.3 Theoretical analysis to show the formation of fringes

Before we show the experimental results, we perform an analysis on the formation of high-contrast fringes from an arbitrary surface, in particular to highlight the self-calibration of our interferometer for real-time displacement measurement. We would like to emphasize that all the measurements of interference intensity is done through an iris and PD along (central point (x_0, y_0)) the axis of the interferometer. The dimension of the iris opening was sub-mm diameter and the PD sensor was around 0.8 mm^2 which is chosen much smaller than the typical fringe width to obtain high-contrast fringes in the detector plane. In this situation, the curvature of the reference and sample wave fronts falling on the detector plane (x, y) is too large and well approximated by a plane-wave near (x_0, y_0). As the iris opening is much greater than the wavelength of the He-Ne Laser, there will not be a diffraction pattern by the aperture. Also, as the iris is placed very close to the photo detector the effect of the diffraction (if there is) will not be much. The simplified analysis below illustrates the formation of randomly oriented fringes in our iLens interferometer.

The reference beam propagating along the z axis and produced by iLens on the detector plane (x, y) is given as:

$$\vec{E_R} = E_{R0}(x, y)e^{\iota(kz_1 - \omega t)} \tag{2.1}$$

where, $k = 2\pi/\lambda$. The diffuse reflection from the sample on the detector plane can be written as [26],

$$\vec{E_S} = E_{S0}(x, y)\, e^{\iota\left(kz_2 - \omega t + \xi(x,y)\right)}, \tag{2.2}$$

where z_1 and z_2 are optical path lengths from the iLens and the sample, respectively. $\xi(x, y)$ denotes a random phase difference between the two waves on the screen.

The total intensity $I(x, y)$ is given by,

$$I(x, y) \sim \left|\vec{E_R} + \vec{E_S}\right|^2 \tag{2.3}$$

Considering that the peak amplitudes of the reference and the scattered beams are identical, on solving and rearranging the terms we get,

$$I(x, y) = I_0 \cos^2\left[\frac{1}{2}\left(\beta\,(z_1 - z_2) + \xi\,(x, y)\right)\right], \tag{2.4}$$

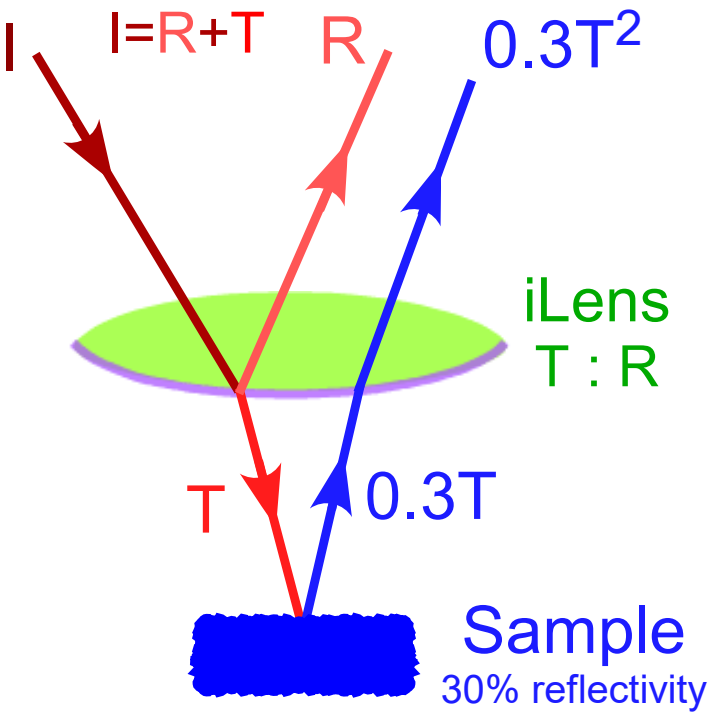

Fig. 2.3 **Illustration of optimal iLens coating for a given sample.** The parameters, T and R, denotes the percentage of the incident light intensity transmitted and reflected from the iLens, respectively. A lossless system has been assumed for this calculation.

with $\beta = 4\pi/\lambda$ and I_0 maximum intensity. The first term in the argument is deterministic, whereas, the second one is a random term. The intensity measured by the photodiode is an integral over a small area of the PD sensor ($I(x_0,y_0) = \int\int I(x,y)dxdy$). Since we experimentally measure the central intensity through iris $I(x_0,y_0)$ at (x_0,y_0) along the interferometer axis the plane-wave approximation is well-justified and $\xi(x_0,y_0)$, which defines the sample roughness, becomes a constant. The local intensity then follows the Michelson-like dependence as [7, 27],

$$I(x_0,y_0,t) \sim cos^2\left(\frac{1}{2}\beta d(t)\right), \tag{2.5}$$

as $d(t) = z_1 - z_2(t)$ is varied. After theoretically formalizing the iLens interferometer, we have to validate the setup experimentally for different rough samples. The optical coating thickness can be determined by the roughness of the sample surface. The optimal coating required for different sample reflectivity is calculated in the next section.

2.4 Optimal coating on iLens

Depending upon the reflectivity of the sample surface, the optimal beam-splitting coating on the iLens can be calculated to obtain the high-contrast fringes. Figure 2.3 illustrates a simple method for a general case of T:R coated iLens to estimate the percentage of the light intensity obtained from the reference and the object arm at the screen. In Table 2.1 we have measured the optimal coating required on the iLens surface to obtain high-contrast fringes from a given sample. The parameters, T and R, denote intensity transmission and reflection coefficients in percent, respectively. We have observed that the fringes can be obtained, even if the coating is not optimum, by adjusting the working distance of the lens and sample suitably. This suggests robustness and easy operation. Please note that for doing these calculations we assumed a lossless system.

It is worth noting that one can obtain interference fringes from any surface by using single iLens with specific ratio. In our experiments we have used the iLens with the ratio of transmitted to reflected intensity of 60:40. The obtained interference contrast $C = (I_{max} - I_{min})/(I_{max} + I_{min})$, ($I_{max}$ and I_{min} are maximum and minimum light intensity, respectively) was $70-95\%$ for all the samples. The contrast can be further enhanced by using the appropriate coating ratio described in the above Table 2.1. After selecting the iLens with appropriate coating we will now obtain the interference fringes with various everyday materials like paper, plastic, rubber, etc.

2.5 iLens interferometry on common material surfaces

To validate our setup we tested all the different everyday rough materials available to us. The iLens interferometer produced high-contrast stable fringes from a wide variety of common surfaces. We have broadly classified the samples into two categories *viz.* biological samples and non-biological samples which include paper, plastic, metal screw, cloth, etc. Figure 2.4 shows representative examples of interference pattern from 9 biological samples including human skin, human hair, insect wing, flower petal, leaf, etc. Even though some of these samples, like insect wing, human hair, were very thin the iLens was still able to collect the very small fraction of the light scattered from them to produce interference pattern. Such sensitive samples are kept near the focus of the iLens for it to collect the maximum intensity of the scattered beam to produce high-contrast fringes. Interference fringes from other readily available materials and micro-objects ($2-50\ \mu m$ diameter) like cellulose paper, quartz crystal, silicon rubber, wood, etc. is shown in Figure 2.5. The fringe shape in all the cases was determined by sample properties such as surface roughness and curvature

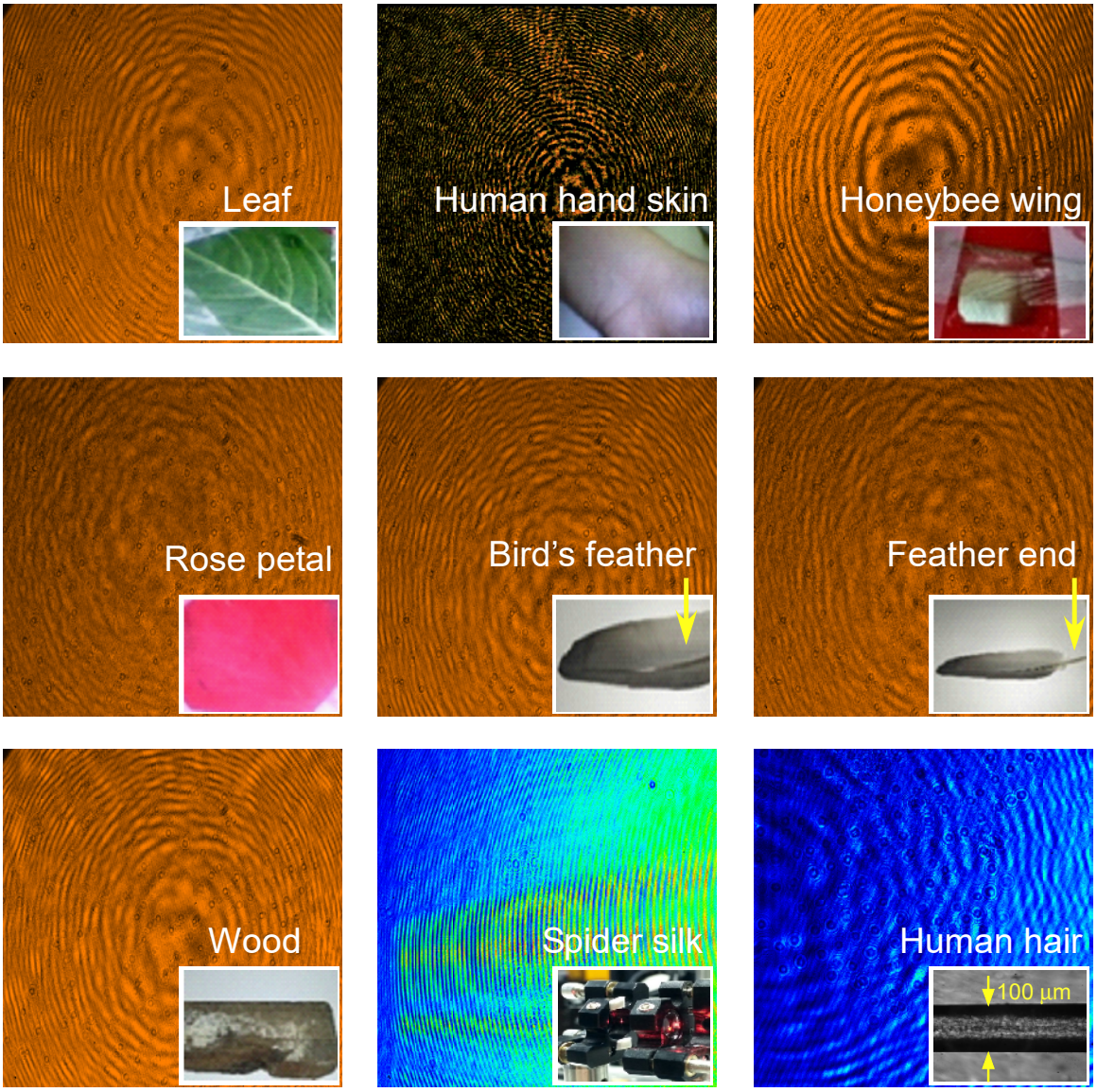

Fig. 2.4 **Demonstration of interference pattern from 9 different biological surfaces.** Typical interference fringes from the sample along with an image of the sample is shown in the inset. The contrast of the patterns, C=0.7-0.95. These patterns were captured by a camera/beam profiler using a 1-inch diameter iLens at $d = 5\ cm$. The spot size of iLens was about $1.22\lambda/NA \approx 300\ \mu m$, where NA denotes numerical aperture.

S. No.	Reflectivity of sample surface (S) (in %)	Optimum coating on iLens (T : R) (in %)	Reference beam from iLens (in %)	Object beam from sample after iLens (in %)
1	10	90:10	10	8.1
2	20	90:10	10	16.2
3	30	80:20	20	19.2
4	40	80:20	20	25.6
5	50	70:30	30	24.5
6	60	70:30	30	29.4
7	70	70:30	30	34.3
8	80	70:30 65 : 35	30 35	39.2 33.8
9	90	60:40 65:35	40 35	32.4 38.025
10	100	60:40 65:35	40 35	36 42.25

Table 2.1 **Design of optimal beam-splitter coating on the iLens** surface for obtaining high contrast fringes from a given sample surface.

[26]. However, our precision is achieved for all the cases since, the interference contrast $C = (I_{max} - I_{min})/(I_{max} + I_{min})$ was $70 - 95\%$ for all the samples. After validation, the next step in any experimental setup is its calibration.

2.6 Picometer resolved self-calibration of the iLens interferometer

The interferometric self-calibration in our measurements allows relation between interference intensity and the sample displacement without any requirement of external calibration standard. To measure self-calibrated picometer measurements, we record interference intensity

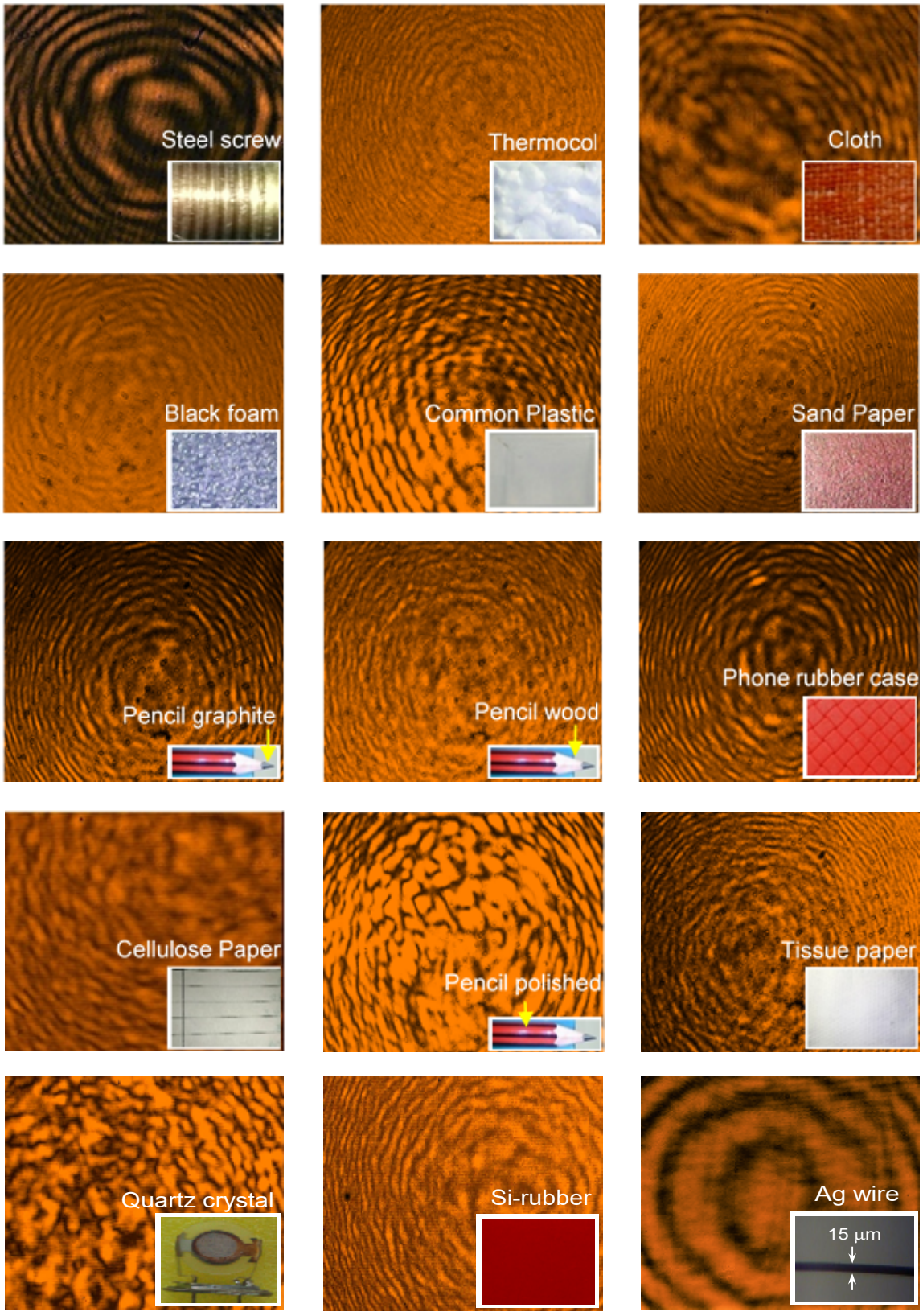

Fig. 2.5 **Demonstration of interference pattern from 15 different surfaces.** Typical interference fringes from the sample along with an image of the sample is shown in the inset. The contrast of the patterns, C=0.7-0.95. These patterns were captured by a camera/beam profiler using a 1-inch diameter iLens at d=5 cm. The spot size of iLens was about $1.22\lambda/NA \approx 300\mu m$, where NA denotes numerical aperture.

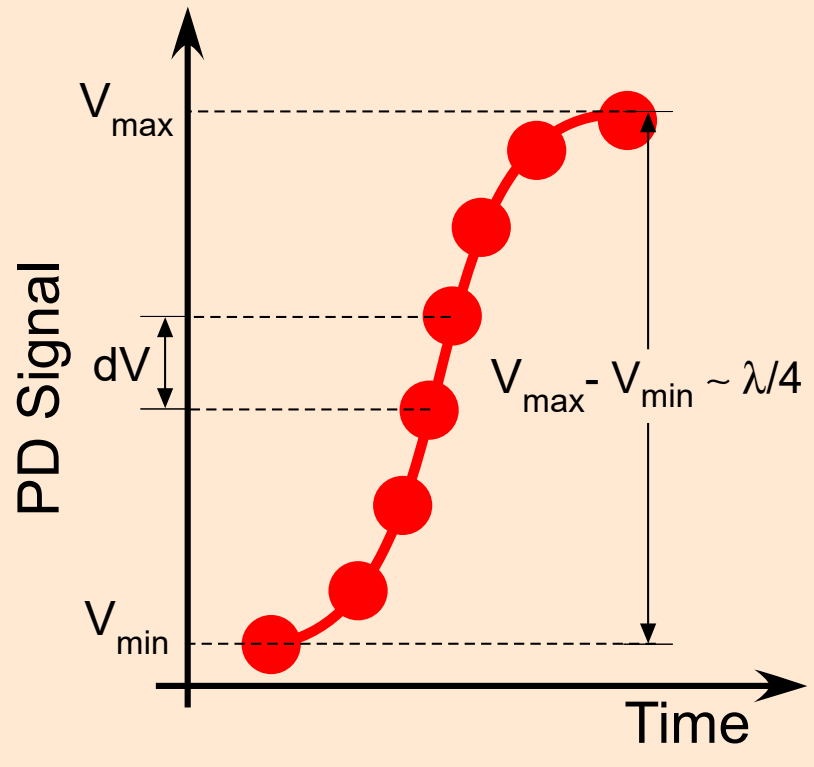

Fig. 2.6 **Illustration of self-calibrated picometer measurement using interference intensity.** Note that the interference intensity is independent of the time-axis hence latter axis cannot be used for finding the resolution of intensity.

of the central fringe with an iris and PD. The iris opening was sub-mm diameter and the PD sensor was 0.8 mm^2 which are adjusted much smaller than typical fringe-size. We established the self-calibration of our set-up for picometer measurements [28] by providing a linear input displacement $\Delta d = d(t) - d(0)$ to the sample using a nano-positioner, causing oscillations in the interference intensity, and compared the displacement measured from the PD signal. A half-fringe collapse, i.e. from minima to maxima is shown schematically in Figure 2.6. One should note that interference intensity is independent of the time-axis hence latter axis cannot be used for finding the intensity resolution i.e. for a fixed d(t) the intensity is independent of time, however, it varies if d(t) is time dependent as will be shown later in this thesis.

In our setup, we drive a piezo-stage with a ramp voltage (Figure 2.7) which causes oscillations in the interference intensity. Due to the interference condition, half-fringe collapse corresponds to a total displacement Δd of the sample by $\lambda/4 \approx 158$ nm. If we further obtain N data points between maxima and minima, the measurement resolution would simply be $\lambda/4N$. A pedagogical illustration in Figure 2.6, number of points, N, from minima to maxima is given by, $N = (V_{max} - V_{min})/dV$. Hence, Resolution = $\lambda/4N$. In Figure 2.7,

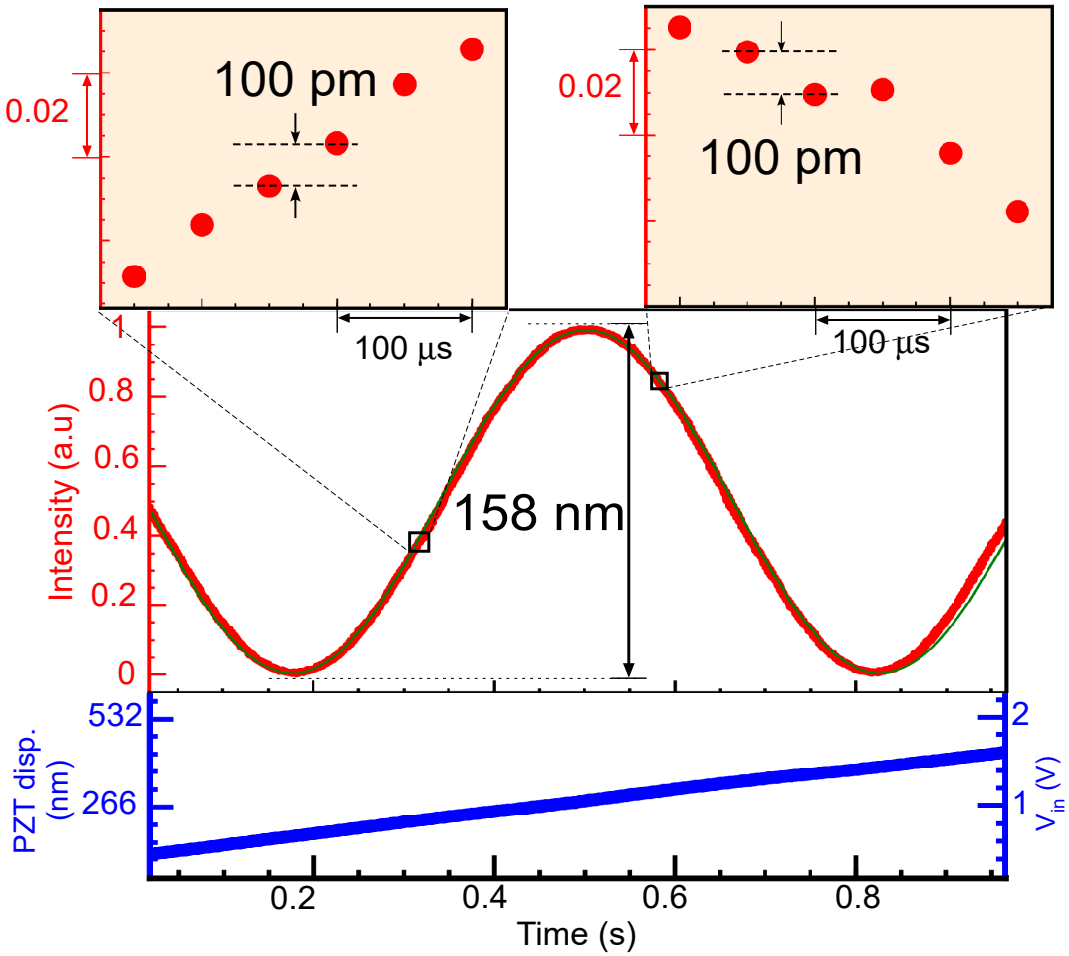

Fig. 2.7 **Self-calibration data on cardboard sample.** Calibration curve: The nano-positioner was given a known displacement (Blue Curve, ramp wave of 5V) with FG ($1\ V \approx 2.6\ \mu m$) and the corresponding change in the fringe intensity (Red Curve) was recorded via PD ($\lambda/4 \approx 16\ mV$ for cardboard). The two insets shows the displacement of $\sim 100\ pm$ at two different point on the intensity curve. Then the nano-positioner was given a square wave input with lower voltages (up to 1 mV, lower limit of FG) and the corresponding change was observed in the fringe intensity.

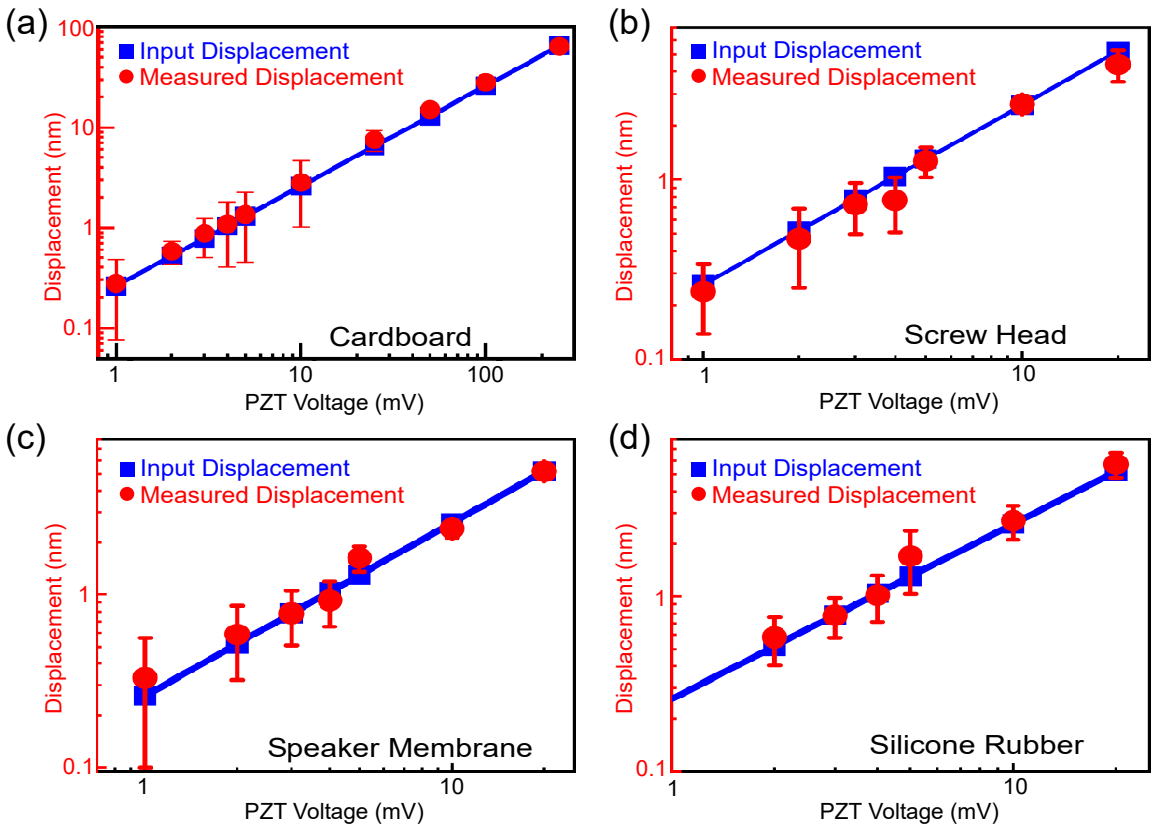

Fig. 2.8 **Calibration data on four different samples.** (a-d) Calibration curve showing input sample displacement (blue square) with the one independently measured using PD (red circle). The solid line is a linear fit. Error bars indicate experimental noise-floor.

there are $N \sim 2000$ data points from minima to maxima, therefore, the resolution of iLens interferometry is $\lambda/4 \times 2000 = 80$ *pm*. It is possible to record about 10,000 data points, giving rise to $\lambda/(4 \times 10,000) \approx 15.8$ *pm*. In our setup, we can drive piezo-positioner by a minimum, $V_{PZT} = 1$ *mV* driving amplitude (lowest limit of used function generator). This puts a practical limit on demonstration of picometer calibration as in Figure 2.8(a-d).

The input and measured displacements agreed very well over the entire measurement range covering three orders of magnitude as shown in Figure 2.8(a). Similar data validating our calibration procedure on four different rough samples is shown in Figure 2.8. Moreover, real-time detection of fringe-intensity and displacement is shown in Figures 2.9, 2.10 for cardboard and speaker membrane sample respectively for different displacement amplitude. The displacement of 260 *pm* was fully detectable. The actual resolution in our displacement measurement is sub-20 *pm*, as we will show in Figure 2.9. However, lack of reliable method for controlling displacement of rough-sample below 266 *pm* determined the lowest data point in the calibration curves (Figure 2.8(a-d)). We emphasize that the self-calibration must rely

on the interference condition, i.e., half-fringe collapse corresponds to $\Delta d = \lambda/4 \approx 158\ nm$, and it is independent of the time-scale of the fringe collapse. Also, one must be careful to avoid transverse displacement of the sample, which may lead to error in actual z-displacement. After calibrating the setup, in the next section, we will now study the surface dynamics in real-time with picometer precision.

2.7 Real time picometer resolved surface dynamics

In Figure 2.9(a-d), we demonstrate the use of interference intensity for real-time sub-20 pm precision in measuring dynamic displacement of arbitrary surface, such as a cardboard. The sample was imparted a single input displacement-pulse (in blue) of different peak amplitudes 5.2 *nm*, 2.0 *nm*, 500 *pm* and 310 *pm* and resulting displacement was independently measured (in red) with a PD and oscilloscope. The measured displacement Δd agreed very-well with the input. On the right-hand side of each curve, we show the histograms of noise showing a standard deviation of about 270 *pm*, resulting from residual mechanical stress, beam pointing, non-uniformity in air pressure, and detection electronics noises. The zooms near steps in the insets of Figure 2.9(b,d), show our ability to resolve sub-20 pm displacements within 300 μs. Similar data for other samples are presented in Figure 2.10 to prove repeatability in our measurements. The dynamic range of displacement for our interferometer is $2Z_R/\Delta d$ where Z_R is Rayleigh range of iLens and $\Delta d = 20\ pm$ was around 10^9 for near focus operation.

It is worth mentioning that the demonstrated picolevel sensitivity was achieved with simple real-time detection of interference intensity with a PD, without lock-in, heterodyne, or noise-filtering techniques [8, 1]. Such advanced techniques may further enhance resolution of our interferometer close to fundamental thermal-noise limit albeit for rough surfaces.

It is worth comparing our interferometer with the well established Michelson [1], Mirau [5] or Fizeau interferometers [29] which essentially require precise stabilization and alignment of its multiple components like beam-splitter, reference mirror and light collector.

No interferometer has been shown to work directly with rough surfaces and achieve pm precision probably due to their multiple components. Although the Mirau interferometer is compact [5], its reference mirror not only clips the incident beam but also require a fixed working distance. In contrast, our interferometer design offers fully clear view, flexible working distance within several times Z_R. A detailed comparison of iLens interferometer with the state-of-the art interferometers has been discussed in Appendix 1. Furthermore, we verified its robustness by purposefully tilting the iLens ($\pm 10°$) and yet retaining the fringes, which could be used for further miniaturization. Importantly, the universal applicability

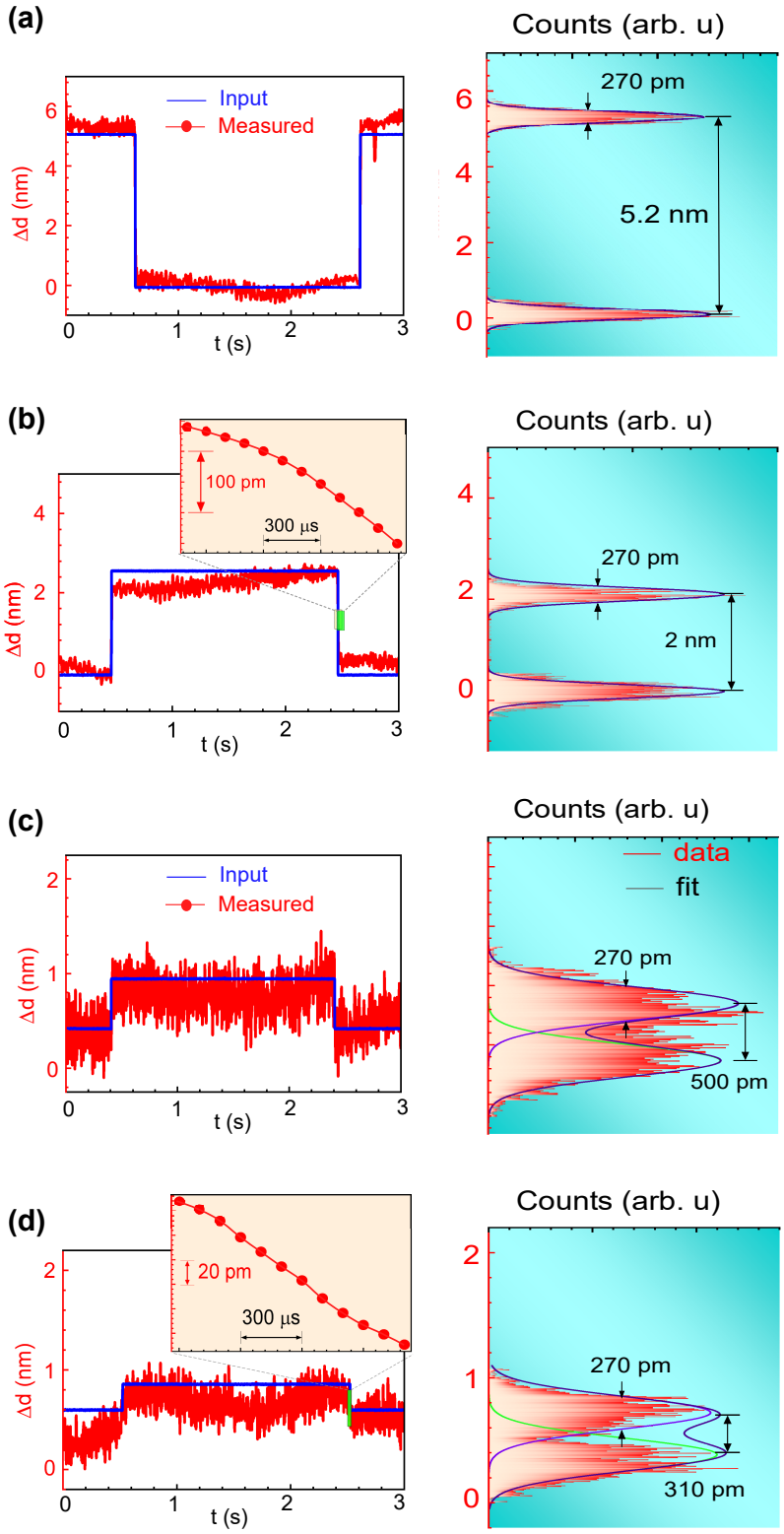

Fig. 2.9 **Real-time picometer resolved surface dynamics.** (a-d) Measured displacement and input displacement versus time for cardboard surface at different amplitudes (a) 5.2 *nm*, (b) 2.0 *nm*, (c) 500 *pm* and (d) 310 *pm*. The figures on the right-side of each graph indicate histogram of signal indicating the noise-floor and resolution between two levels. Insets: zoom showing sub-20 *pm* change in Δd within 300 μs interval. Histograms fit have Gaussian distribution with standard deviation of 270 *pm*.

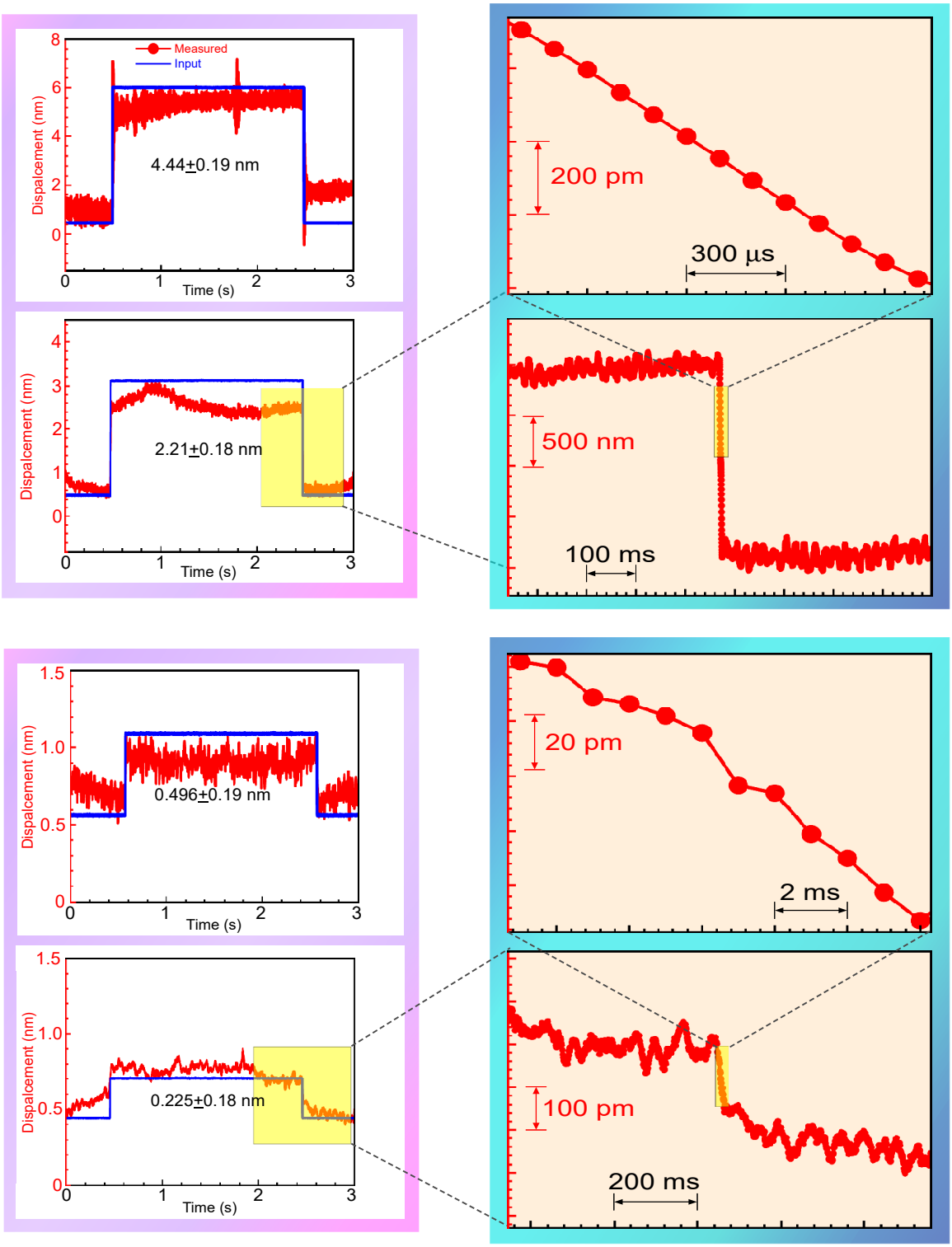

Fig. 2.10 **Real time detection of picometer displacement for speaker polymer membrane.** Interferometric detection of sample displacement caused by PZT (Blue curve) of amplitudes 4.4 nm, 2.2 nm, 496 pm, 225 pm.

of our interferometer on any scrap material, ultra-affordability and easy operation with self-calibrating pico-level precision makes it attractive for wide applications.

2.8 Conclusion

We demonstrate a new paradigm of universal interferometry with everyday materials enabling self-calibrated real-time measurements with picometer resolution. We integrated key functions of beam splitter, reference mirror, and collection optics into a single interference lens (iLens) which when combined with any everyday material, such as paper, wood, plastic, rubber, unpolished metal, skin, etc., formed the compact and universal interferometer producing stable high-contrast fringes. We have demonstrated a real-time self-referencing precision of ~ 20 *pm* under ambient conditions without averaging.

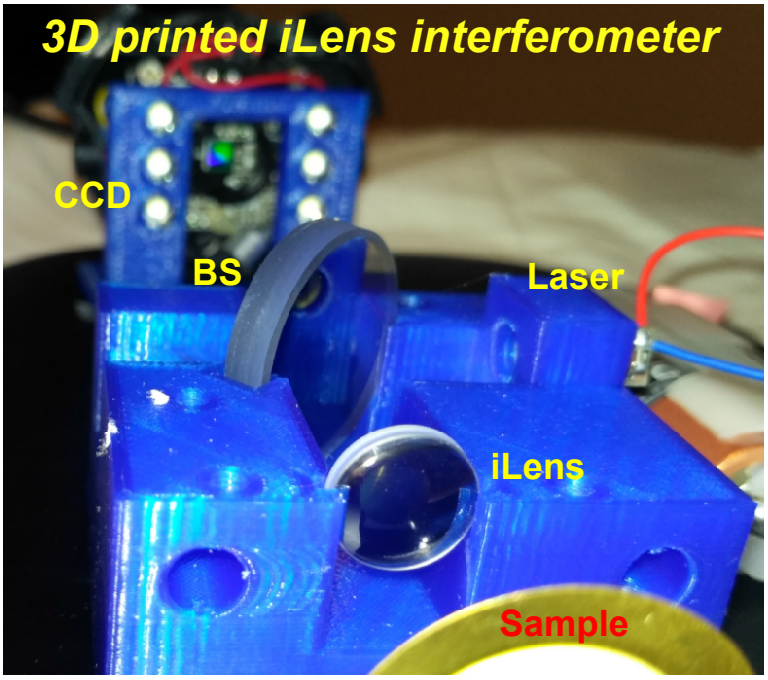

Fig. 2.11 **Prototype of the compact iLens interferometer on 3D printed substrate.** The iLens with $f = 12$ *mm*, $d = 12.7$ *mm* and coating ratio of 30:70 is mounted on a 3D printed substrate along with a Beam Splitter (BS), CCD camera, laser diode, and sample holder.

The sensitivity and speed of our current measurement can be further improved. The precision of few hundred picometers of the current apparatus is only limited by the set-up components. If frequency stabilized lasers and electronic signal processing is also used, one can obtain thermal-noise limited precision similar to the sophisticated interferometers [7, 8].

In addition, using high-speed avalanche detectors one should achieve sub-*ns* time-resolution. In applications demanding compactness, one can design a micro-iLens with micro-lasers and detectors on 3d printed substrate. A prototype of the compact iLens interferometer on a 3D printed substrate is shown in Figure 2.11.

In Chapter 3, we will demonstrate various applications of iLens in fabrication of precision frugal devices made with everyday materials yet matching or outperforming their state of the art counterparts. The next chapter will also discuss application of iLens interferometer in probing dynamics of candle flame plasma with sub-nanometer precision and the surface deformation of complex fluids subjected to optical or electrical stimulation.

Chapter 3

Applications of iLens Interferometer

3.1 Introduction

With the advancement in science and technology, more and more scientists desire to achieve unparalleled precision in measurement of time, displacement, force, material deformation, etc. Generally, the high precision measurements of various physical quantities require high-end sophisticated devices, which are expensive. Although the scientific knowledge is priceless, gaining the knowledge should also be cost effective. While for some well equipped universities the cost may not be an issue, in most developing nations, like India, access to high-end expensive instruments for research and high-end teaching may not be easily available.

Design and development of inexpensive frugal optical instruments without compromising the precision can prove to be a boon. In this regard, the central question arises on how to devise approaches to design high-end optical interferometers for precision measurements. Is there a way that we could inculcate the frugal optical science, using everyday items, for our obsession towards superlative precision?

In this Chapter we demonstrate two different kinds of applications of the iLens interferometer. First, we will demonstrate a couple of frugal photonic devices based on the iLens whose precision matches or outperforms their commercial counterparts. Second, we will use iLens to perform fundamental measurements of pump induced nano-mechanical dynamics on solid surfaces and to resolve photo-dynamics of the candle flame plasma in real time with picometer precision. These two applications suggest vast possibility of iLens interferometry.

3.2 The concept of frugal optical devices

While the idea of frugal science is quite old, over the past decade many interesting frugal devices have been invented. This was with an objective to impart affordable knowledge to the society in resource-less settings in a cost-effective way and for low-cost technological applications. For example, a paper based optical microscope, known as foldscope [23] was designed and shown to have practical applications in disease identification. Similarly, a hand-powered paperfuge [24], and microfluidic paper-based analytical devices [30, 25] are low-cost alternative to pressing healthcare needs. However, design of frugal optical devices offering high-precision is difficult because the route to direct interferometry with common items is not known. This has constrained broad practical applications of interferometry for realizing counter-intuitive idea of constructing super-precise optical devices from scrap materials. This goal requires a unique approach to overcome difficulties in obtaining high-contrast fringes directly with common surfaces, self-calibration with picometric precision, and universal applicability for diverse materials. Our universal iLens interferometer opens path for a new class of ultra-affordable photonic devices from scrap yet offering unprecedented precision for diverse applications in science and education.

In the following, we will realize and establish three kinds of iLens based frugal photonic devices from common materials such as, a paper-based picogram weighing balance, a broadband and pico-level acoustic sensor using cloth/paper, human-hair based *pN* radiation pressure sensor operating in air. Our frugal devices made from different common materials are easy to operate and vastly outperform their high-end commercial counterparts.

3.2.1 Paper-based pico-balance

Precision weighing balances are used widely for scientific and commercial purposes in our everyday life. The sensitivity of a weighing balance, i.e., its ability to resolve minimum weight, is decided by the operating principle and design of its load-cell. A load-cell is a transducer that produces some electrical signal in response to a weight force. For high-end digital balances, a load-cell converts the weight force into electrical signal by electromagnetic force (EMF) compensation mechanism [31]. The cost of the balance increases with the accurate design of the EMF load cell. Such commercially available load cell can measure few grams with a precision of micro-grams.

There are various solutions for precision weighing in femto-to-zepto grams range using nano-mechanical resonators by measuring the load-induced shifts in its resonance frequency [32]. Such nano-beams are carefully fabricated with dedicated nano-processing of SiN and require high-vacuum and cryogenic conditions to achieve zepto gram precision. Various

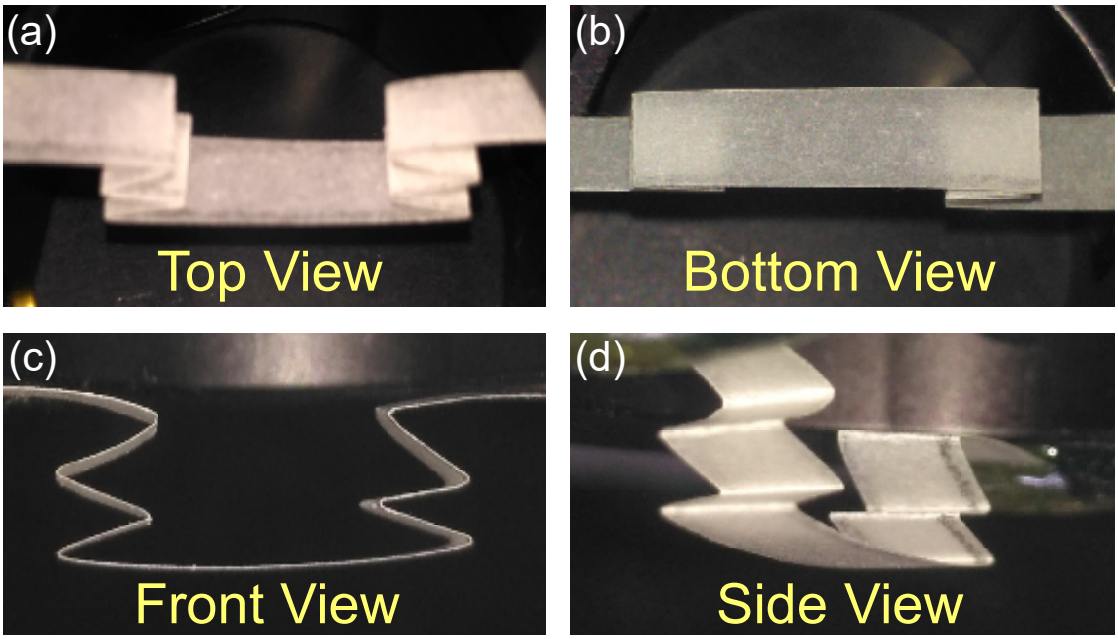

Fig. 3.1 **Paper-based load cell design.** (a-d) shows the top, bottom, front and side view of the load cell designed for the paper-base balance respectively. The width of the paper-strip was 4 mm.

inertial sensors based on micro-cantilevers have also been designed to weigh living cells, tissues with femto-gram precision [33, 34]. Such setups are very sophisticated and require specialized means to design the micro-cantilevers with dedicated readout mechanism.

Here, motivated by the paper origami [35], we designed and demonstrated a paper-based load cell for precision weighing balance. The basic idea was to fold a strip of easily available paper and read the load-induced displacement of the paper using our iLens. Since the iLens enables picometer resolution in the displacement of paper, as demonstrated in the previous chapter, we intend to achieve precision weighing.

3.2.1.1 Fabrication/Design of the paper load cell

We folded a strip of paper (80 μm thick, 4 mm wide, L=1.5 cm) in zigzag-pattern to design an elastic load-cell [35]. Figure 3.1(a-d) shows the top, bottom, front, and the side view of our designed load cell respectively. We measured the spring-constant of the paper-load cell by pulling test which validated its Hookean response with $k = 24\ N/m$ (as shown in Figure 3.2) upto a maximum load limit of about 0.6 mN. The load-cell is attached with a heavy weight at it center. Then the load-cell is pulled up using a motorized translation stage and attempts to lift a fixed heavy mass initially resting on the weighing pan of the

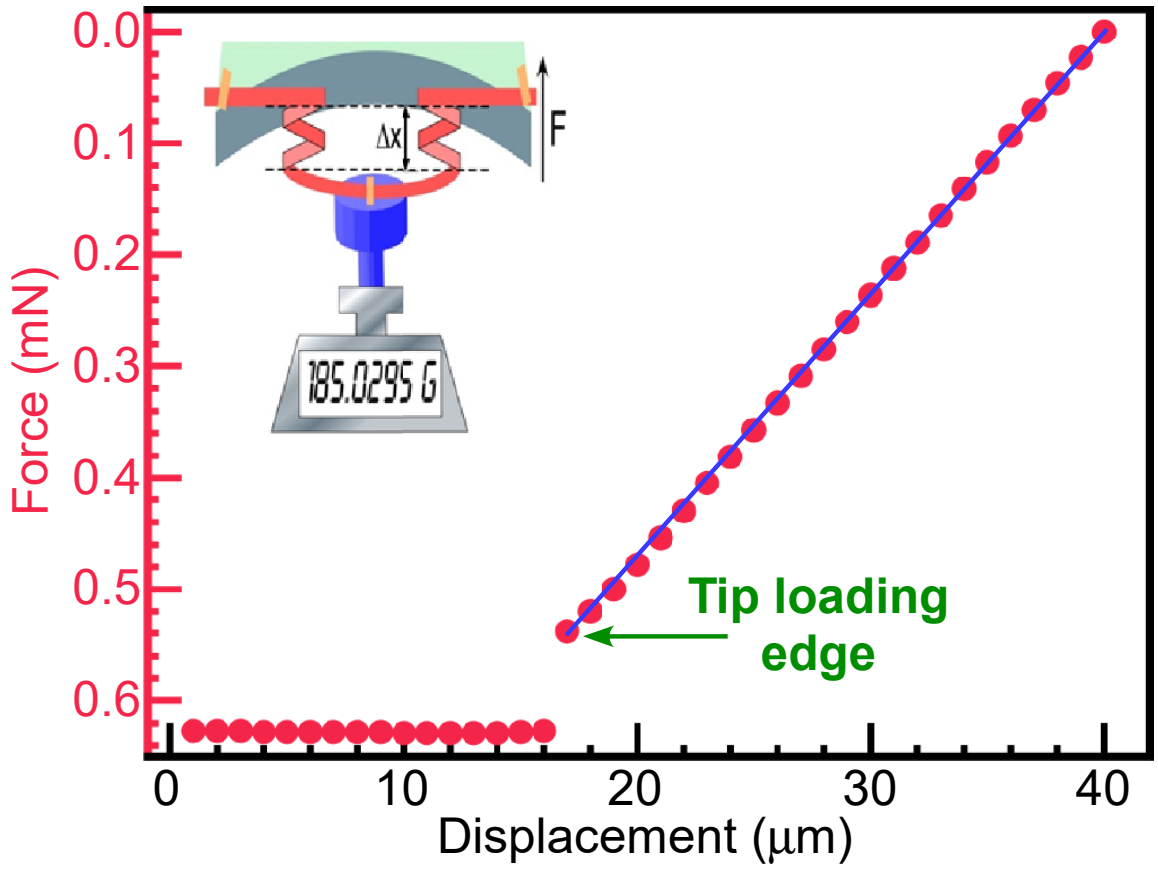

Fig. 3.2 **Measurement of force-displacement curve and spring constant of the paper load cell.** Inset shows the schematics of the setup. A tiny initial jump at first contact is attributed to a sudden jerk in the pulling. The slope of the curve is the spring-constant, $k = \Delta F/\Delta d$, for our load cell was 24 N/m.

micro-balance. The change in mass read by the balance is used to compute the force by multiplying it with local gravitational acceleration, while the displacement of the load-cell is recorded from the position of the translation stage. The force-displacement curve follows Hooke's law up to 0.62 mN, beyond which the load-cell lifts the mass in air (zero-force). The slope of the curve is the spring-constant, $k = \Delta F/\Delta d$, for our load cell was 24 N/m. A tiny initial jump at first contact is attributed to a sudden jerk in the pulling. One can also write, $k = 24\ pN/pm$, indicating that a displacement precision of picometer will lead to weight precision in pico-gram.

We used the paper-load cell to fabricate a paper-based optical balance enabling rapid picogram precision measurements.

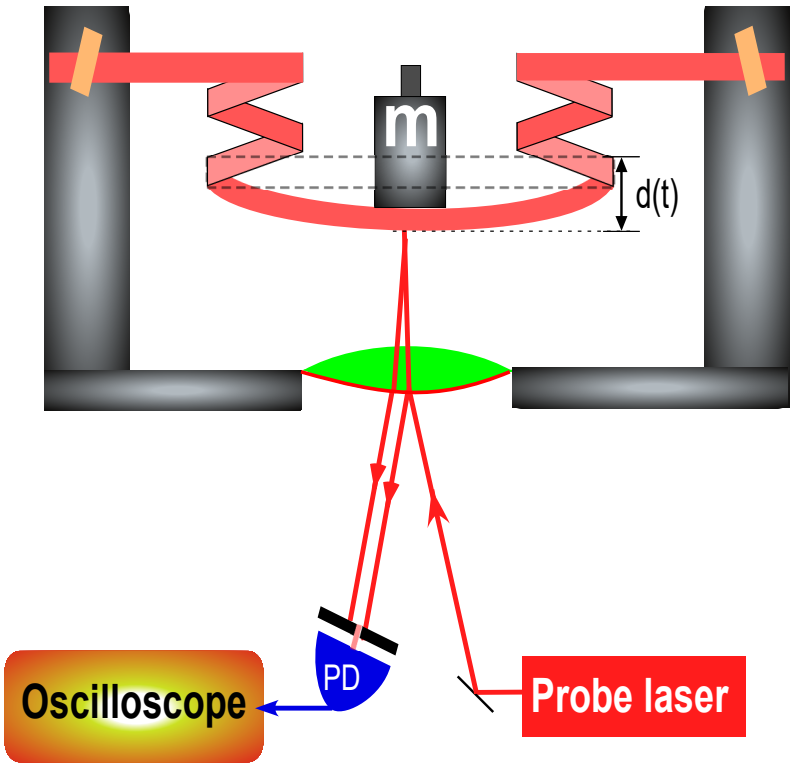

Fig. 3.3 **Schematic of the paper-load cell based optical balance.**

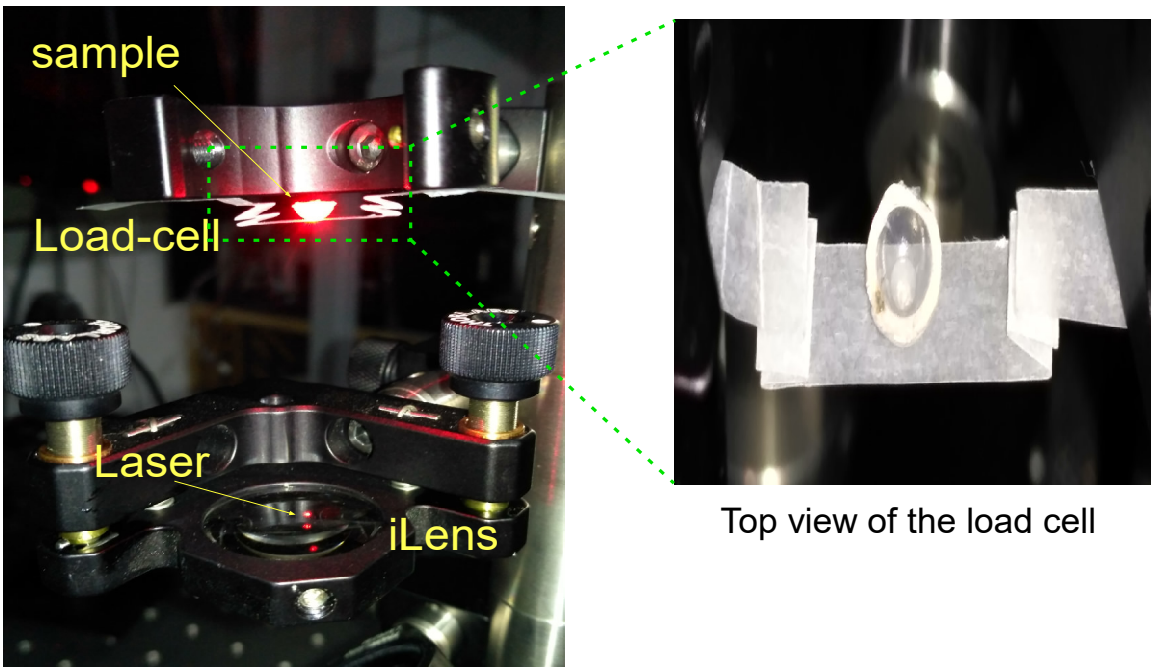

Fig. 3.4 **A labelled picture of the weighing set-up.** The right side figure shows the top view of our load cell with sample holder placed on it.

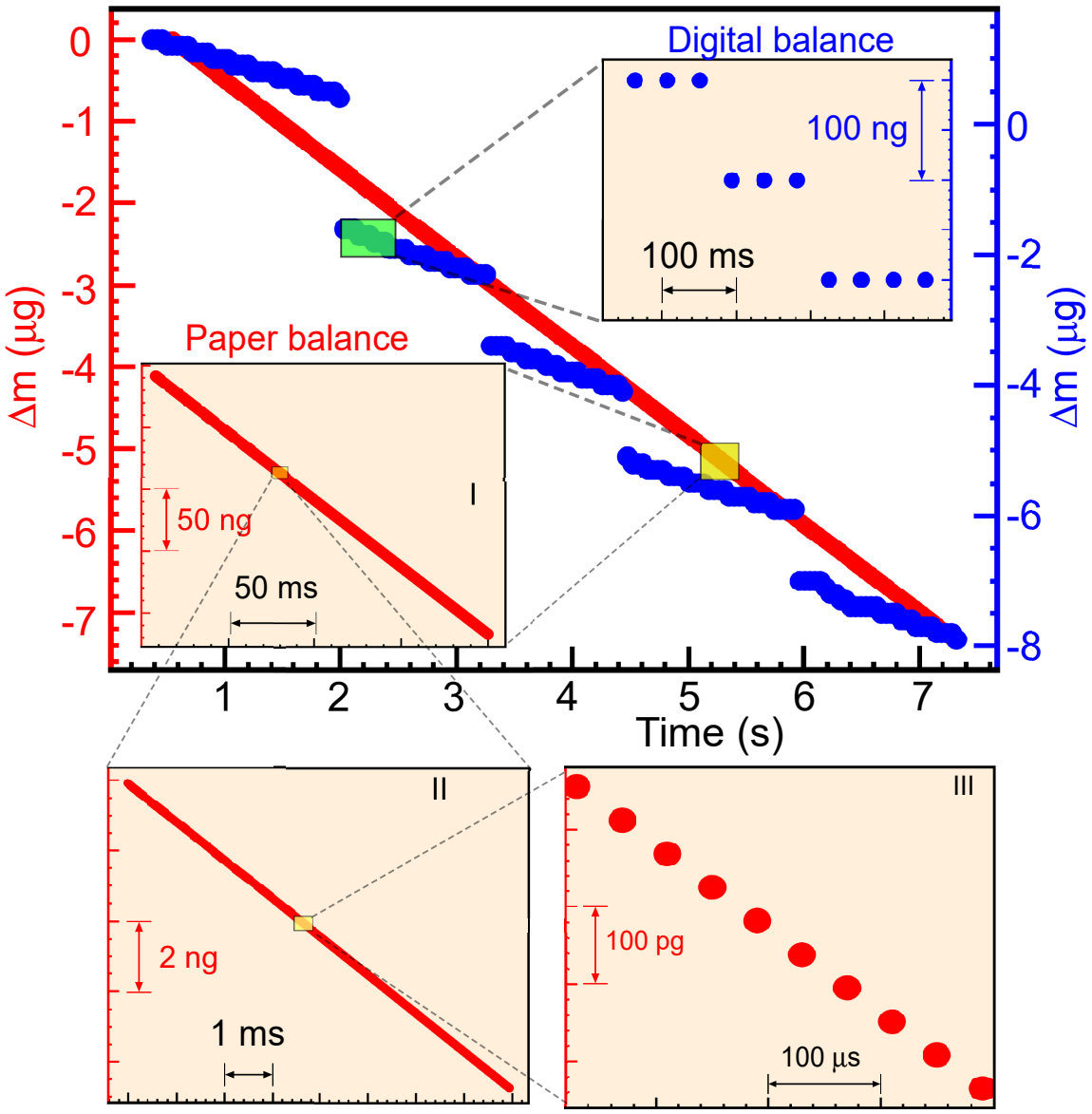

Fig. 3.5 **Experimental data for weight-loss of an evaporating water drop**. Comparison of weight-loss of an evaporating water drop with paper balance (red data) and electronic ultra-micro balance (blue data). Zoom of the electronic balance data shows 100 *ng* resolution. Zoom of the paper-balance shows about 100 *pg* with 1000 times faster readout. Error bars are about the size of the data symbols.

3.2.1.2 Set-up of iLens based paper-pico-balance

Figure 3.3 shows the schematic of our paper-based pico-balance. The paper load cell was mounted firmly on a C-type holder. The vertical geometry of the iLens interferometer was used to build the pico-balance. The low-power He-Ne laser was made incident on the iLens from below to obtain interference fringes from the bottom side of the paper load cell. The reference beam from the iLens is superimposed with the object beam scattered by the paper-load cell to produce the randomly shaped fringes. A plastic sample holder was then kept on top of the load cell and the whole setup was brought to equilibrium. The table-top experimental setup is shown in Figure 3.4, the right side image shows the top view of the load-cell with the sample holder placed on its top. When the sample is placed in the sample holder, it causes the load cell to displace from its equilibrium position. This change in the position of the load cell causes a shift in the interference fringe intensity which is recorded using a photodiode through an iris. The paper optical balance was enclosed in a removable plastic enclosure to minimize acoustic noise and air currents. To calibrate the pico-balance we measured the change in mass of an evaporating water drop and was compared with a commercial balance as discussed in the next section.

3.2.1.3 Performance comparison of Paper balance with 7-digit electronic balance

A weight force on the middle of the load-cell produced elastic deformation δy, that was directly measured with pm precision with iLens to estimate unknown mass $m = (k/g)\delta y$, where g is the acceleration due to gravity, and k is the spring-constant of the load-cell. The weighing performance of our paper-balance was compared with a commercial electronic ultra-microbalance, Mettler-Toledo, with a weighing precision of $0.1\mu g$, which is based on the electromagnetic force compensation technology [31]. We measured, for example, mass of an evaporating water drop under identical conditions of temperature, humidity, volume and surface area. As shown in Figure 3.5, the ultra-microbalance exhibited discrete weight-jumps corresponding to 100 ng precision (one part in ten million) within tens of ms. In contrast, our paper-balance is 1000 $times$ more precise with sub-100 pg weighing accuracy. Moreover, thanks to the direct optical measurement of the load-induced displacement, our device can provide 1000 $times$ faster measurements. Even though, our balance is compact, and easy to fabricate and calibrate, it can achieve picogram precision in ambient conditions.

3.2.2 Cloth-based iLens acoustic sensor

In another application, we used cloth, paper or polymer membrane as an ultra-sensitive acoustic sensor operating from 1 Hz to 200 kHz. We obtained interference pattern from such

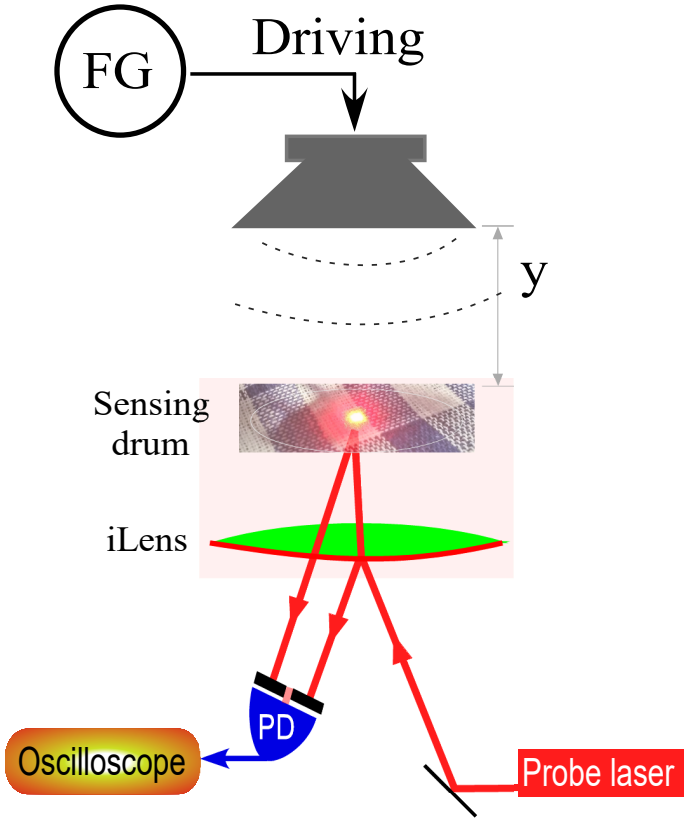

Fig. 3.6 **Design of frugal optical acoustic sensors.** Schematic of iLens acoustic sensor made from cloth/paper/polymer.

diaphragms and used interference intensity, as described previously in Figure 2.7, to measure its dynamic displacement in real-time. Three example devices were fabricated from the three common materials, a cotton cloth (around 200 μm mesh size, diameter $D = 12.5\ mm$), a paper-load-cell, and a polymer diaphragm film. We validated our devices by subjecting it with acoustic driving at different frequencies and different driving amplitudes, as shown schematically in Figure 3.6.

3.2.2.1 Experimental set-up

The schematic of our custom built acoustic sensor is shown in Figure 3.6. Here, we used the He-Ne laser to obtain the interference fringes from cloth, paper or polymer membrane, which act as the diaphragms of the acoustic sensors. The acoustic signal kept at a distance was used to drive these diaphragms and the corresponding shift in the fringe intensity was recorded using the photodiode. For this, all the devices under test were kept at a fixed distance ($y = 5\ cm$) from an acoustic source, and their response to acoustic signal was detected from

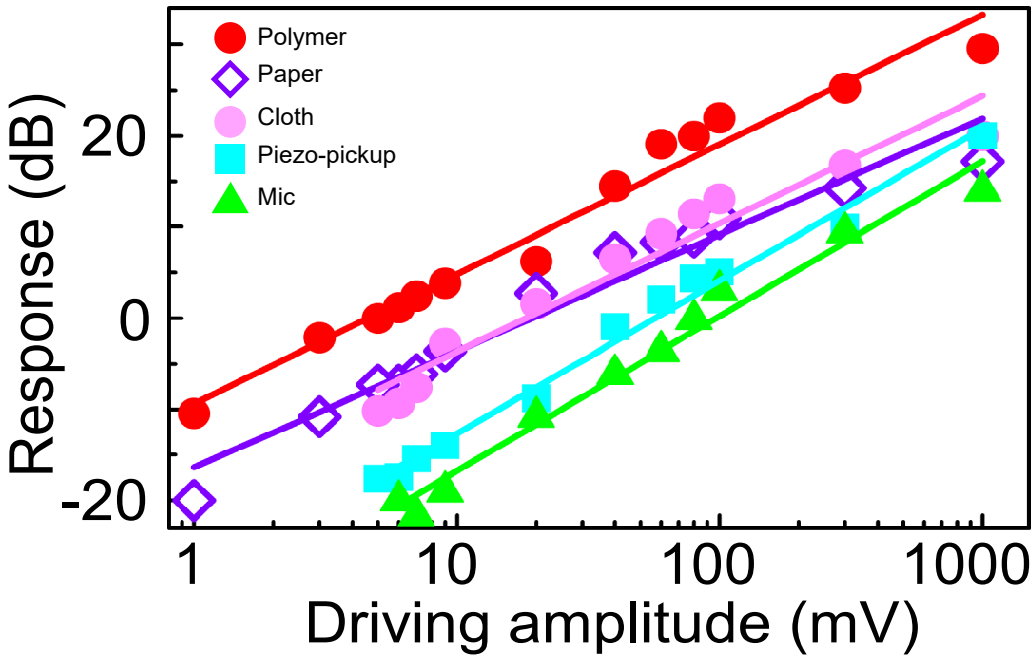

Fig. 3.7 **Characterization of frugal optical acoustic sensors.** Comparison of detection sensitivity of frugal sensors with piezo and microphone at 1000 Hz. Source amplitude was varied by driving voltage for a fixed source-sensor distance.

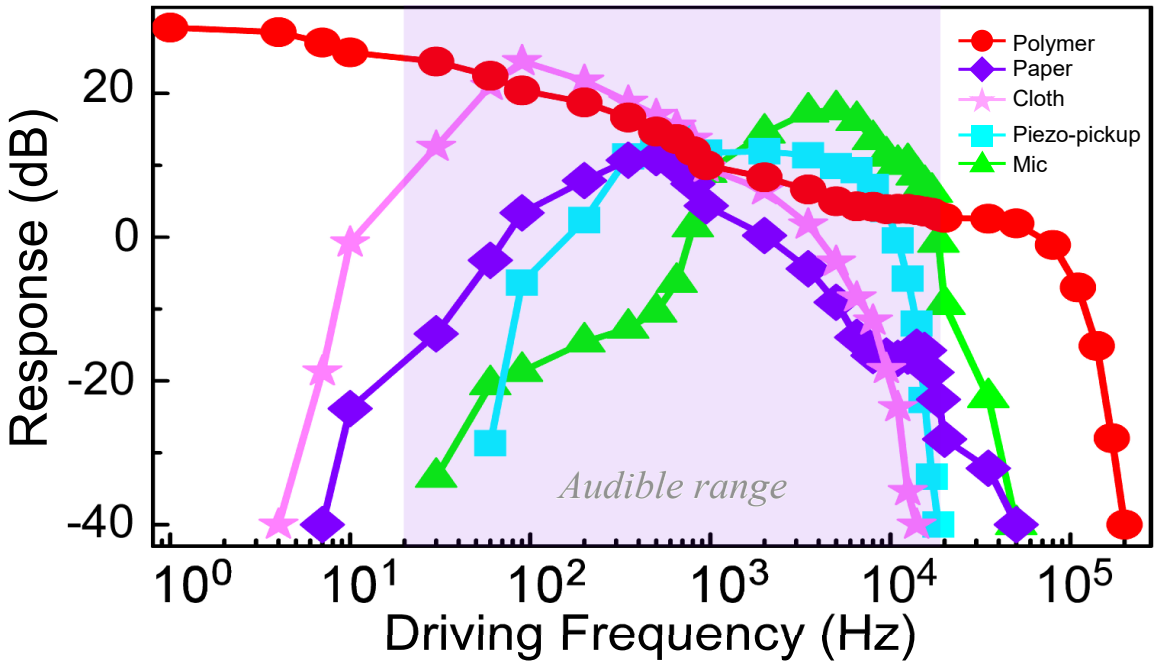

Fig. 3.8 **Characterization of frugal optical acoustic sensors.** Frequency response of iLens acoustic sensors when compared to piezo-pickup and microphone. Response (dB) is defined as $20Log_{10}(V_{sensor}/V_{ref})$ at $V_{ref} = 1\ mV$.

1 Hz to 200 kHz driving frequency. It is worth comparing the bandwidth and sensitivity of our acoustic devices with easily available commercial sensors such as piezo-pickup and an electromagnetic microphone.

3.2.2.2 Sensitivity and bandwidth of frugal acoustic sensors

Initially the sensors under test were driven by the acoustic signal of varying amplitude from 1 mV to 1 V at a frequency of 1 kHz. The sensitivity of our acoustic sensors made with cloth, paper load cell (described in the previous section), and polymer membrane was compared against the piezo pickup and electromagnetic sensors as shown in Figure 3.7. We found that even at low input voltage of 1 mV our interferometer was able to detect the displacement caused by the acoustic vibrations, whereas, the existing sensors started responding at a minimum input amplitude of ~ 10 mV. Thus, owing to our interferometric read-out our sensors exhibited higher sensitivity (e.g., at 1 kHz) to weak driving amplitude of the source (Figure 3.7).

Furthermore, our custom-built sensors exhibited broadband response from infra-sound to near-ultrasound frequencies, while the piezo and electromagnetic sensors responded mostly in the audible range as shown in Figure 3.8. For the bandwidth comparison the samples were driven at an input voltage of 1 V with varying input frequency and the corresponding change in the interference fringe intensity was recorded at the oscilloscope using a photo-diode. All these sensors operated in the linear-regime for their comparison. We attribute the maximum cut-off frequency of our devices to the inertia of the vibrating drum since we drive them far beyond their natural resonance frequency [36]. In fact, when the vibrating polymer diaphragm of a commercial headphone speaker was read with the iLens, instead of electrically, we could achieve enhanced bandwidth as well as sensitivity (compare curves in red and green in Figure 3.8). Our frugal acoustic devices present an attractive alternative for various applications demanding low-cost precise displacement sensing, such as in medical instruments [37, 38] and photo-acoustic spectroscopy for trace-gas detection [39].

3.2.3 Micro-fibre based nano-Newton force sensors

In an important advancement, in particular to study the microscale objects, we demonstrated fringes from a single human hair strand ($D \sim 50$ μm), Ag-wire ($D = 15$ μm), and remarkably with a single spider dragline silk ($D = 1-3$ μm). Local dynamic deformation of these micro-objects, in response to external optical, acoustic, and thermal excitations, has been measured with the interferometric precision without any sample preparation such as metal coating.

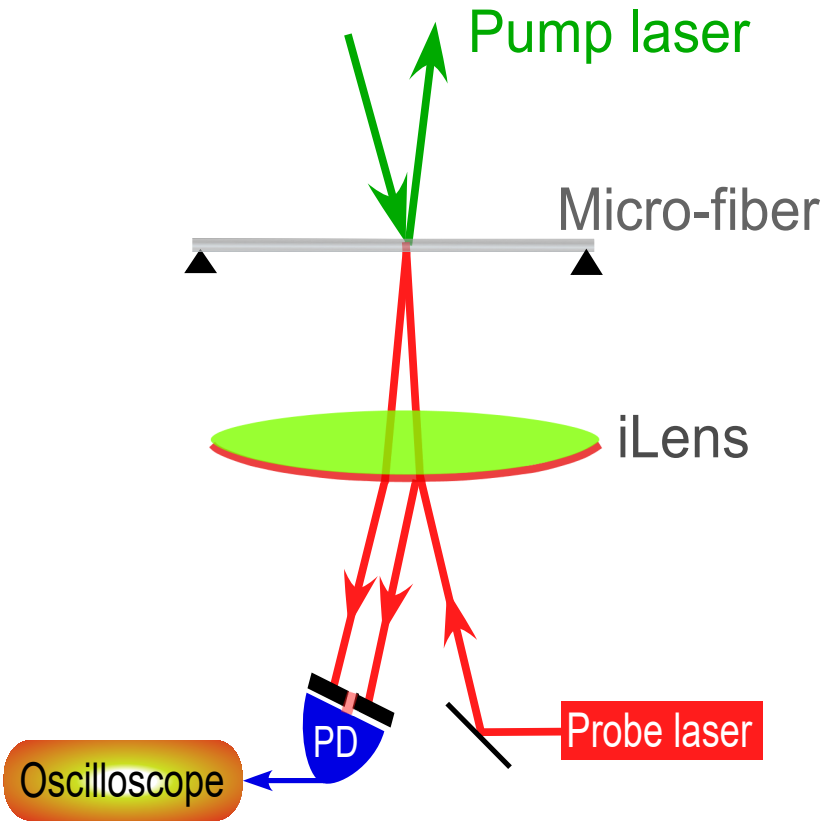

Fig. 3.9 Design of bio-fiber based optical force sensors.

Although the size of these objects was much smaller than the spot size (around 200 μm), the collection of a fraction of back-scattered light was sufficient to obtain high-contrast fringes.

3.2.3.1 Experimental set-up

We demonstrated a direct detection of sub-nN optical force in air using human hair as an actuator. Figure 3.9 shows one of our devices fabricated by freely suspended white human hair ($D \approx 100\ \mu m$, length $L = 1.2\ cm$). The spot size of the laser beam at the hair sample is $\approx 300\ \mu m$ which is much lager than the sample size, therefore, the light scattered back in the direction of the optical axis of the interferometer is very less. To avoid the light being collected from the nearby substrate surfaces the micro-fiber sample under test is fixed at its both ends to a hollow mount as shown in the schematic diagram. The maximum contrast of the interference fringes was obtained for the sample kept within the Rayleigh length of the iLens. The shape of the interference fringes obtained from the white human hair sample is

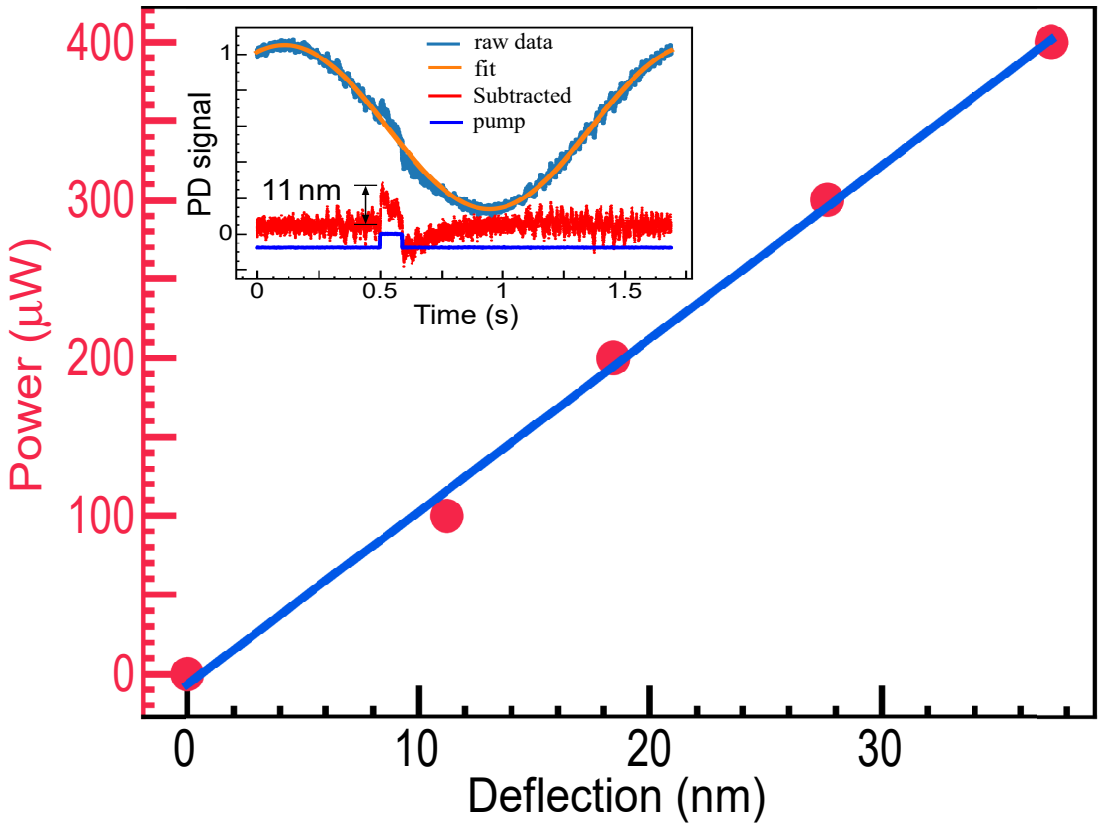

Fig. 3.10 **Ultra-sensitive bio-fiber force sensors.** Maximum deflection of hair-fiber versus laser power. Upper inset: experimental signals showing 11 *nm* deformation using a white human hair ($D \sim 100\mu m$, $L = 12.5\ mm$). Both the ends of the sample were clamped and the sample was excited in the middle by a pump laser. The oscillation in the $I(t)$ shows a background modulated signal that is used to find the direction of deflection.

shown in Figure 2.4. To study the time-resolved displacement the hair sample was excited using a low-power cw pump laser ($\lambda = 532\ nm$) with varying power. The pump and probe beams overlap on the same point on the sample but from the opposite direction as shown in Figure 3.9. In the next section we will study the deformations caused in the micro-sample when exposed to pump laser.

3.2.3.2 Bio-fibre deflection with laser power

The time-resolved displacement of the hair following low-power pump-laser irradiation, is shown in left-side inset of Figure 3.10. One can clearly distinguish a fully reversible step-like nanometric displacement of the fiber during on and off of the pump beam. We also observed a fully reversible slow-response due to weak laser heating which is related

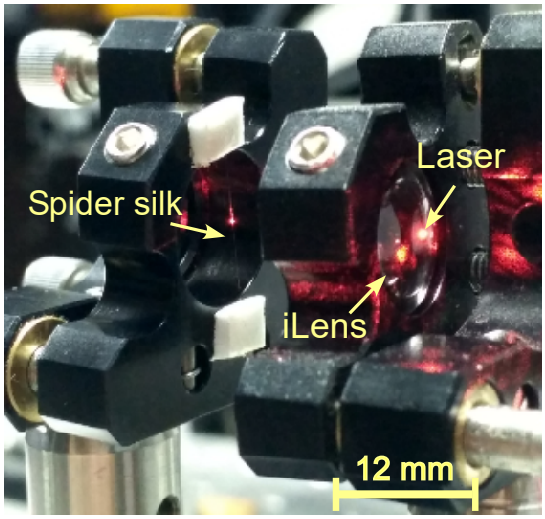

Fig. 3.11 **Prototype ultra-sensitive force sensor with spider silk.** The probe laser is used to measure the time-resolved displacement of the silk. The pump and probe beams overlap on the same point on silk. The diameter of the silk thread is approximately $1-3$ micron and its length is about $1.2\ cm$.

to thermal properties of the sample as detailed later. Considering about 80% reflectivity of our sample & for 100 μW of total irradiated power, we obtained a spring constant of about $k = 50\ N/m$. This value was independently confirmed by measuring a force-displacement curve of the same sample, analogous to the paper-load-cell case. Furthermore, the amplitude of the deformation varied linearly with the pump laser power.

Detection of sub-nN radiation pressure effects is of great recent interest and most measurements have been performed using SiN cantilevers at micro- and nanoscale [40, 38, 41]. To the best of our knowledge this is the first demonstration of radiation pressure effects on everyday micro-objects.

The sensitivity of our device can be further enhanced, for example, by replacing the hair with a spider silk (Figure 3.11) having much smaller diameter [42]. Recently, spider dragline silk has been demonstrated as a broadband acoustic sensor (MHz), owing to its high elasticity and sub-micron diameter. However, the response was detected using a doppler velocimetry [43]. Our universal interferometry offers a paradigm shift by opening interferometric route to silk-based nano-engineering devices on a chip that can potentially work in vacuum or in cryogenic conditions [44–46].

3.3 Universal iLens interferometer for photo-dynamics of solid, flame plasma and for liquids

3.3.1 Picometer resolved photo-dynamics of solid surfaces

Precise mechanical characterization of various materials and devices has always been a basic necessity for high-end technology. A sample exposed to electromagnetic radiation exhibits thermal effects through non-radiative processes causing the sample to expand or contract or to form a local bulge or dimple. Various physical quantities such as optical density, photo-thermal and photo-elastic response of materials, thermal expansion coefficient, etc., rely on measurement of such mechanical effects caused by external fields. Although many techniques exist for surface-deformation analysis of materials, such as Scanning Electron Microscopy (SEM) [47], X-Ray Diffraction [48], Photo-thermal deflection spectroscopy (PDS) [49], Atomic Force Microscopy (AFM) [50], Raman Microscopy [51]. Optical techniques based on Michelson [1] and Mirau [5] interferometers have also been demonstrated with advantages of being contactless, non-invasive, free of sample preparation yet offering precision in the nanometer or below.

In industries [52], interferometry is widely used, for example to measure crystal growth [53, 1], metrology [54], surface topography and surface temperature measurements [55, 56]. Most existing precision interferometers require optical quality components (beam splitter, mirrors, samples, etc.), which limits their application to smooth sample surfaces. A multi-component interferometer requires careful alignment and stabilization of each component against various noises. It is important and necessary to develop a minimal-component interferometric technique which is compact, and highly-precise to quantitatively measure deformations of smooth as well as rough surfaces in real-time.

Here, we use a robust single-lens interferometer and demonstrate its application in measuring local deformation of three samples with about 100 *pm* precision without any need for external calibration standard. We measured time-resolved photo-thermal mechanics of solid surfaces illuminated by a focused low-power pump laser by measuring the interference intensity through a photodiode and iris system. We demonstrate application of our setup to measure deformation dynamics of two representative rough samples (graphene-oxide and dried-blood) by obtaining interference pattern from their non-specular reflection. Such deformation dynamics may enable measurement of real-time change in local temperature of solid samples provided a prior knowledge of absorption coefficient and thermal expansion coefficient. Our setup will find application in studying laser cooling of solids as well [57–59] on sub-ns time-scales.

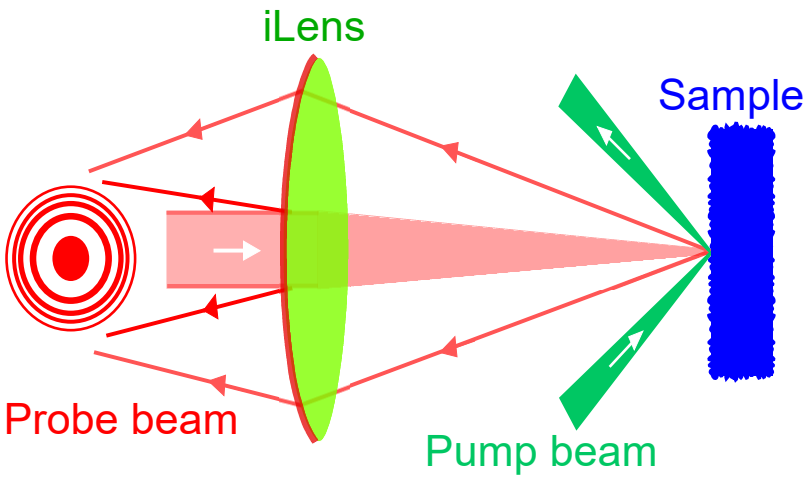

Fig. 3.12 **Schematic of single-lens interferometer for probing solid samples.** A low-power He-Ne laser (10 mW, $\lambda = 632$ nm) is used as a probe to produce interference fringes from the sample while another low-power green laser ($\lambda = 532$ nm) induces local deformation.

3.3.1.1 Experimental set-up

The schematic of our setup is shown in Figure 3.12. We used a collimated Gaussian beam of He-Ne laser (10 mW, $\lambda = 632$ nm, $1/e^2$ full waist $2w_0 = 1.0$ mm) to obtain high-contrast interference fringes from the sample surface using our versatile single-lens interferometer [60]. Our interferometer consists of a single partially silver-coated convex lens, iLens, which integrates the function of a beam splitter, a reference mirror and a light collector, which are generally derived from three or more optical components of any interferometer. Briefly, the incoming probe beam is divided into two beams, viz. reference beam and the object beam, at the front surface of the iLens. The iLens then collects the back-scattered light from the sample and project towards the screen where it combines with the reference beam to produce high-contrast fringes.

We measure picomechanical dynamics on three different sample surfaces, a smooth red-acrylic surface and two rough surfaces (producing non-specular reflection), namely, a dried blood drop and a graphene oxide thin-film prepared by drop-casting corresponding solution on a glass slide. We generated a reference modulation in the fringe-intensity by vertically displacing the sample by a known amount using a piezo stage (with calibration of 7.5 $V \approx 2$ μm). A half-fringe collapse in the signal corresponds to a sample displacement of $\lambda/4$ which equals to 158 nm in our case. We further resolve intensity using the PD with a resolution of dI, giving $dI = (I_{max} - I_{min})/N$, where N denotes the number of data points. The displacement resolution is then given by $\lambda/4N$ as shown in the schematic illustration of

Figure 2.6. For our case $N \sim 1000$ leading to a precision of ~ 150 *pm*. The intensity at the center of the fringes obtained was recorded on an oscilloscope using a photo-diode and a pin hole iris whose dimensions are chosen to obtain high-contrast in the interference oscillations. To determine the direction of deformation, the piezo stage was electronically displaced such that the length of the interferometric cavity was increasing relating a corresponding change in the interference fringe intensity.

The sample was locally deformed by focusing a low-power CW pump laser ($\lambda = 532$ *nm*, $P = 6$ *mW*) for varying exposure times. The pump laser was spatially overlapped on the probe beam on the sample and was made to incident obliquely as shown in Figure 3.12. The spot size of both the pump and the probe beam on the sample were around 300 μm and 400 μm, respectively (measured with a CCD beam profiler from Thorlabs). Since the spot size for probe was larger than the one of pump beam, the maximum deformation at the centre of the pump was recorded. We used a 650 $nm \pm 40$ *nm* band pass filter to block the unwanted stray reflection of the pump laser.

3.3.1.2 Results

3.3.1.2.1 Pico-mechanical dynamics of smooth surfaces To measure photo-induced deformation by *mW*-level pump beam, we biased the piezo-stage to be at the center of linear regime, i.e., of the interference intensity (shaded region, in Figure 2.6). The direction of deformation i.e. the formation of a bump or a dimple on the sample was a priory determined by relating the change in the interference intensity (increase or decrease) by displacing the sample in the known direction. With no pump exposure, a constant interference intensity was observed. The pump-exposure and the interference intensity was simultaneously recorded on the oscilloscope.

Figure 3.13(a) shows the deformation-dynamics of acrylic surface for $P = 6$ *mW* pump beam exposed for 5 *s* duration. We clearly observe a bulge induced by local heating followed by relaxation when the pump pulse was switched 'off'. During the heating period, the rate of collapse of fringes tends to reduce and the sample deformation reaches a maximum value at the end of pump-pulse (corresponding to maximum temperature) as shown in Figure 3.13(b). After the pump exposure the sample relaxes back to its original state (corresponding to cooling back to initial temperature). Note that for such low-power laser the deformation is fully reversible without any permanent physical state change. The magnitude of deformation in Figure 3.13(b) is calculated by extracting the phase corresponding to the recorded intensity variation. The deformation in the sample was added successively after every half fringe collapse corresponding to $\lambda/4 \approx 158$ *nm*. The displacement resolution in our measurement is sub-100 *pm* shown in the inset of Figure 3.13(b).

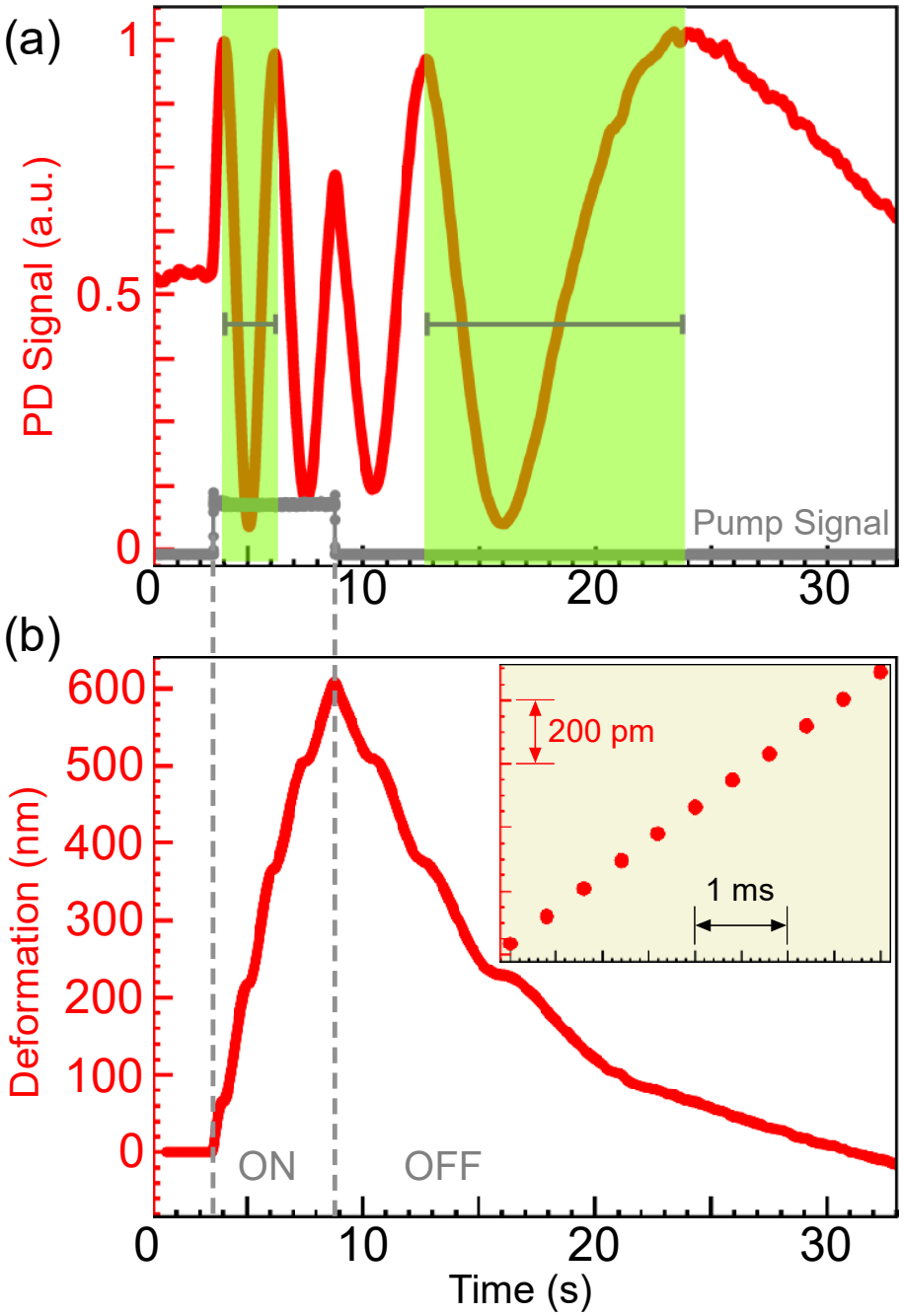

Fig. 3.13 **Measurement of time-resolved deformation of the acrylic surface induced by a pump laser**. (a) The interference intensity and corresponding pump signal (shown in grey). A shutter is used to control the pump exposure. Note the time-interval between fringe-maximum varies. (b) The deformation of the sample surface with 150 *pm* precision.

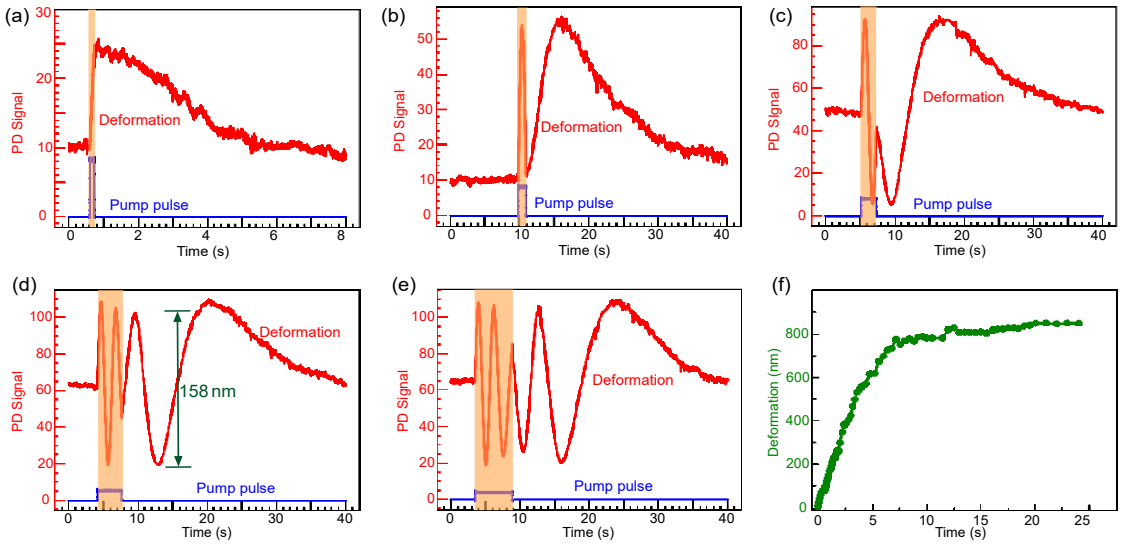

Fig. 3.14 **Deformation dynamics of acrylic for fixed $P = 6mW$ at different exposure times.** (a) 100 *ms*, (b) 1 *s*, (c) 2 *s*, (d) 3.4 *s*, (e) 5.2 *s*. (f) Maximum deformation at the end of pulse shows a saturation for pulse exposure greater than 7.5 *s*.

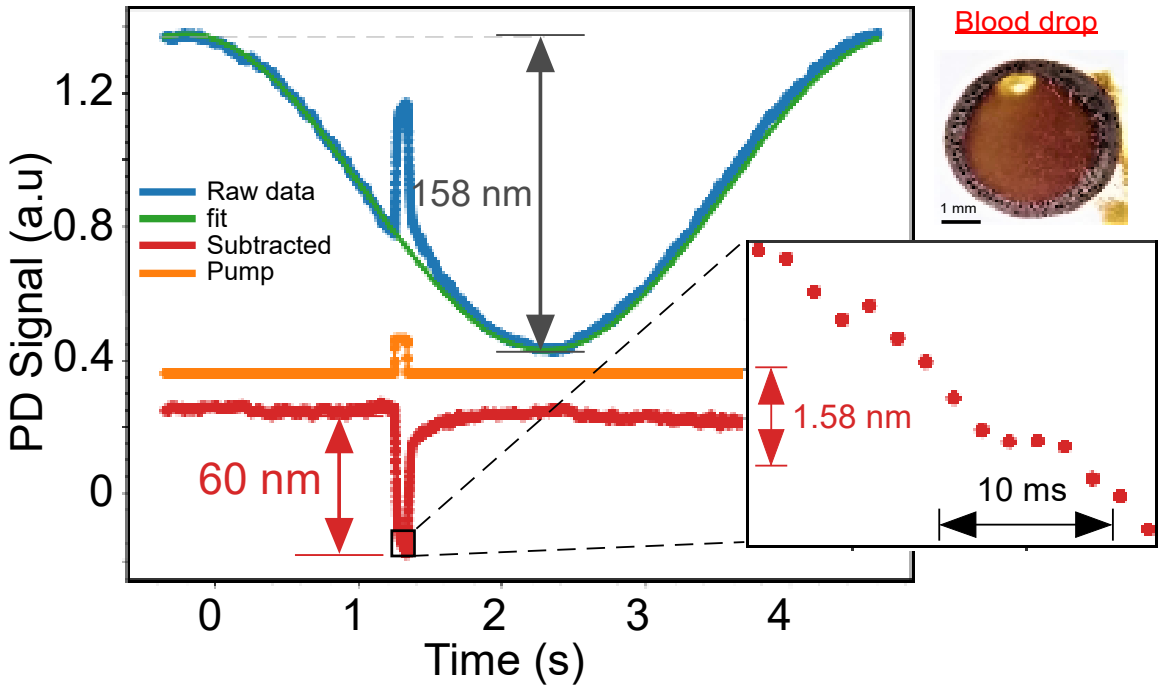

Fig. 3.15 **Time-resolved laser induced deformation of rough samples.** Deformation dynamics of blood-sample for = 500 μW and 80 *ms*. The upper right inset shows the image of a dried blood drop on a glass slide.

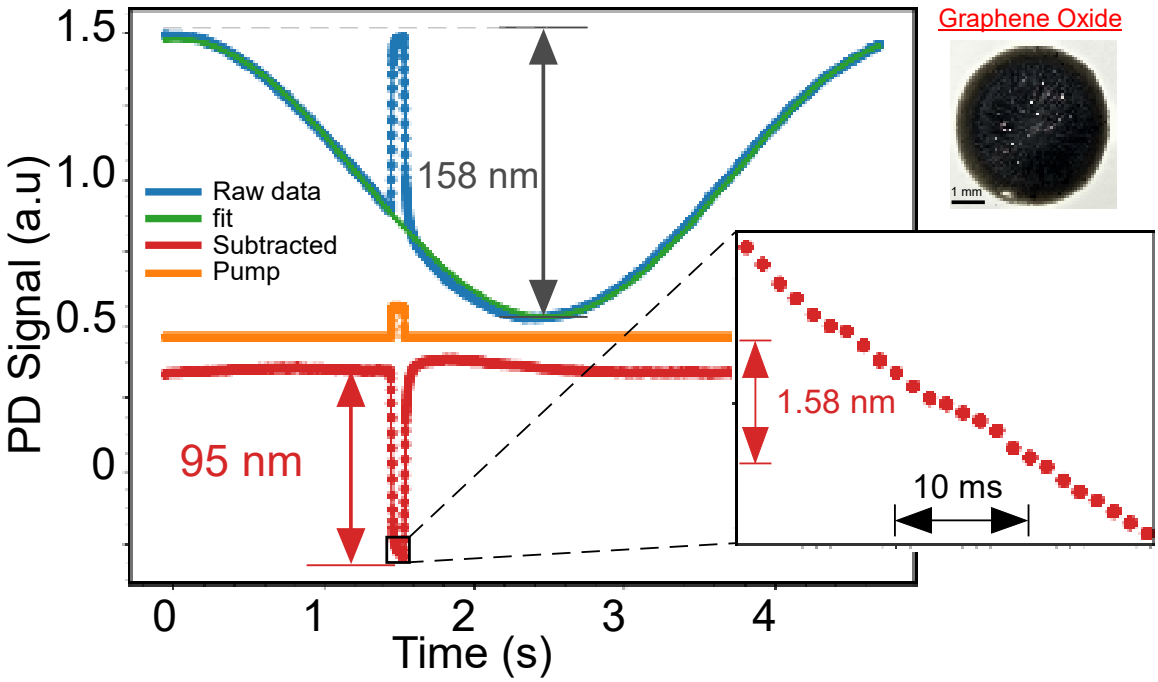

Fig. 3.16 **Time-resolved laser induced deformation of rough samples.** deformation of graphene oxide film for $P = 4.7\ mW$ and 80 *ms*. The upper right inset shows the picture of graphene oxide film drop casted on a glass slide.

The deformation dynamics of acrylic for different exposure times from 40 *ms* to 25 *s* is shown in Figure 3.14. We observed that for a fixed pump power, a longer exposure time produces a larger deformation as shown in Figure 3.14(a-e). The deformation in the sample attains a maximum value (for $\approx 7.5\ s$ exposure) and then remains at this value for longer exposure times as shown in Figure 3.14(f). We attribute this behaviour to the fact that the sample has attained its maximum temperature and reached thermal equilibrium. If higher power laser is used a permanent damage to the sample can be observed.

3.3.1.2.2 Displacement of rough surfaces To measure the displacement of rough sample, we prepared two samples, namely a dried blood drop and a graphene oxide film on a glass-slide by drop-casting method (see Figure 3.15, 3.16 for real-picture of the samples). Remarkably, our single-lens interferometer was able to collect non-specular reflection from these samples and obtained fringes. Using the above described approach of fringe analysis, we observed displacements of 60 *nm* and 95 *nm* respectively with a real-time resolution of 200 *pm* for the two samples as shown in Figure 3.15, 3.16.

With these photo-induced mechanical deformation of various samples, our technique can also be used to estimate the change in the local temperature of the sample. At *mW*-level laser

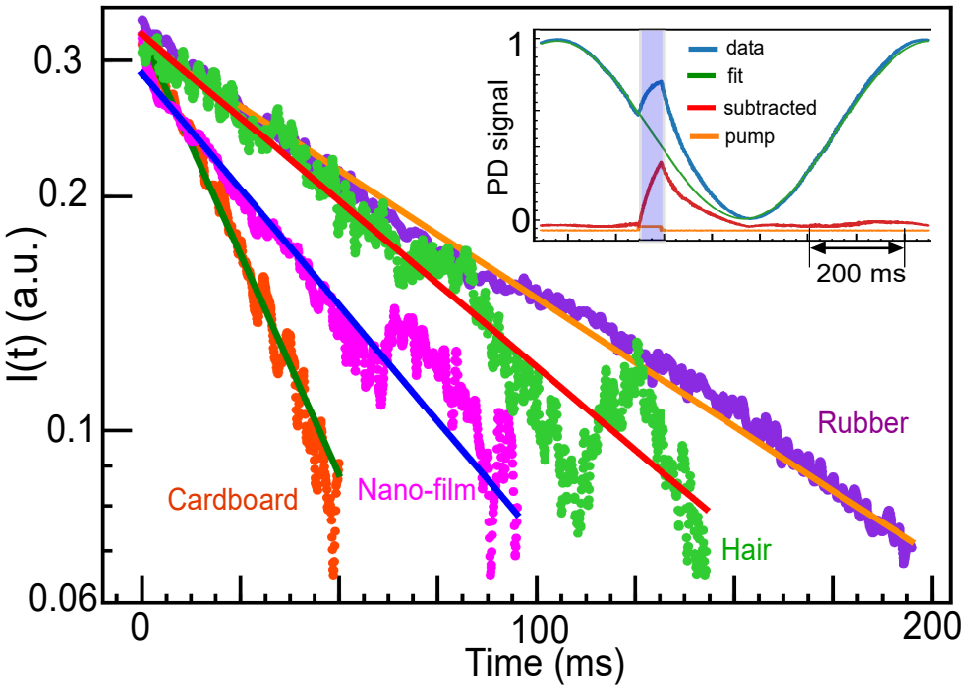

Fig. 3.17 **Measurement of thermal diffusivity.** Thermal relaxation of four samples after switching off the laser with corresponding exponential fits (solid lines). Inset shows typical response for 80 *ms* pump exposure.

power the solid sample mostly expands locally due to the absorption of heat. The magnitude of radiation pressure force is expected to be in pico-Newton (of the order of P/c, where c is the speed of light), and the resulting mechanical deformation on solids is beyond the detection sensitivity of our technique. In our experiments, absorption of laser causes sample to heat locally and the induced thermal stress is balanced by the elasticity of the material. Knowing the thermal expansion coefficient and elasticity modulus of the material, geometry of sample and its optical absorption coefficient one can quantitatively estimate the local temperature change in the sample [61, 62]. While a detailed modelling will be of interest, our approach may help to isolate competing effects of radiation-pressure and heating towards developing a better understanding of light-matter interaction in rough samples.

3.3.1.3 Measurement of thermal diffusivity

Furthermore, although the two fundamental effects of light-matter interaction, i.e., a mechanical transfer of optical momentum and optical heating are observed in all our samples [63], our technique can be leveraged for isolating photothermal strains with picometric preci-

S. No.	Material	$t_c^{-1}(s^{-1})$	Exp. Diffusivity Values (m^2s^{-1})	Known Diffusivity Values (m^2s^{-1})
1	Si Rubber	7.59	1.82×10^{-7}	$(0.89-1.3) \times 10^{-7}$ [67]
2	Al filter	31.44	7.55×10^{-7}	8.1×10^{-7} [68]
3	Cardboard	35.62	8.56×10^{-7}	11.8×10^{-7} [69]

Table 3.1 Comparison of the thermal diffusivity of four samples used in our experiment against their known values.

sion. Inset in Figure 3.17 shows typical thermal-response of a silicon rubber sample along with the $sub-mW$ level heating laser pulse ($\lambda = 532\ nm$, spot diameter $2\omega_0 = 300\ \mu m$). In Figure 3.17, we plot the post-pulse relaxation dynamics of four samples including the human hair and a fragile 200 nm thickness freely suspended Al-film. Our data exhibited an exponential relaxation, $\delta h \sim e^{-t/t_c}$ with a characteristic time constant t_c. Using the standard heat-diffusion model [64], the t_c allowed us to determine the thermal diffusivity D of the sample as $D = \omega_0^2/4t_c$. The thermal diffusivity values for our samples agreed well with their known values (Table 3.1) [65], showing that universal interferometry enables non-invasive and precise measurement of physical properties of various rough or structured bio-materials, which might not be possible with conventional optical techniques such as beam profilometry or IR thermometry [66].

The photo-thermal properties of the solid sample (or micro fiber) can also be isolated in the transverse plane by probing the sample using our iLens interferometer from two directions of the plane as shown in Figure 3.18.

3.3.2 Study of candle flame plasma

3.3.2.1 Introduction

Plasma, the fourth state of matter, can be created in a wide variety of situations, for example, from lightning in the atmosphere, high-voltage breakdown of materials, in intense laser-matter interactions to a candle flame. Understanding various physical properties of plasma is important to devise novel applications in material processing and biomedicine. A simple example of a plasma medium, that is easily accessible to everyone, is a candle or a spirit lamp flame. While flames have been an integral part of our lives and a subject of human curiosity since ancient times, it was only in 1825 when Faraday performed inquisitive experiments

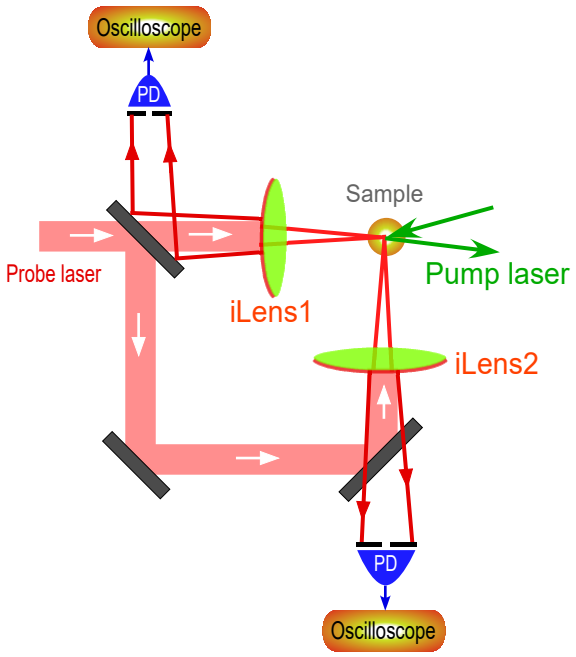

Fig. 3.18 **Schematic describing double-axis iLens interferometer to isolate the photothermal properties of the sample in the transverse plane.**

on candle flames that revealed different temperature and charge distribution in the flame [70, 71]. His experiments offered qualitative insight into the properties of the flame plasma, however, due to intrinsic dynamical character of the flame, a quantitative and non-invasive measurement of its properties remained a challenge.

Previously, many invasive and non-invasive techniques have been performed to characterize various regions of the flame. For example, a thermocouple has been used to directly measure the change in flame temperature [72]. This single point measurement disturbs the flow inside the flame, in addition, deposition of soot particles on the surface of thermocouple also affect accuracy of the temperature measurement, and hence, contributing to a major source of error. Non-intruding optical techniques for characterizing the flame include interferometry [26, 73–77], holography [78–80], sspeckle techniques [81], Rayleigh scattering [82], Coherent Anti Raman Scattering [83], color-ratio pyrometry using DSLR camera [84]. The experiments performed with these methods are not only tedious but also require a lot of sophisticated analysis to achieve precision measurements. Furthermore, most measurements till date have been done at a single point (within a limited focal volume) in the flame rendering a precision of sub-μm. Holography can simultaneously measure the entire spatial profile of the flame, but the speed of measurement is limited by image acquisition and processing. Flickering dynamics of flame due to different fuel types in different atmospheres [85, 86], and under various gravity fields [87] have also been studied at various timescales.

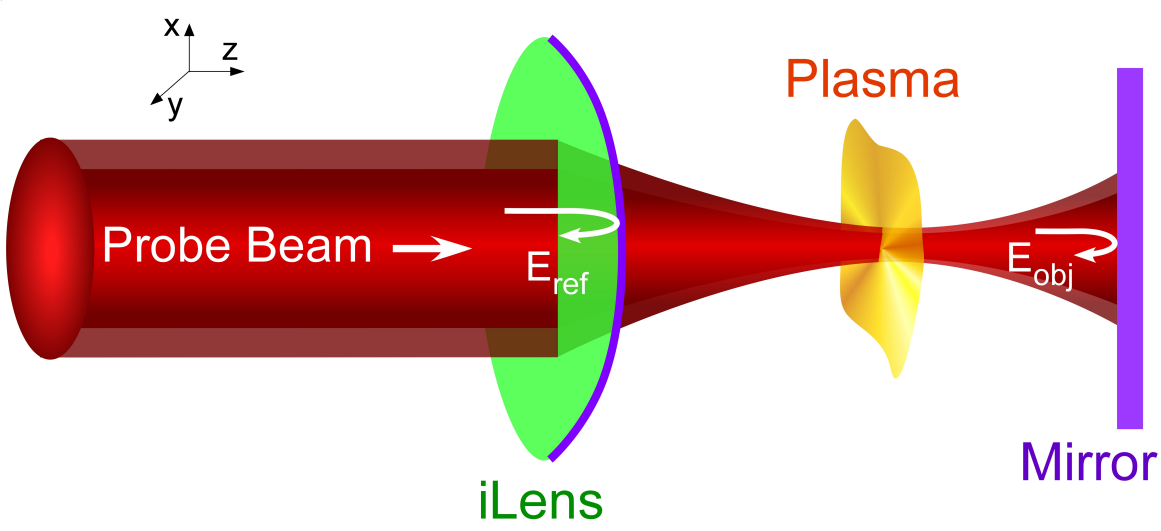

Fig. 3.19 **Schematic describing idea of using iLens interferometer for probing plasma.**

However, there is a lack of simple yet precise tool to measure the dynamical properties of plasma in real time.

Although interferometers have been widely used to study the three states of matter viz. solid, liquid, and gas but few have been used to study the fourth state of matter, i.e. plasma. The laser interferometers are precision devices for various measurements; however, the setup should be compact, and the noise-floor should be low to make a precision probing of plasma. Standard interferometers are based on either amplitude division or phase division, such as Michelson, Fabry-Perot, Mirau, Fizeau interferometer, etc. [1, 4–6]. Recently, we have designed and demonstrated a compact single iLens interferometer [60, 88] that was shown to produce fringes with most common (flat and rough) surfaces enabling tens of pm precision in real-time. However, iLens interferometer has not been shown to work with any plasma medium yet. Though there are many techniques to study the profile of the candle flame but very few experiments have been performed to study the flame at atomic level. We know that the excited atoms emits light during relaxation and it happens at a very fast time scale of $\approx ns$. So, one may wonder if it is possible to use the unprecedented precision and speed offered by interferometry to find the new insights of the flame at atomic level.

Here, we demonstrate our simple and compact iLens interferometer to study the photo-mechanical dynamics of the full candle flame with pico-meter precision in the optical path. A full 2D-profile of the candle flame was obtained from the phase information of the interferometer. We also found the point-by-point refractive index and temperature profile of the different regions inside the flame. Lastly, we studied the plasma formation inside

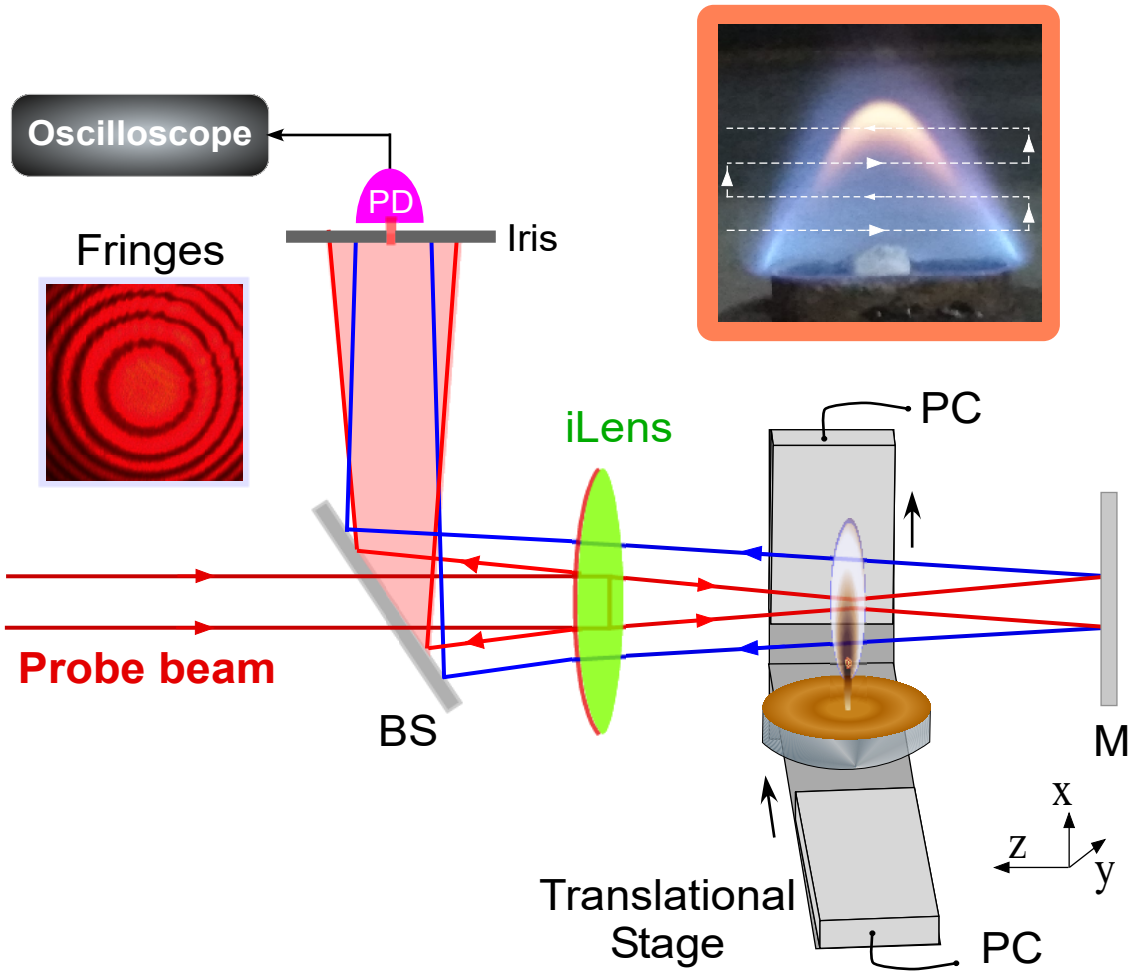

Fig. 3.20 **Schematics of the experimental set-up**. A He-Ne laser ($\lambda = 632\ nm$, $10\ mW$) is used to obtain the interference fringes from the mirror surface using the iLens interferometer. A candle flame placed on a 2D translation stage in the interferometric cavity at the focal point of the iLens. The upper right inset shows the real picture of the flame with the scan direction.

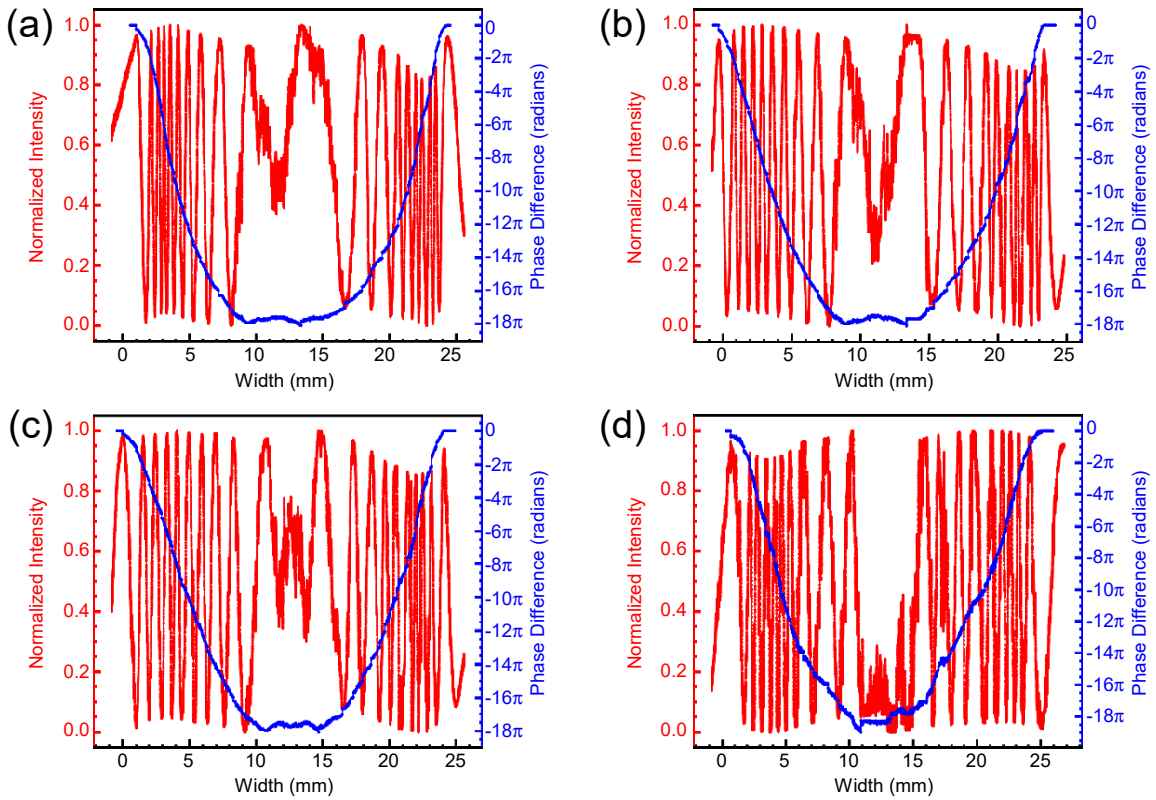

Fig. 3.21 **Intensity and Phase plot of the flame at different heights**. (a-d) shows the phase change in and around the flame with the intensity profile at a height of 6 *mm*, 14 *mm*, 22 *mm*, and 27 *mm*, respectively, from the wick of the lamp.

the flame by perturbing it with a high-power nano-second laser and observed an interesting phenomena of locally extinguishing the flame above the plasma formation.

3.3.2.2 Experimental set-up

The basic idea for probing plasma medium with our interferometer is described in Figure 3.19. The compactness of our setup is rendered by iLens which combines three functions in one element, generally accomplished by three or more separate components in a traditional interferometer, namely beam splitter, reference mirror, and light collector. An incoming Gaussian beam serves as a probe to produce high contrast fringes by overlapping a reference beam, coming from iLens, and an object beam, from a flat mirror onto a photodiode. The plasma medium is kept inside the iLens cavity at a suitable location and any change in its properties imparts a further change in the optical path length of the interferometer producing a change in the interference intensity.

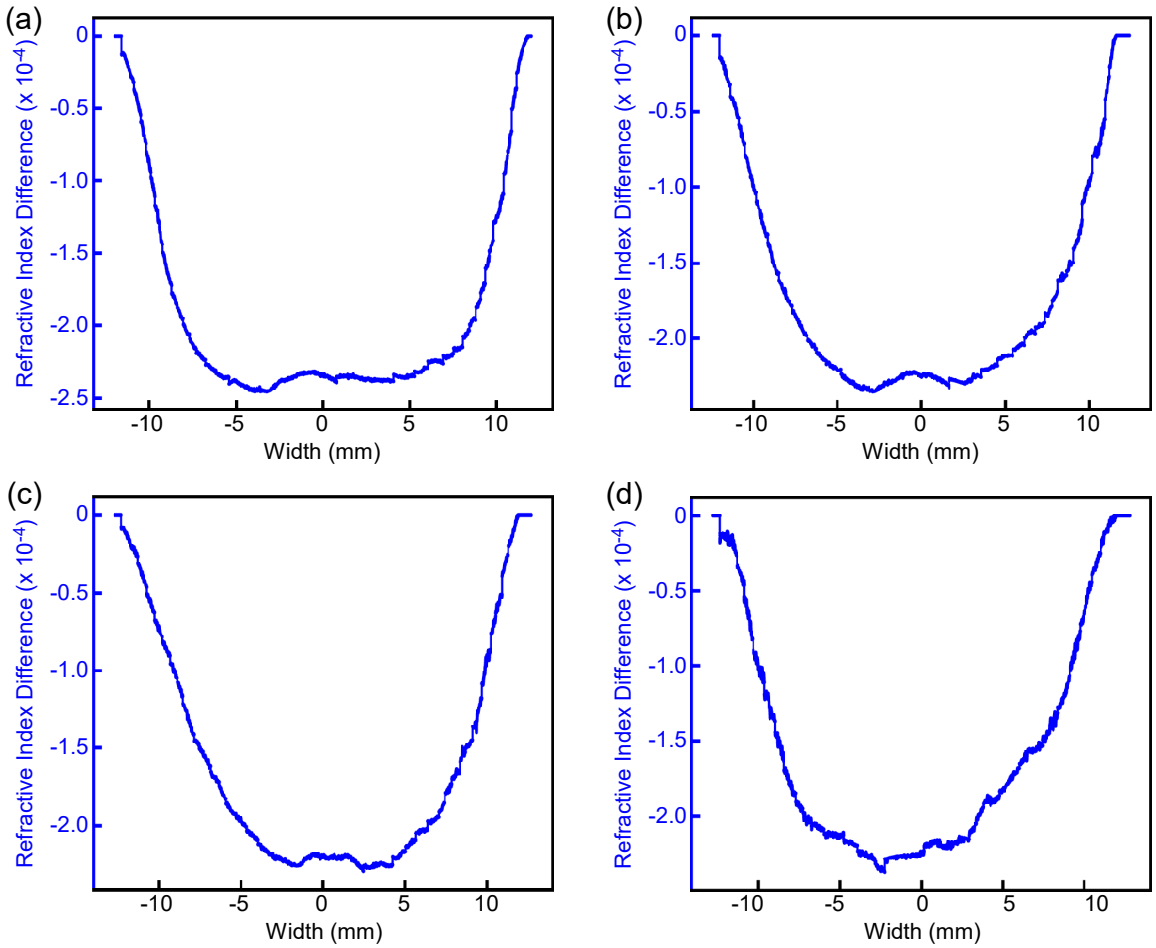

Fig. 3.22 **Change in the refractive index of flame**. (a-d) shows the refractive index difference in and around the flame at a height of 6 *mm*, 14 *mm*, 22 *mm*, and 27 *mm*, respectively, from the wick of the lamp.

The detailed setup for probing the flame plasma is described in Figure 3.20. The commercial spirit lamp flame was placed inside a collinear interferometer cavity consisting of the iLens and a mirror [60, 88]. Prior to placing the flame, the iLens interferometer was adjusted to produce high-quality fringe from the mirror surface. In this experiment, we used a partially coated (60 : 40) convex iLens along with a He-Ne laser beam (10 mW, $\lambda = 632$ nm, and $1/e^2$ full waist $\simeq$ 1.0 mm). The high-contrast circular fringes were produced by superimposing the reference beam (reflected from the coated side of the iLens) with the object beam (reflected from the mirror). The ethanol flame mounted on a 2-D translation stage, with 50 mm scan range, was kept in the interferometer cavity at the focal point of the probe laser. The flame was scanned slowly by 2-D raster scanning along the measurement path (upper right inset of Figure 3.20) at a speed of 1 mm/s. The presence of the flame plasma in the iLens cavity

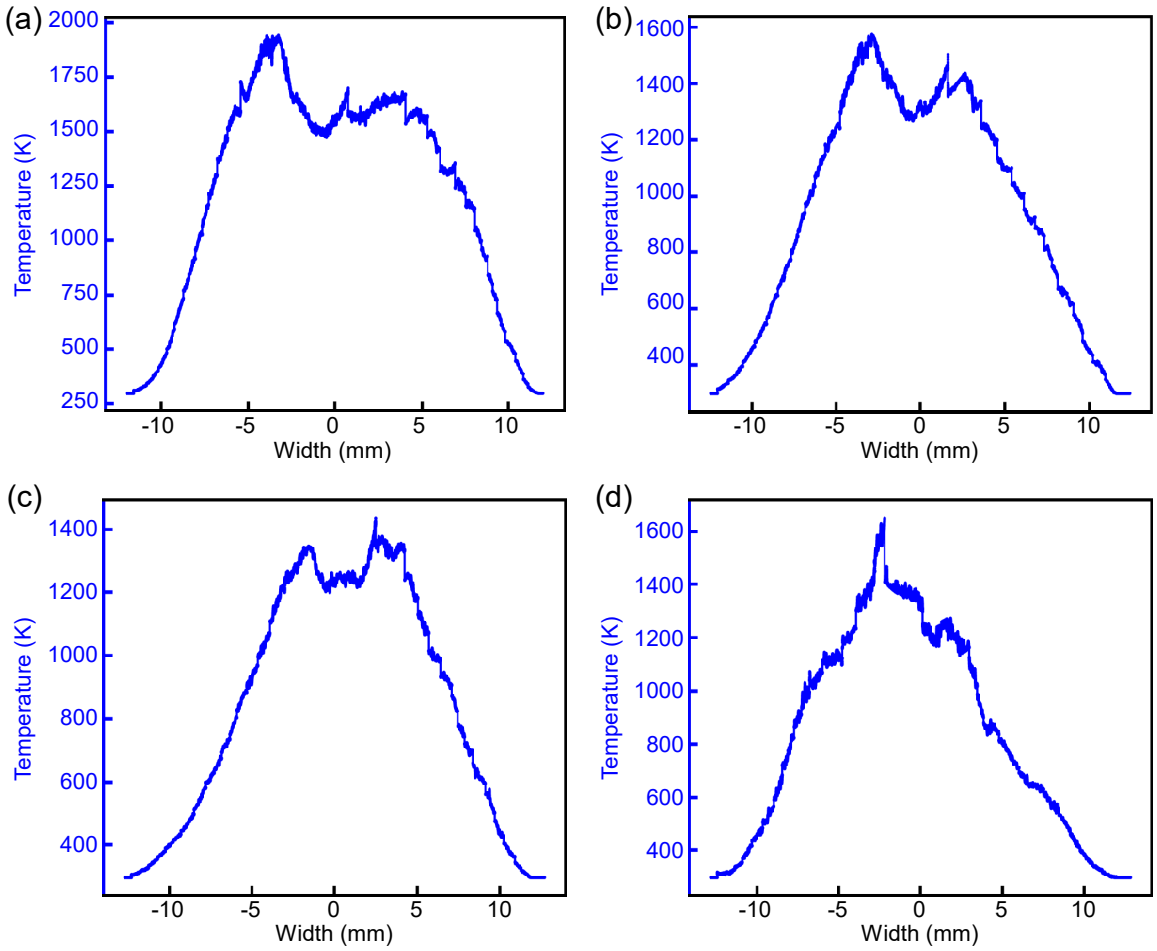

Fig. 3.23 **Temperature profile of the flame at different heights**. (a-d) shows the corresponding temperature of the flame with respect to temperature of the air.

varied its optical path length and produced dynamic fringes. To measure the full 2-D profile of the flame, we measured the central intensity of the interferogram with a fast photodiode (rise time 1 *ns*) and an iris.

3.3.2.3 Theory

Since all the measurements of interference intensity is done through an iris and PD along the axis of the interferometer. The dimension of the iris opening is around 0.8 mm^2 which is chosen much smaller than the typical fringe width to obtain high-contrast fringes in the detector plane. In this situation, the curvature of the reference and sample wave fronts falling on the detector plane (x,y) is too large and well approximated by a plane-wave near (x_0,y_0). The length of the cavity d(t) varied due to the change in the density of ions in the different regions in the flame. As discussed in the previous chapter the local intensity of the

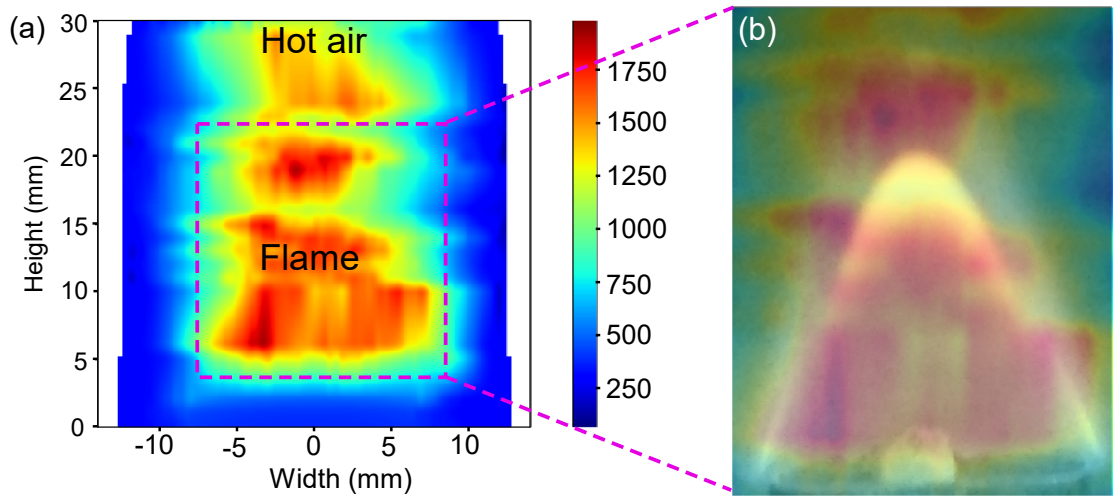

Fig. 3.24 **Reconstruction of the flame.** (a) 2D color plot of the flame. The color bar represents the temperature (in K) of the flame. (b) Superposition of the real image and the 2-D color plot of the flame.

interference pattern follows the cosine square law, given as:

$$I = I_0 \cos^2(\Delta\phi/2) \tag{3.1}$$

where ϕ is the phase difference between the reference and the object beam. The relative phase change in the two beams of the interferometer can then be extracted using the equation:

$$\Delta\phi = 2\cos^{-1}\sqrt{(I/I_0)}, \tag{3.2}$$

where I/I_0 is the normalized fringe intensity. It should be noted that since flame is a rarer medium than ambient room-temperature air, so, a subsequent 2π subtraction is done while calculating the phase change. The red curve in Figure 3.21(a-d) shows the intensity change recorded at the oscilloscope when the flame enters and exits the interferometric cavity. The blue curve shows the phase extracted from the intensity curve at a height of 6 *mm*, 14 *mm*, 22 *mm*, and 27 *mm* respectively from the base of the flame. Please note that as the flame enters the cavity from the left the initial fast oscillations is due to the change in the temperature of the surrounding air. The almost constant intensity (slow change) at the center of the graph is when the laser passes through the flame. Then again as the flame leaves the cavity we could observe the fast oscillations in the intensity plot due to changing density of the ambient air due to change in its temperature.

The refractive index difference at every point inside the flame was then calculated using the equation

$$\Delta\eta = \eta_1 - \eta_2 = (\lambda/2\pi)(\Delta\phi/a), \tag{3.3}$$

where $\eta_{1,2}$ is the refractive index of flame and air respectively, λ is the wavelength of the laser, $\Delta\phi$ is the phase change and a is a geometric path length as described in detail in [78]. Figure 3.22(a-d) shows the change in refractive index as the flame progresses in the interferometric cavity at different heights of 6 *mm*, 14 *mm*, 22 *mm*, and 27 *mm*.

The temperature of the flame at each point at a particular height can then be calculated using the following equation:

$$T = \frac{T_0}{\left(\frac{\Delta\eta}{\rho_0\beta}\right) + 1}, \tag{3.4}$$

where, T_0 is the room temperature and the value of $\rho_0\beta$ for organic fuels is 0.28×10^{-3}. Figure 3.23(a-d) show the plots of the temperature of the flame at different heights of 6 *mm*, 14 *mm*, 22 *mm*, and 27 *mm*, respectively. The refractive index values and the temperature of the flame are in agreement with the literature [89, 78, 80]

The temperature profile at all the heights was used to obtain the 2-D color plot of the entire flame as shown in Figure 3.24(a). The color bar represents the temperature (in K) of the flame. As the flame enters the interferometric cavity the temperature increases upto 1800 K, and it decreases as it leaves the cavity. In Figure 3.24(b) the real image of the flame is superimposed with 2-D color plot of the flame region only. One can observe the one-to-one correspondence between our quantitative measurement and the actual picture of the flame.

3.3.2.4 Study of Flame at nano-second time scale

In another demonstration we measured the pico-scale dynamics in the flame when excited with a nano-second laser ($\lambda = 532$ *nm*, pulse width = 30 *ns*). The maximum average and peak power of ns-laser was 1300 *mW* and $\approx$ 100 *kW* respectively at a frequency of 2600 *Hz* and an input voltage of 8 *V*. As soon as the pump laser was made incident on the flame, a plasma is formed along the pump laser path. The soot particles present inside the flame breakdown/ionize at this high power to produce plasma inside the flame. The distinctive plasma sound can be heard clearly when the pump laser interacts with it.

To further study the flame at nano-second time scale, we placed a shutter (Thorlabs SH05) and a chopper (Thorlabs MC1F10HP) in front of the ns-laser. By varying the operational frequency of shutter and chopper, we tried to separate out the response of the flame due to a

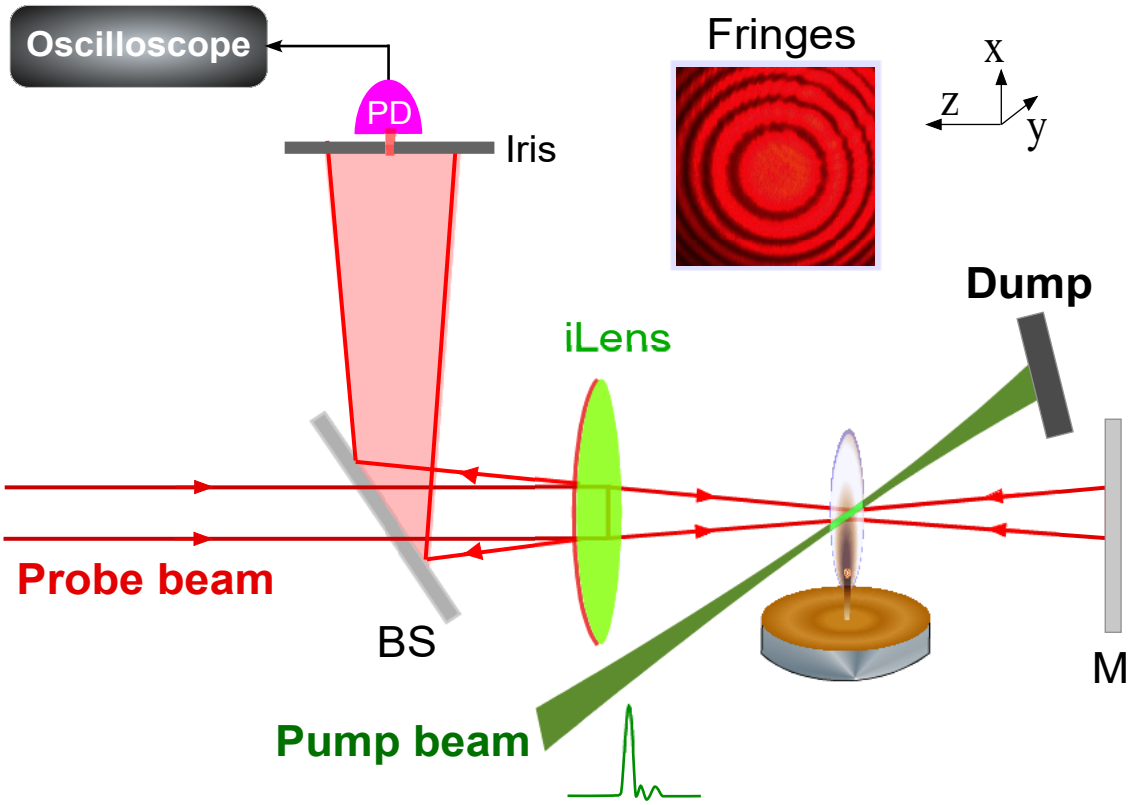

Fig. 3.25 Schematics of experimental setup to probe the flame with nano-second laser.

single ns-pulse. A change of few *nm* was observed due to a single ns-pulse of peak power 100 *kW* in Figure 3.27. We also noted that as soon as the plasma is formed, a cut/slice (Figure 3.26) in the flame was observed all the way up to the height of the flame. The appearance of dark-slit in the flame, above the laser interaction point, following interacting with high laser power can be due to scattering of the soot particles on breakdown and hence, are not able to escape just above the plasma formation. The appearance of the dark spot is robust and fully reproducible. We speculate that this dark band could be a result of photo-de-excitation of the excited molecules or it could also result from a fragmentation of the flame molecules by the nanosecond laser pulses which could also suppress their photo emission properties. More experiments and modelling is needed to fully understand this intriguing phenomenon.

3.3.3 Potential application of iLens to probe liquids

We have also designed set-ups to probe fluid surfaces and fluid volume with high precision and with ease. Although, we do not show the detailed results in this thesis, we sketch the possible setups and report preliminary results validating applications of iLens interferometry for opto-fluidic experiments.

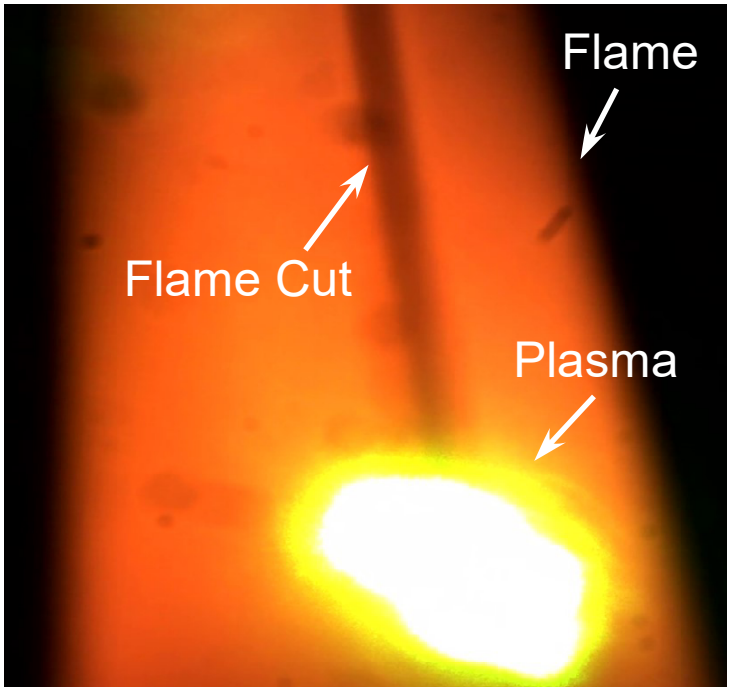

Fig. 3.26 **A picture of a vertical dark-band in the flame** created by the ns-laser interaction with pristine flame. Note that the flame is seen through a filter while the ns-pulses are continuously exposed.

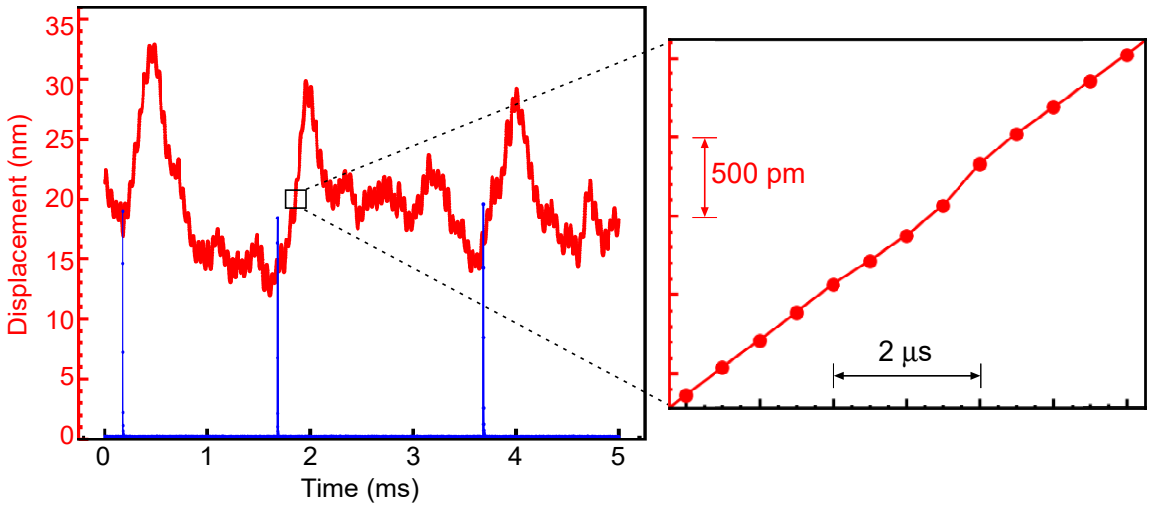

Fig. 3.27 **Probing flame with nano-second laser**. shows the deformation in the flame due to 125 ns-pluses of 50 *ns* period each. The zoom at the right side shows the resolution of ≈ 150 *pm*.

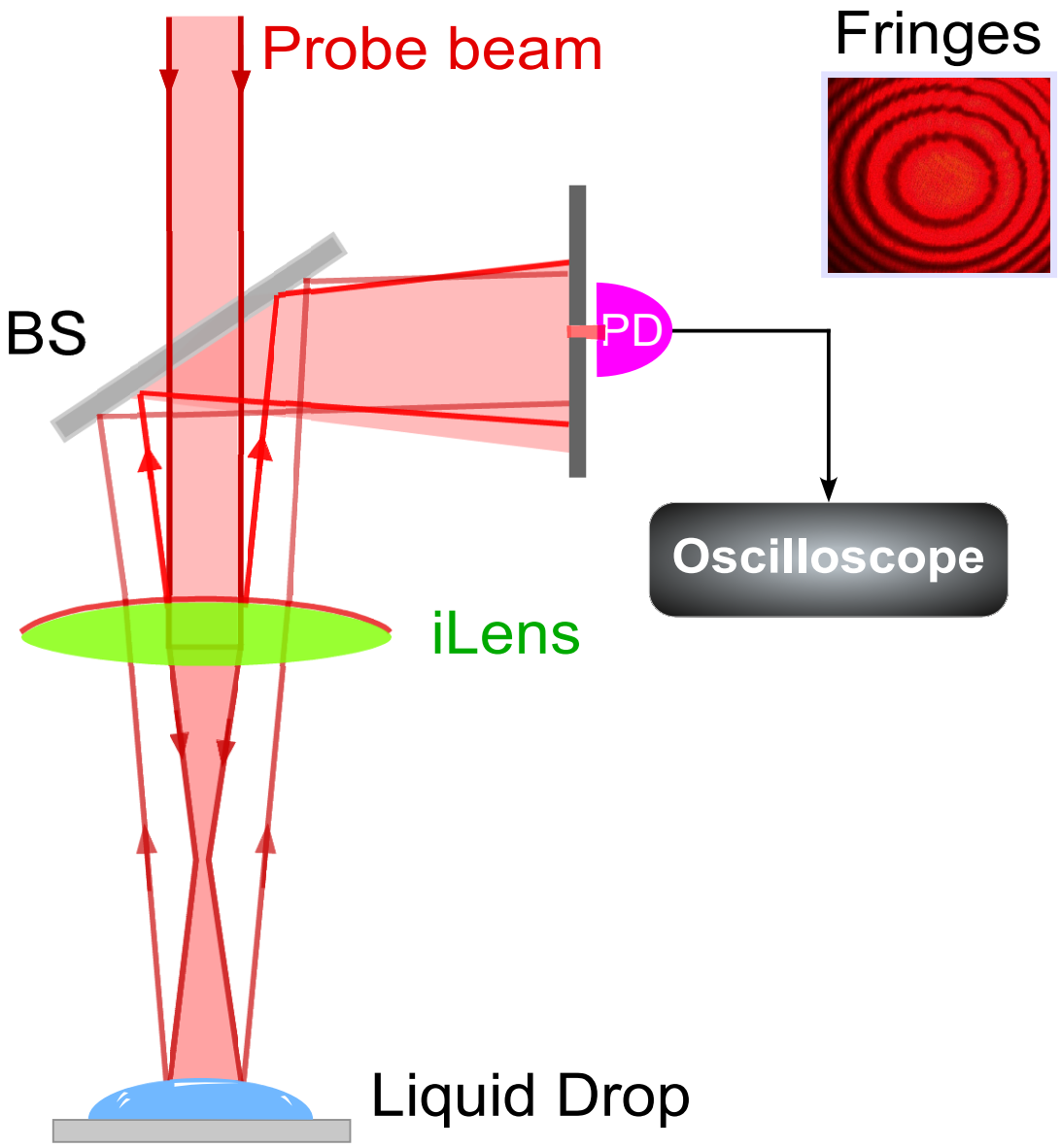

Fig. 3.28 **Schematics of the experimental set-up to probe liquid surface**. A He-Ne laser ($\lambda = 632\ nm$, $10\ mW$) is used to obtain the interference fringes from the surface of the liquid drop sample using the iLens interferometer. This can be used to study the various properties of liquid like evaporation rate, viscosity, etc.

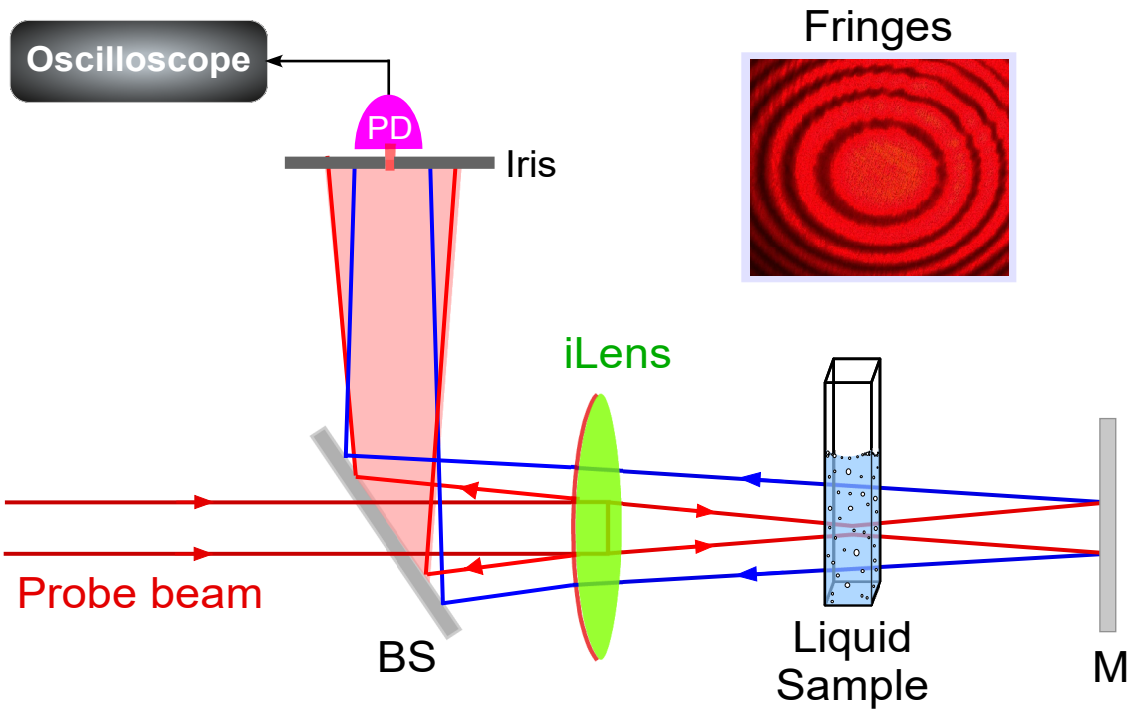

Fig. 3.29 **Schematics of the experimental set-up to probe liquid sample**. A He-Ne laser ($\lambda = 632\ nm$, $10\ mW$) is used to obtain the interference fringes from the mirror surface using the iLens interferometer. A cuvette with the liquid sample is then kept in the interferometric cavity to study the volumetric changes in the sample.

We demonstrate two different setups for probing surface deformation and volume effects. As shown in Figure 3.28, & 3.29, iLens interferometer forms high contrast interference fringe from the curved surface of a fluid drop. The iLens produces high contrast Michelson-like circular fringes from the drop surfaces. Such fringes have been previously obtained with a liquid-drop interferometer (LDI), however, LDI works best with semi-transparent fluids [90–92]. In the case of highly absorbing or turbid fluids, the LDI would not work well. Since iLens uses the back-reflection from the fluid surface, it will offer advantage over LDI for highly absorbing fluids, gels, and turbid fluids like milk. In addition, the iLens technique can also be adapted for multi-point measurement by obtaining fringes from two spatially separated points on the fluid surface. Such multi-point interferometer could find applications to resolve surface dynamics (capillary waves, dispersion) of fluids subjected to optical or electrical excitation.

The iLens can also be setup to probe volume effects such as change in the refractive index of fluids by heating or resulting from chemical mixing. One can place the desired fluid inside the iLens cavity and record changes in the optical thickness of the fluids using methods as

discussed in Chapter 2 and 3. The above example highlight unique advantages of iLens for precision measurements from solids to gaseous medium.

3.4 Conclusion

In this chapter, we have demonstrated two different kinds of applications of the iLens interferometer. On the one hand, we exploited iLens to fabricate frugal optical devices with ultrahigh sensitivity, including a paper based pico-balance, a cloth-based acoustic sensor and a force sensor using human hair. We established a calibration procedure and also compared them with the state-of-the art available commercial devices.

On the other hand, we demonstrated that iLens enables direct measurement of arbitrary solid surfaces exposed to another laser with picometer precision in real time. The iLens also enables probing a candle flame plasma with sub-nanometer precision that allowed us to probe the dynamic properties of the flame. We observed a new phenomenon, whereby a nanosecond laser causes the candle flame to quench, observed by a dark-band in the bright flame. The iLens interferometer enables real-time probing of the local changes in the flame. Although, the exact mechanism of this effect remains unknown and is under investigation. Lastly, the iLens is a universal interferometer that also enables probing of absorbing liquid surfaces and the volumetric changes in a liquid.

In the following chapter, we shall further develop the iLens interferometer to design a compact picometer resolved interferometer with shaped light, in particular, using light possessing orbital angular momentum.

Chapter 4

Twisted Cylindrical iLens Interferometer and Application of light sheet

4.1 Introduction

We have established that the iLens interferometer with the Gaussian beam produces high-contrast fringes and enables picometer resolution with not only for arbitrary solid surfaces but also for candle plasma and fluids. The compactness and picometer real-time precision allowed fabrication of a new class of frugal optical devices and also to probe various fundamental light-matter interaction.

With the recent advances in producing structured light, such as in generation of light possessing orbital angular momentum (OAM), it is natural to explore whether structured light offers new feature in an interferometer which are generally not possible by conventional Gaussian beams.

Many previous attempts have been made to design Michelson, Mach-Zhender, Young's double slit interferometers with the twisted light. These interferometric schemes allow direct determination of topological charge in the beam. Michelson interferometer with twisted light was shown to produce a daisy flower-like fringe pattern that rotated clockwise or counter-clockwise direction when one arm of the beam was displaced forward or backwards. Naked eye detection of picometer precision was proposed by looking at the angle of rotation of the petal pattern [93, 94]. However, measurement of rotation angle, requires the image to be recorded with a camera that make the measurement slow. In addition, the twisted light interferometers have multi-components, that make such setups difficult to align and stabilize. Our objective in this chapter is two-fold. First, we would like to design a compact cylindrical iLens based interferometer with twisted light, and, second, we would like to propose a simple detection scheme to measure the picometer displacement in real-time. Besides, we will

show a unique advantage of the twisted light in noise self-cancellation of certain noises present in an interferometer, which will facilitate detection of weak signals with twisted iLens interferometer.

In the second part of this chapter, we will present an interesting application of cylindrical lens, whereby we generated ultra-fast light sheet for large-area surface patterning of solid surfaces. Such large-area surface patterns serve as reference surfaces for various applications, including measurement of surface topography and optical components.

4.2 Noise self-compensating signal-amplifying twisted CiLens interferometer

4.2.1 Introduction

Noise is a fundamental limitation in precision optical interferometers. Minimizing noises has been a major challenge to boost the sensitivity of optical interferometers. Usually the interferometer is set on the dark fringe in order to reduce the noise floor [11], which also affects the detection of true signal. The coupling of laser and the thermal fluctuations in the mirror has been reduced by using beams with larger spatial profiles, such as flat-top beams [95] or higher order LG beams [96], thus reducing the noise by averaging it over a larger area [97]. Other methods to reduce the effect of different noises include Fourier-filtering of known noise frequency from the data [13, 98]. These techniques generally require the subtraction of two or more images from the object taken at different time, thus requiring more memory and analysis time. Injection of squeezed light in interferometer allows broadband noise reduction [squeezed]. Owing to the multi-component systems, most techniques are tedious to align and make the setup complex and bulky. Importantly, cancellation of noise in real-time has been a challenge to detect picometer scale signals deeply submerged in noise.

Light possessing orbital angular momentum (OAM) has enabled extraordinary vast applications such as in trapping and twisting tiny objects, optical communications and interferometry [99, 100]. The spiral interferometry overrides the basic problems of conventional interferometry in that it allows to distinguish a bump or dimple in the phase sample by the direction of spiral fringes [101–103]. The OAM light has been employed in interferometers, such as in Michelson-type interferometer [93, 104–106, 94], for precision metrology as well as to quantify the topological phase. Detection of linear displacement of one of the mirror produces a screw-like rotation of the interference pattern, therefore, linear displacements have been measured by detecting rotation angle of the interference pattern. However, measurement of rotation angle demands measurement of petal-edge with image-analysis. Although, naked

eye detection of rotation is simple but is limited by ms-scale persistence of vision. A simple scheme leveraging real-time detection of picometer resolution with twisted light is missing. Besides, most of the existing twisted interferometers are multi-component systems which must be stabilized and carefully isolated from noises to render precision measurements.

Here, we introduce an ultra-compact twisted interferometer that self-compensates noise in real-time while also amplifying signal by exploiting the spiral phase structure of twisted light enabling detection of ultra-weak signal deeply buried in noise. We exploit nearly perfect anti-correlation of a pixel-pair chosen on a petal of daisy flower-like interferogram to generate an intensity noise-free linear regime where signal is also selectively doubled. Furthermore, we construct $2pl$ independent number of such noise-free pairs on the twisted interferogram to further reduce overall noise-floor by two orders of magnitude enabling detection of weak displacements. We apply this unique approach to isolate a single-event of deformation of solid deeply hidden in noise. Our simple, precise and scalable approach suggest wide application in detection of signal from noise in remote sensing, precision metrology and fundamental measurements of intra-cellular forces.

4.2.2 Theoretical analysis of twisted interferometer

We theoretically analyze our interferometric self-calibration and multi-pixel noise-cancellation.The paraxial beam can be represented by the combination of the Laguerre-Gaussian (LG) modes. Any paraxial beam can be represented by the combination of the Laguerre-Gaussian (LG) modes. A generalized $LG_p^{|l|}$ beam can be described using Eq. (4.1).

$$\begin{aligned} E_{p,l}(r,\phi,z) = \big(E_0+\xi(t)\big)\,\frac{1}{w(z)}\sqrt{\frac{2p!}{\pi(|l|+p)!}}\left(\frac{\sqrt{2}r}{w(z)}\right)^{|l|} \\ \times L_p^{|l|}\left(\frac{2r^2}{w^2(z)}\right)\exp(i(2p+|l|+1)\Psi(z)) \\ \times\exp\left(-\frac{kr^2}{2R_c(z)}-\frac{r^2}{w^2(z)}\right)\exp(il\phi) \end{aligned} \tag{4.1}$$

where k is the wave number, $w(z)=w_0\sqrt{\left(1+\left(z/z_0\right)^2\right)}$ and $R_c(z)=z\left(\left(z_0/z\right)^2+1\right)$ are the size and radius of curvature of the LG beam at z, $z_0=\pi w_0^2/\lambda$, the Gouy phase $\Psi(z)=\tan^{-1}\left(\frac{z}{z_0}\right)$, and $L_p^{|l|}(x)$ is the Laguerre polynomial with l and p as the azimuthal and radial indices of the beam. $\xi(t)$ is the additive noise in the laser intensity fluctuations. The above equation can be written in a simplified form for p=0 as:

$$E_{+l}(r,\phi,z) = \big(E_0 + \xi(t)\big) R_1(r) e^{il\phi} \tag{4.2}$$

where, $R_l(r)$ is the radial dependence term of the electric field. The electric field of the conjugate LG beam (measurement beam) with $-l$ topological charge will include a minus sign in the ϕ dependence term of Eq. (4.2). The electric field of the measurement with additional path difference of Δh is written as

$$E_{-l}(r,\phi,z) = \big(E_0 + \xi(t)\big) R_l(r) e^{i(-l\phi + 2k\Delta h)} \tag{4.3}$$

The superposition of these conjugate LG beams will result in the formation of daisy flower like interference pattern with $2|l|$ number of petals. The net interference intensity at z due to the superposition of the beams carrying $+l$ and $-l$ topological charge will then be given by:

$$I(r) = \left|E_{-l}(r,\phi) + E_{+l}(r,\phi)\right|^2 \tag{4.4}$$

$$I = \underbrace{4E_0^2 \left|R_l(r)\right|^2 \cos^2(l\phi + k\Delta h)}_{Interference\ Intensity} + \underbrace{4|\xi(t)|^2 \left|R_l(r)\right|^2 \cos^2(l\phi + k\Delta h)}_{Noise\ Term} \tag{4.5}$$

From the above expression we notice an angular dependence in the intensity modulation of the daisy flower pattern. Just like in Michelson interferometer, we also observed that the interference intensity for the LG beam propagation follows the $\cos^2\phi$ curve. The first term in the above expression is the noise-free interference term and the second term is the noise term. For the noise free measurements we have selectively chosen the pixel pair such that they are out of phase with respect to each other at all times, i.e. $\Delta\theta = \pi/2$, where $\theta = l\phi$ is the net transverse phase difference of the interference pattern (as shown in Figure 4.1). The interference intensity at detector 1 (I_{D1}) is given by:

$$\begin{aligned} I_{D1}\big|_{\phi=0\to\pi/2} = {} & 4E_0^2 \left|R_l(r)\right|^2 \cos^2(l\phi + k\Delta h) \\ & + 4|\xi(t)|^2 \left|R_l(r)\right|^2 \cos^2(l\phi + k\Delta h) \qquad \in [1,0] \end{aligned} \tag{4.6}$$

The out of phase interference intensity at detector 2 (I_{D2}) can then be written as:

$$\begin{aligned} I_{D2}\big|_{\phi=0\to\pi/2} = {} & 4E_0^2 \left|R_l(r)\right|^2 \cos^2(l\left(\phi + \pi/2\right) + k\Delta h) \\ & + 4\left|R_l(r)\right|^2 \left|\xi(t)\right|^2 \cos^2\Big(l\left(\phi + \pi/2\right) + k\Delta h\Big) \qquad \in [0,1] \end{aligned} \tag{4.7}$$

Subtracting the intensities at both the detectors yields:

$$I_D = I_{D1}|_{\phi=0\to\pi/2} - I_{D2}|_{\phi=0\to\pi/2} \qquad \in [-1,1] \tag{4.8}$$

Note that the range in which the interference intensity now varies has doubled. The intensity in the linear regime, i.e. at $\phi \to \pi/4$, at both directions will be similar in magnitude but in opposite direction. The interference intensity at $\phi = \pi/4$ at both the detectors will be given by:

$$I_{D1}|_{\phi\to\frac{\pi}{4}} = 4E_0^2 \left|R_l(r)\right|^2 \cos^2\left(\frac{l\pi}{4} + k\Delta h\right) + 4|\xi(t)|^2 \left|R_l(r)\right|^2 \cos^2\left(\frac{l\pi}{4} + k\Delta h\right) \tag{4.9}$$

$$I_{D2}|_{\phi\to\frac{\pi}{4}} = 4E_0^2 \left|R_l(r)\right|^2 \cos^2\left(\frac{l3\pi}{4} + k\Delta h\right) + 4|\xi(t)|^2 \left|R_l(r)\right|^2 \cos^2\left(\frac{l3\pi}{4} + k\Delta h\right) \tag{4.10}$$

The subtracted intensity at this point is given by:

$$I_D = I_{D1}|_{\pi/4} - I_{D2}|_{\pi/4} = 0 \tag{4.11}$$

Thus, we have created (or shifted) a noise-free minima in the linear regime of the interferometer. Now, at this point any external signal detected will be noise free and amplified as now the net intensity can be given by:

$$I_D = Interference\ Intensity + \text{ Noise } + I_S$$

$$\begin{aligned} I_D|_{\phi=\pi_4} &= I_{D1}|_{\pi/4} - I_{D2}|_{\pi/4} \\ &= I_{S1} - I_{S2} \\ &= 2I_{S1} \qquad \left(\because I_{S2}|_{\pi/4} = -I_{S1}|_{\pi/4}\right) \end{aligned} \tag{4.12}$$

This has been validated in the simulation and experiment as will be shown later. We will now discuss our compact CiLens twisted interferometer and will demonstrate the noise cancellation with signal amplification in real time.

4.2.3 Experimental set-up

Our compact twisted interferometer is based on the key idea of a cylindrical interference lens (CiLens), as shown in Figure 4.1(a). The CiLens combines the multiple functions of a beam-splitter, reference mirror, light collector, and parity invertor into a single lens in order to produce a stable daisy flower-like interference pattern. The CiLens was fabricated by

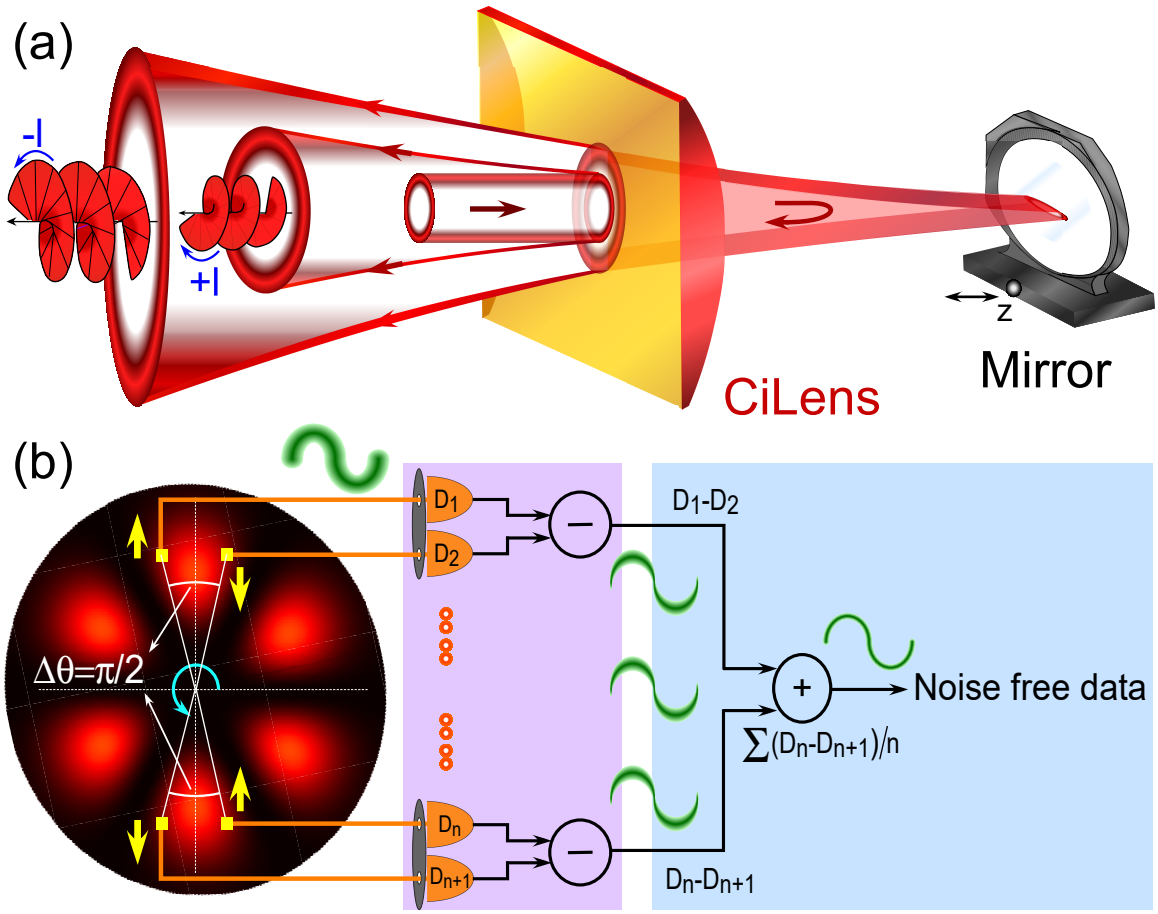

Fig. 4.1 **Schematics of a single cylindrical iLens ultra stable twisted interferometer.** (a) Cylindrical iLens produces the flower-like interference pattern by combining the two beams with opposite topological charges. (b) describes the algorithm to do noise-free measurements by selecting anti-correlated pixel points (yellow squares) on the interferogram.

partially coating (40:60) the flat surface of the cylindrical lens. The incoming twisted light of given topological charge $+l$, generated by a spatial light modulator (SLM), is partially reflected from the flat surface and serves as a reference beam with state $+l$. The partially transmitted twisted beam is retro-reflected from the mirror also its state is changed to $-l$. An overlap of two twisted beams of opposite helicity interfere on the screen leading to a stable daisy flower-like interference pattern as shown in Figure 4.1(b). To observe the good contrast of the interferogram, the test mirror is adjusted near the focus of the CiLens. The number of the petals in the interference pattern, are double of the topological charge $2|l|$. When the test mirror is displaced in the positive (negative) z-direction, the flower pattern rotates clockwise (counter-clockwise) like a mechanical screw-like motion. Previously, such interference pattern has been observed with Michelson interferometer, albeit a multi-component system,

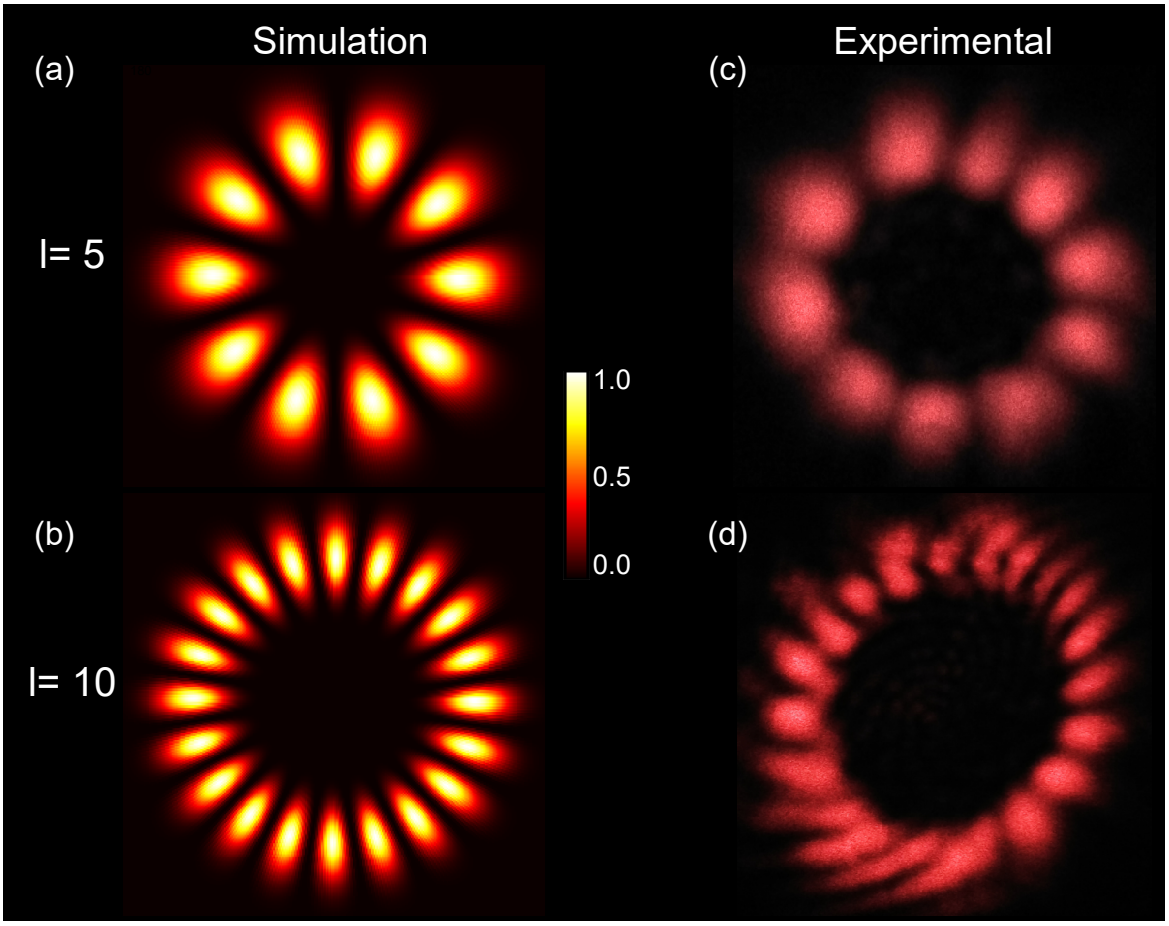

Fig. 4.2 **Snapshots of daisy flower pattern.** (a-b) Snapshots of simulated daisy flower pattern. The color bar shows the normalized intensity value. (c,d) Corresponding experimentally obtained pattern for l=5, 10.

by placing a cylindrical lens in one of the interferometer arm. Unlike the conventional interferometers, our CiLens interferometer is compact and robust in producing stable high contrast fringes.

Besides, we show that a single-pixel based intensity detection using a fast photodiode allows an easy and precise self-calibration of the interferometer. In addition, we show that a two-pixel or multi-pixel based detection exploits the spatial correlation in the phase of the twisted beam to cancel noise in real-time and enable detection of picometer scale signal deeply submerged in noise establishing the key advantages of twisted-interferometer over the Gaussian beam interferometers. Figure 4.1(b) shows schematically the algorithm used to do the noise-free measurements in real-time. A pixel-pair on the interferogram is chosen such that the intensity at the two detectors are out of phase, i.e. ($\Delta\theta = \pi/2$), at any time while taking the measurements. The intensity difference at these two detector positions is

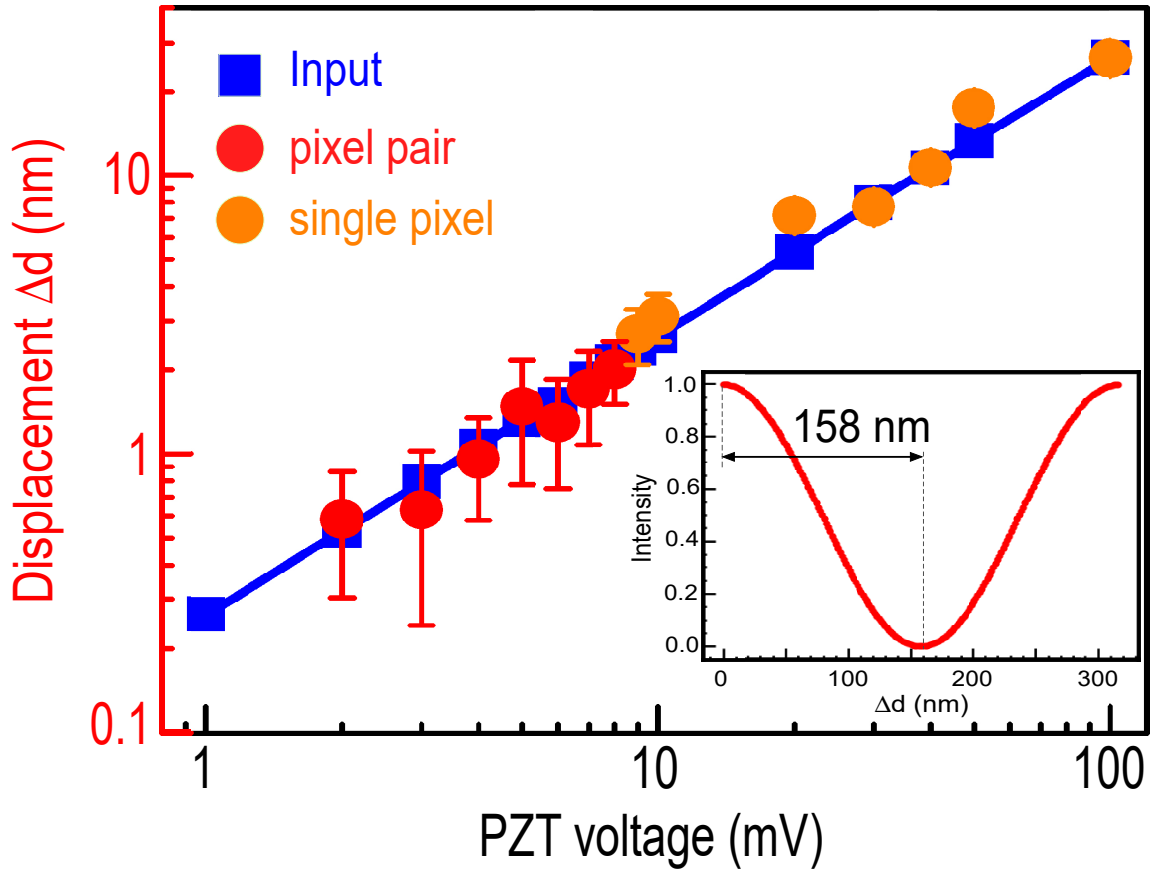

Fig. 4.3 **Calibration curve** showing the measured mirror displacement with a photodiode (red & orange circle) with the known input mirror displacement (blue square). The orange and the red dots correspond to the single pixel displacement and anti-correlated pixel pair displacement on the interferogram. The solid blue line is the linear fit. The experimental noise floor is indicated by the error bars. The lower right inset shows the $\cos\phi^2$ dependence of the interference intensity.

recorded using a photodiode (or webcam) on the oscilloscope to reduce the additive noises, like laser intensity fluctuations, in the interferometer. Furthermore, we can construct $2pl$ independent number of such noise-free pairs on the twisted interferogram to further reduce overall noise-floor by two orders of magnitude enabling detection of weak displacements.

4.2.4 Picometer resolved self-calibration with single-pixel measurement

We validate our compact interferometer in Figure 4.2(a-d) by obtaining a stable daisy-flower like interference pattern. The experimental interference pattern for two different values of l is shown along with the corresponding simulated pattern. In the absence of modulation in the mirror position, the interference pattern remains stable. In order to measure the direction

and magnitude of the displacement of mirror, we detect single-pixel intensity (detector area much smaller than typical petal width) and modulate the mirror by imparting a known value of displacement. To establish the self-calibration of our setup [107] we gave an input displacement $\delta h = h(t) - h(0)$ to the mirror using the nano-positioner and compared it with the corresponding shift in the interference intensity as shown in Figure 4.3. The interference condition, i.e., half fringe collapse corresponds to $\delta h = \lambda/4$, governs the self-calibration of our setup and is independent of time-scale of the interference fringes. As shown in the inset (Figure 4.3), the $I(x_0, y_0)$ follows a cosine square curve vs the mirror displacement. The measured displacement of the the Mirror with laser intensity, using the interference condition, agrees with the given displacement from the measured range covering from 100 nm to tens of pm. Thus I allows to measure unknown displacement in real time, with self-calibration.

Single-Pixel detection is not only simple and fast, but also precise compared to rotation angle based measurement approaches used previously because this requires detection of edges of interference pattern. The self-calibration is robust in the sense that it is independent of the position of the pixel on the petal.

4.2.5 Results

4.2.5.1 Set-up stabilization against various noises

We have exploited the symmetry in the daisy flower pattern to stabilize our setup against various fundamental noises. It is well known that the interferometer is most sensitive to path length change in the linear regime of the $\cos^2\phi$ curve, so, there is a need to reduce the noise floor in the linear regime. Here, we used the symmetrical flower pattern to track the intensity change at two different points simultaneously. The points are chosen such that they are out of phase, i.e. if one detector is at the maxima (minima) of the fringe then the other detector will be at the minima (maxima). For example in Figure 4.4(a) we show the simulated effect of intensity fluctuation noise in the laser and we notice that the effect of noise is more prominent at the maxima and in the linear regime of the intensity curve. The noise affecting minima the least is the reason why interferometers are set there. This would also imply that now the interferometer is less sensitive towards capturing the change in the optical path length of the beam. To solve this problem, we have exploited the anti-correlated points on the daisy flower interferogram to self-cancel the additive noises. Such two-pixel detection allows significant reduction of noise in the most sensitive linear regime of our interferometer as derived in the equations 4.9-4.11 above. This has been validated in our numerical simulation as well as in experiment of interference intensity in the presence of intensity noise, as shown in Figure 4.4. Due to the $\cos^2\phi$ dependence, the noise amplitude modulates. Although, noise affecting

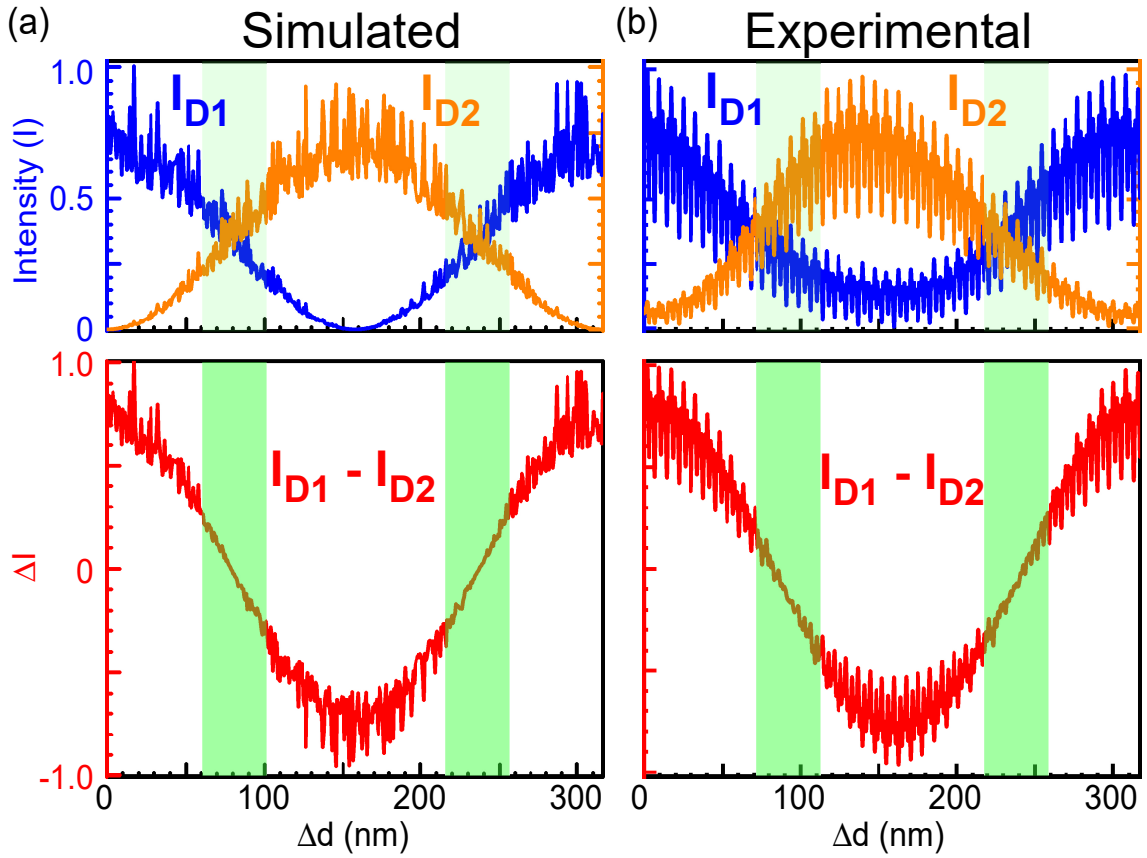

Fig. 4.4 **Differential noise cancellation**, (a,b) The upper graphs shows the simulated random noise and the experimental noise in the fringe pattern at two anti-correlated points. The lower graphs shows the enhancement of the signal to noise ratio in the linear regime (in green color band) by differential noise cancellation technique.

minima is the least, our interferometer is least sensitive towards capturing the displacement of the mirror near the minimum. For all other positions, the noise is clearly visible in both pixels. However, if we chose the location of pixels such that the intensity change is anti-correlated, i.e., to be out of phase ($\Delta\theta = \pi/2$), due to intrinsic anti-correlation in the intensity change, produced by the rotation of the petal, the noise is cancelled significantly as shown in Figure 4.4(a,b).

We have demonstrated real-time noise self-cancellation by detection of a weak signal, amid the large intensity noise produced by SLM. We show that a tiny step of few nm, which is otherwise undetectable (see Figure 4.5) becomes visible in our experiment by two-pixel detection. Using the approach derived in the above equations we have been able to detect weak signal, i.e., the displacement of the mirror, reliably with a precision of sub-50 *pm* (4.5). The above scheme is independent of the l, provided the correlated detection can be setup.

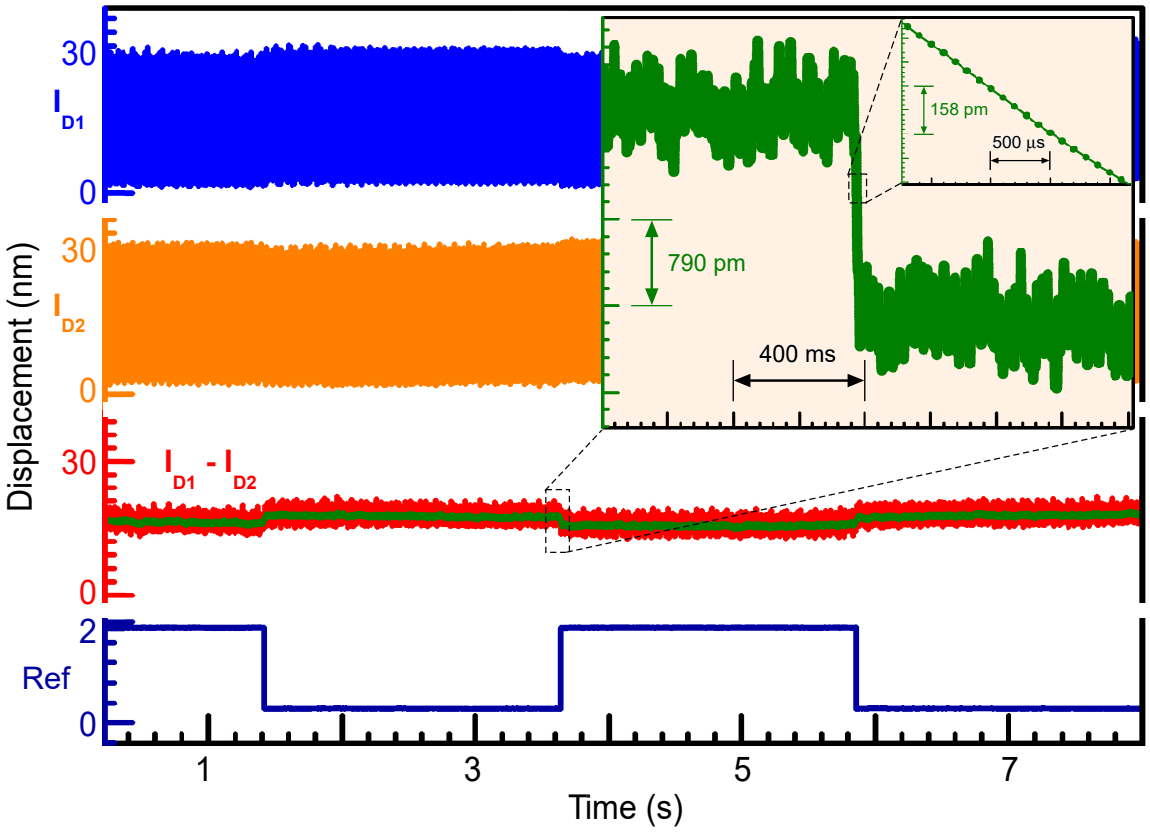

Fig. 4.5 **Real-time sub-50 pm resolved displacement measurement.**. The mirror was given a known displacement of 2 nm, and the corresponding change in the interference intensity was recorded at two anti-correlated points.

For larger l-value, the petal width reduces. In this situation, it is possible to optically expand the petal to allow double-pixel detection.

When the sample mirror is displaced, rotation of the petals induce a small change occurs in the intensities of both the detectors (red and orange curve in Figure 4.5). For tiny displacements, the corresponding small intensity change is masked by the laser intensity noise and is hardly visible. Here, our interferometer (or detection scheme) provides the advantage of real time differential noise cancellation. As the detected intensities are in opposite phases, we do the real time subtraction where the laser noises in same phases disappears and the required signal gets enhanced by a factor of two. Fig. 4.5 shows the zoom of step response where the laser noise has been cancelled out and required response becomes double. The generation of OAM with 288^{th} order directly from the laser with transmission-stability has been recently demonstrated, which suggests that a significant $(1/\sqrt{N})$ reduction in the noise-floor of an interferometer can be achieved [108].

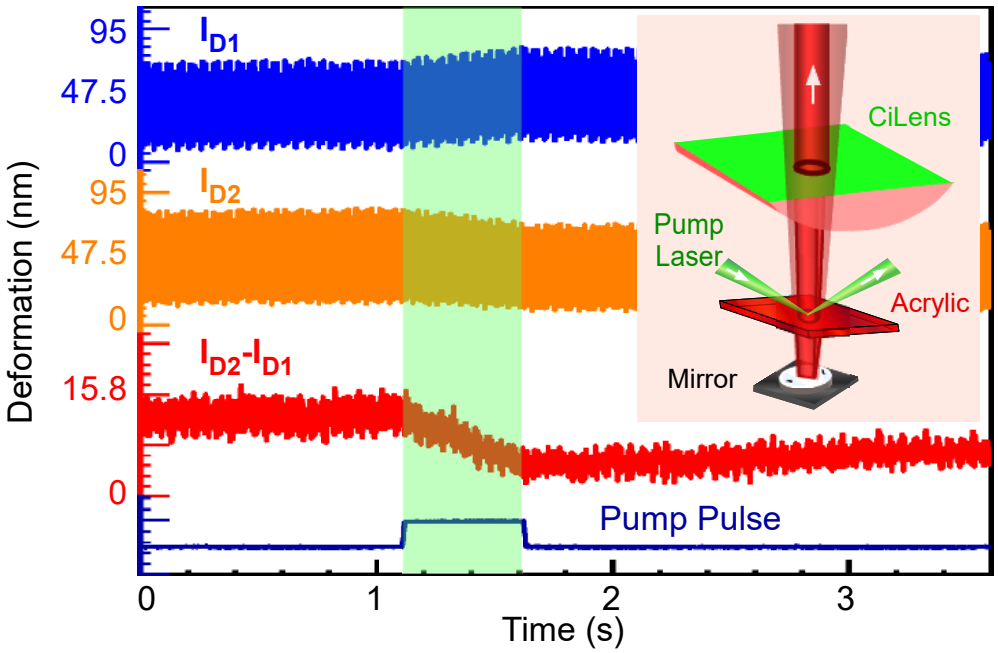

Fig. 4.6 **Photo-thermal dynamics of a semi-transparent solid material**. The blue and the orange curve shows the interference intensity at two detector positions. The red curve shows the noise cancelled deformation in real-time. The violet curve is the pump laser signal. The inset shows the schematic setup to measure the deformation on the red acrylic sheet kept in the interferometric cavity. A low-power CW green laser was used to deform the sample surface.

4.2.5.2 Isolating photo-dynamics submerged in noise

Finally, we demonstrate that the iLens cavity allows detection of photo-thermal dynamics of a semi-transparent solid material, such as a sheet of red-acrylic, below the experimental noise floor. High-contrast fringes were obtained when a red-acrylic (poly-methyl-methacrylate) was inserted in the cavity (Figure 4.6). Upon irradiation of acrylic with a low-power green laser pulse ($500\ ms, 10\ mW, 2\omega_0 = 400\ \mu m$), the deformation is hardly visible in I_{D1} or I_{D2}. We clearly resolved the reversible photo-thermal bump, which was few nm, in this case. The direction of rotation of the pattern during the pump exposure tells about the formation of a bump on the sample due to heating. The sensitivity and simplicity of our scheme allows dynamic detection of small deformation below the noise level suggesting its wide application potential for precision measurement on liquid, gas and plasma.

4.2.6 Discussion

CiLens has a broad applicability for noise-free measurements on diverse solid surfaces. CiLens allows obtaining twisted-fringes directly from highly absorbing to fully transparent surfaces by appropriately tuning its beam-splitting coating. The CiLens and the solid surface of interest makes an ultra-compact tool to probe dynamics of solids, for example across a phase-transition, subjected to thermal, magnetic and acoustic perturbations. Besides, the setup is versatile to probe liquid, gas or plasma state of the matter as well.

In contrast to conventional Gaussian beam interferometers, the noise-cancellation can be scaled up using higher order twisted light. For example, for a twisted light of charge l and radial quantum number p, the total petals in the interference pattern are $2lp$, which allows making a $2lp$ noise-cancelled pairs. For $l = 300$ and $p = 30$, which one can generate experimentally, the residual random noise floor (acoustic, air-drag, thermal noise etc) can be further reduced by ($\sqrt{2lp}$ 100) fold. The ultimate noise reduction may be decided by the pixel size of the detector chip (pixel density) and the size of the OAM beam which increases with l. Our unique scheme allows exploiting full potential of spatial phase structure of twisted light for noise-elimination.

It is possible to further miniaturize the entire setup on a chip. For example, one can integrate a phase-plate and CiLens into one element along with a micro-laser producing Gaussian mode for space-constrained applications. Besides, our CiLens can be directly integrated with a laser cavity emitting twisted-light, such as $l = 288$ with stable propagation, to make a compact twisted noise-compensated interferometer.

Furthermore, by employing balanced low-noise detector pairs, frequency stable-laser, and cooling our ultracompact interferometer to cryogenic temperatures the noise can be further improved, possibly reaching the femtometer regime in real-time.

In conclusion, we demonstrated a comprehensive approach for noise self-cancellation and signal amplifying single-lens twisted interferometer. Besides, being ultra-stable and compact, we show a single-pixel detection of daisy flower-like interference pattern to self-calibrate the twisted interferometer with picometer resolution. The multiple degrees of freedom, offered here in the form of identical fringe petal, allows us to simultaneous detect correlated intensity change leading to real-time averaging based decrease in noise-floor. Remarkably, we exploited the anti-correlation in the transverse phase front to achieve real-time cancellation of intensity noise, allowing detection of signals buried in the large noise background for wide variety of application.

We envision that our simultaneous multi-dimensional measurement would be useful for many applications including precision metrology, remote sensing and fundamental measure-

ments. It will be interesting to operate the interferometer in quantum noise regime with few photons.

4.3 Large area processing with ultrafast light sheets

4.3.1 Introduction

The nanopatterning of solid surfaces with ultrashort laser pulses is a growing area with many applications in modulating optical, material and surface properties. Since the first observation of laser-induced periodic surface structures (LIPSS), also termed as ripples on semiconductors by Birnbaum, LIPSS have been produced on most metallic and dielectric surfaces [109, 110]. The generation of LIPSS upon irradiation of laser pulses below the material's damage threshold is a universal phenomenon [111]. Although their occurrence, structural size and formation mechanism depend on the material and irradiation parameters.

The LIPSS have attracted remarkable interests over the past few decades due to their large variety of applications such as in generation of super-hydrophobic surfaces [112], cell culture substrates [113, 114] and in making of photonic devices [115–117]. Several attempts have been made to produce variety of patterns by shaping the polarization of fs-pulse (linear, circular or radial) or using beams carrying orbital angular momentum and multicolor pulses [118–120]. This has allowed researchers to generate surfaces that mimic structures found on insects, shark skin etc in order to imitate their remarkable optical, mechanical or self-cleaning properties [121–125].

The standard technique to produce LIPSS is by 2D raster scanning of a focussed fs pulse on a solid surface. The LIPSS are formed within the microspot of the laser beam. The point-by-point illumination to cover LIPSS on a large surface area (say, 1 cm^2) is a time-consuming process [121, 126–128]. Furthermore, with this approach it is difficult to produce homogeneous nano-patterns over the entire area because the laser parameters (pulse energy, pointing stability, fluence) may fluctuate during the slow patterning. Cylindrical lens with long focal length have also been used to produce nano-structures on extended area of steel and TiO_2 [129, 130]. However, the effect of shorter focal length of cylindrical lens in combination with short 25 fs pulse has not been studied yet. One may wonder if these improvements lead to high-fidelity, large area tunable nano-structures.

Here, we demonstrate an application of tightly focussed fs-light sheet to produce high-fidelity LIPSS over a macroscopic surface area by a single one-dimensional scan. A short focal length cylindrical lens is used to produce the line focus on the silicon surface and by varying the scanning speed of the sample, we reliably produce different LIPSS. The

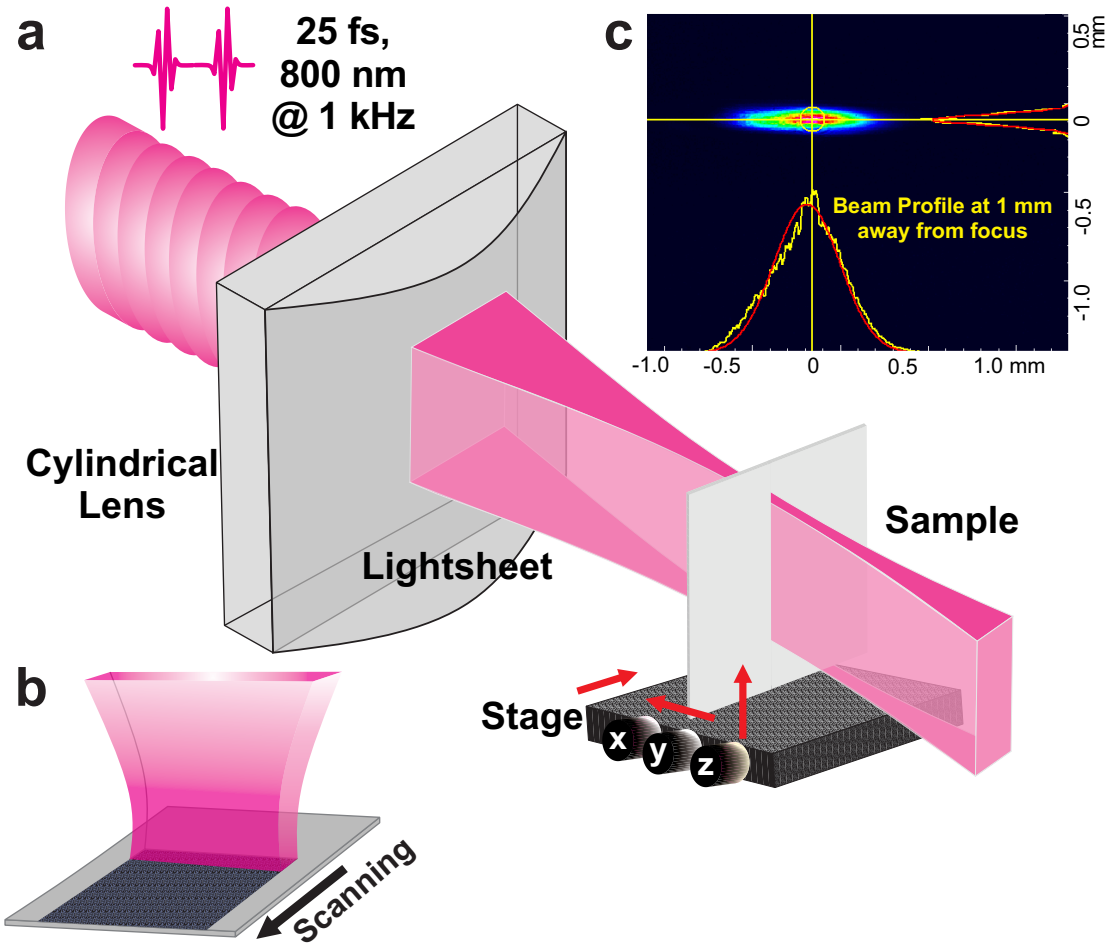

Fig. 4.7 **Schematics of the experimental set-up.** (a) The fs-pulses (25 fs, 2 mJ, 1 kHz, $\lambda = 800$ nm) are focused through an achromatic cylindrical lens made of fused silica (f = 8 mm). (b) Sample scanning in the light-sheet. (c) A typical beam profile at 1 mm away from the focus of the cylindrical lens. The estimated spot size at the focus is about 7 μm.

fundamental spatial frequency of LIPSS on a crystalline Si is about 660 *nm*. It's second order at 330 *nm* became dominant as the scan speed is increased. We also observed visible structural colors on the silicon surface under white light illumination.

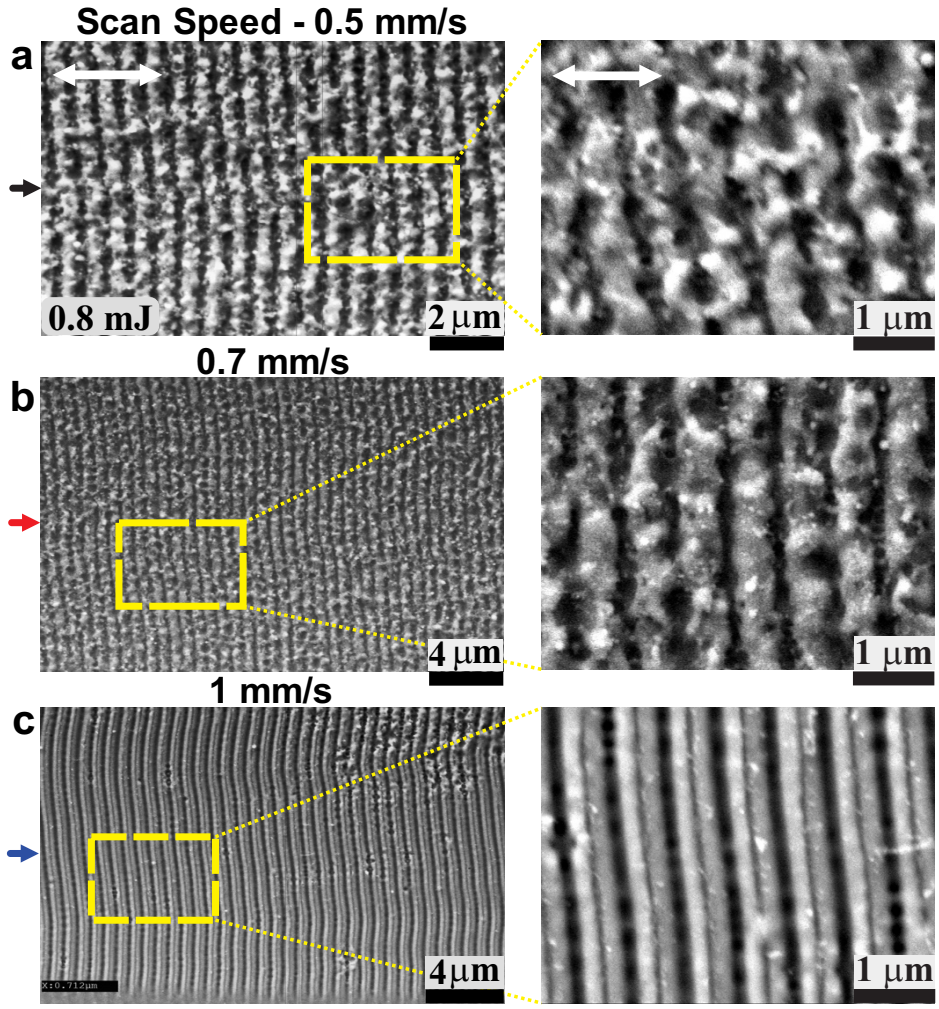

Fig. 4.8 **SEM images of laser induced periodic nano-structures on the crystalline silicon surface at different scanning speeds.** (a) 0.5 mm/s, (b) 0.7 mm/s, and (c) 1.0 mm/s. The energy per pulse is 0.8 *mJ* for these cases. White arrow indicates the direction of linear polarization of the incident pulse. The right side images are zooms of the dotted rectangles. The horizontal arrows (black, red and blue) on the left indicate the direction of line profile.

4.3.2 Experimental set-up

The schematic of our experimental setup is shown in Figure 4.7(a). We used femtosecond laser pulses of 25 fs pulse duration arriving with 1 kHz rep rate at central wavelength of 800 *nm*. The femtosecond light sheet was produced from the input Gaussian beam

($2\omega_0 \simeq 8\ mm$) by focusing it in one dimension using a cylindrical lens. The cross-section of the cylindrical lens was $8\ mm \times 8\ mm$ with central thickness of $3\ mm$. The major axis of the elliptical focus was about $8\ mm$ and the minor focus was about $7\ \mu m$. A typical image of the line focus (characterized using a He-Ne laser) is shown in Figure 4.7(c). The light sheet was linearly polarized along the minor-axis.

The sample taken was a silicon wafer (Si 100) available from Sigma Aldrich. The sample (typically $10 \times 30\ mm^2$) was mounted on a computer controlled high-speed translational stage (Thorlabs) and was adjusted in the focus of the fs-light sheet. The sample was scanned in the focal plane with a controlled speed varying from $0.5\ mm/s$ to $1\ mm/s$. The laser power (energy per pulse) was controlled by a ND filter. The pulse duration in the line focus was not measured. After processing, the silicon sample was cleaned in an ultrasonic bath for 30 minutes. The sample surface, without any coating, was then imaged using electron microscope and analyzed.

4.3.3 Results

4.3.3.1 Characterization of laser induced periodic nano-structures (LIPSS) on silicon surface

The electron micrographs of the silicon surface processed at constant energy of $0.8\ mJ$ per pulse and at three different scanning speeds is shown in Figure 4.8(a)-(c). The interaction of fs light-sheet decorated the Si surface with periodic nano-structures as shown in the imaging area of about $50\ \mu m \times 50\ \mu m$. The lines in the patterns were aligned perpendicular to the direction of linear polarization (shown by white arrow in Figure 4.8(a)) [131]. As we increased the scan speed from $0.5\ mm/s$ to $1\ mm/s$ (Figure 4.8(a)-(c)) the LIPSS became more and more homogeneous [132]. Figure 4.9 shows the line profile of the image taken along the direction marked by coloured arrows with average of 10 pixels in Figure 4.8(a)-(c) indicating multiple spatial periods as the scan speed is increased.

Figure 4.10(a)-(c) shows 2D Fourier transform of the images shown in Figure 4.8(a)-(c), respectively. The Fourier transforms show well defined peaks that correspond to an average spatial period, $\Lambda = 660\ nm$. This is close to $\Lambda = 0.75\lambda$ which has been referred to as Low spatial frequency LIPSS [133, 134]. The line profile of the Fourier transforms (right column, Figure4.10) indicates that the fidelity, F, of the structure, defined as the inverse of full width at half maximum, ΔK, of the peaks (marked 1, 2), i.e., $F \propto 1/\Delta K$. We observed that F increases with increase in the scanning speed. In addition, the 2D-FFT images illustrated that there is no change in the spatial frequencies of LIPSS rather the intensity of second-order peak increased. The deviation angle of the oriented nano-structures with respect to the normal of

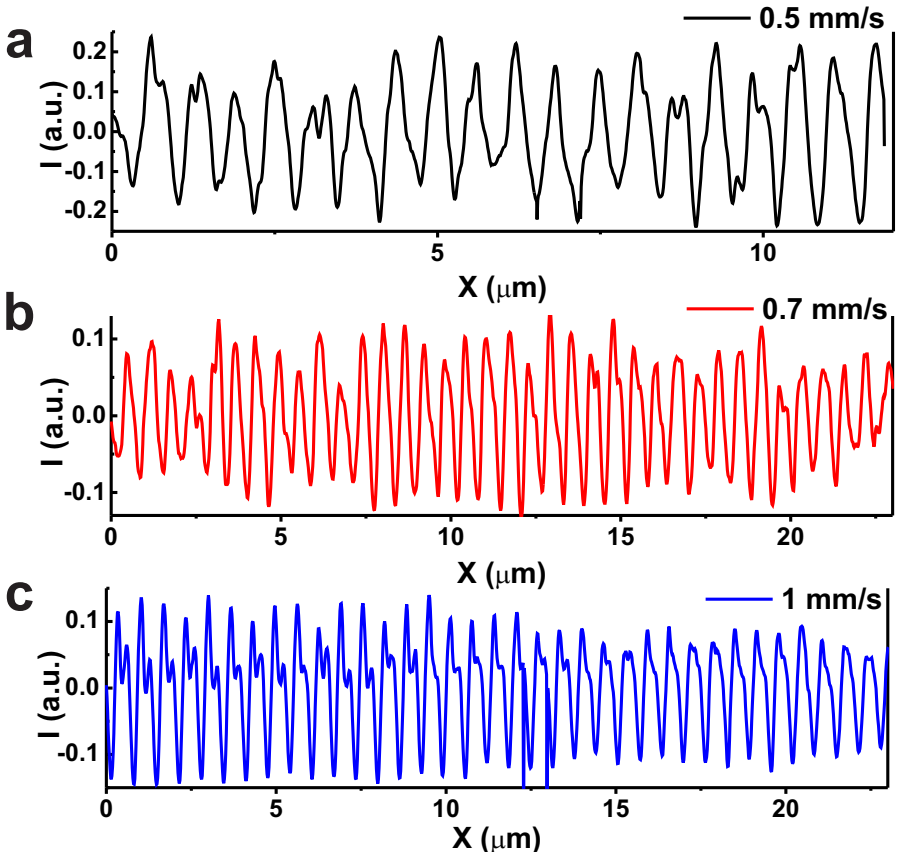

Fig. 4.9 **Line profile of SEM images of Figure 4.8 along the direction of the corresponding color arrow.** (a)-(c) correspond to the SEM micrographs at different scanning speeds (a) 0.5 mm/s, (b) 0.7 mm/s, and (c) 1.0 mm/s.

the incident S-polarization decreased from 10° to 6°, i.e., the perpendicularity of LIPSS was higher [135].

A wide variety of periodic patterns has been reported in the literature, in particular, low-frequency and high-frequency LIPSS [133]. In our case of normally incident fs-light sheet, the observed sub-λ spatial periods were in the range $(\lambda/2 \leq \Lambda \leq \lambda)$.

Previous attempts to explain the large wavelength sized ripples were based on the inhomogeneous energy deposition due to interference between incident and scatterd wave [136, 137]. However, the scattering model could not explain the observed features of the sub-wavelength ripples on dielectric and metallic surfaces. As reported in the literature, we attribute that these nano-structures are generated by the excitation of Surface Plasmon Polaritons (SPP) [138, 139]. A normally incident laser beam excites the SPP on a metal-dielectric interface when specific conditions for the dielectric permittivity of laser-produced plasma and phase matching between the plasmon surface wave and the incident photons is fulfilled, as detailed

in [138–141]. In addition, these low-spatial frequency LIPSS run perpendicular to the laser polarization. These observations suggest that the large area LIPSS are due to non-linear interactions of the light sheet with the surface plasmons [136]. However, to get a deeper insight into the exact mechanism a detailed theoretical model should be performed in future.

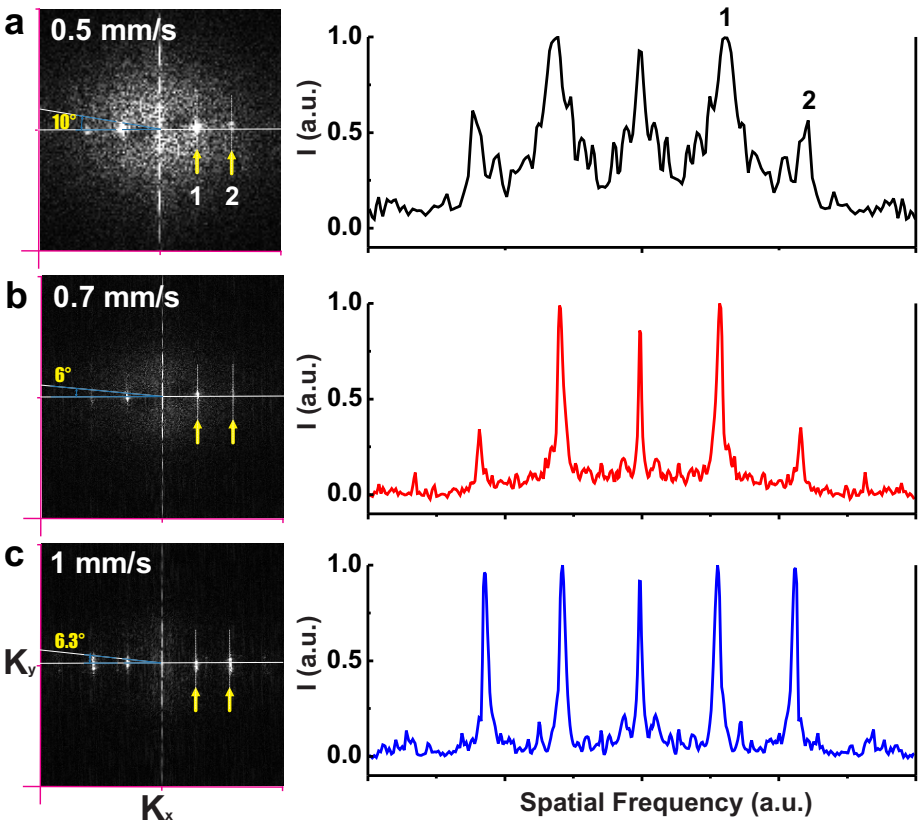

Fig. 4.10 **FFT of SEM micrographs and the corresponding intensity profile along the x-axis.** (a) 0.5 mm/s, (b) 0.7 mm/s, and (c) 1 mm/s. The cut profile of the images is shown on the right.

4.3.3.2 Femto-second processing of large area surface

In Figure 4.11(a)-(d), we demonstrate a potential application of our large area LIPSS in structurally coloring the silicon surface [142]. Upon white light irradiation the original silicon sample appeared black (Figure 4.11(a)). However, we observed rainbow-like colors due to diffraction of the incident white light by LIPSS (Figure 4.11(b)-(d)).

We show two examples of large area processing in Figure 4.12. We processed 95 mm diameter magnetic disk platter (taken out from a computer hard disk) at scanning speed of 1 mm/s at about 1.5 W average power. One can see that the processed area exhibits

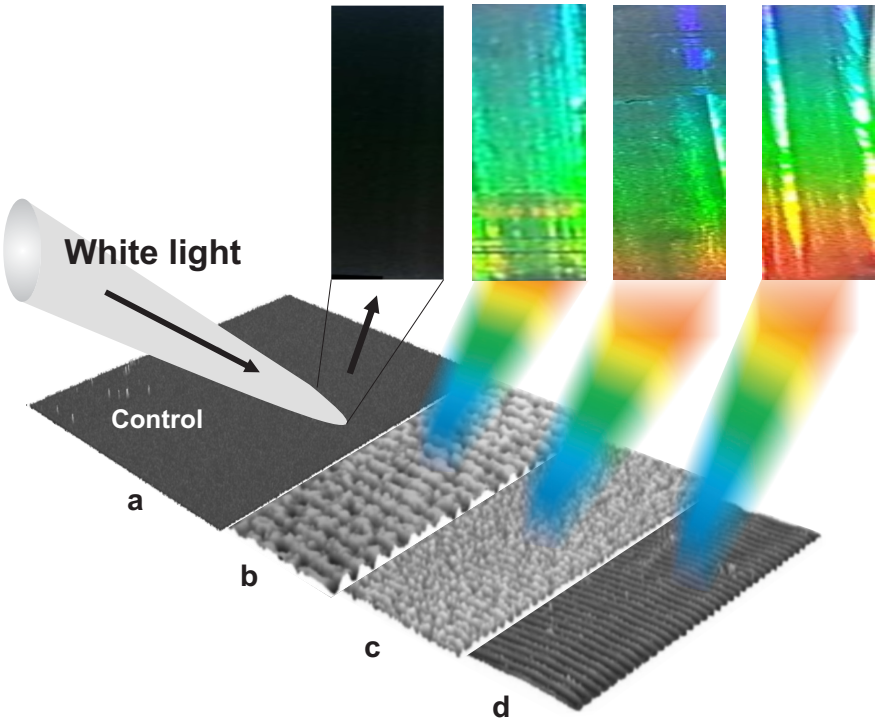

Fig. 4.11 **Diffraction of white light on nano-structured crystalline silicon surface.** (a) Control (no laser), (b) 0.5 mm/s, (c) 0.7 mm/s, and (d) 1.0 mm/s.

visible colors due to diffraction under collimated sun light. Using the grating equation, $\Lambda(sin\alpha \pm sin\beta) = m\lambda$, we observe that for normal incidence, $\alpha = 0^\circ$ and for our spatial period $\Lambda = 0.66\ \mu m$, the visible colors appear in a range of $\beta = 37^\circ - 65^\circ$ in the first order. In another example we chose to process surface of a “butterfly" shaped Nickel-plated Neodymium magnet from a hard disk drive bracket. The three different images of the processed surface taken at different angles of observation shows the vivid colors. The total processing time was about 60 and 10 minutes for the disk and magnet, respectively. These processing speeds are comparable with the recent approaches using laser pulses having a longer pulse duration [143].

One of the key advantages of using short fs light-sheet is in generating uniform nano-patterns over a large area. In addition, 1D line scan is much faster compared to the traditional point by point scanning. For example, with a beam size of 10 mm patterning a 1 cm^2 area at 1 mm/s will take only 10 seconds. The reduction in the processing time makes it easier to keep the laser parameters constant which further helps in getting better uniformity.

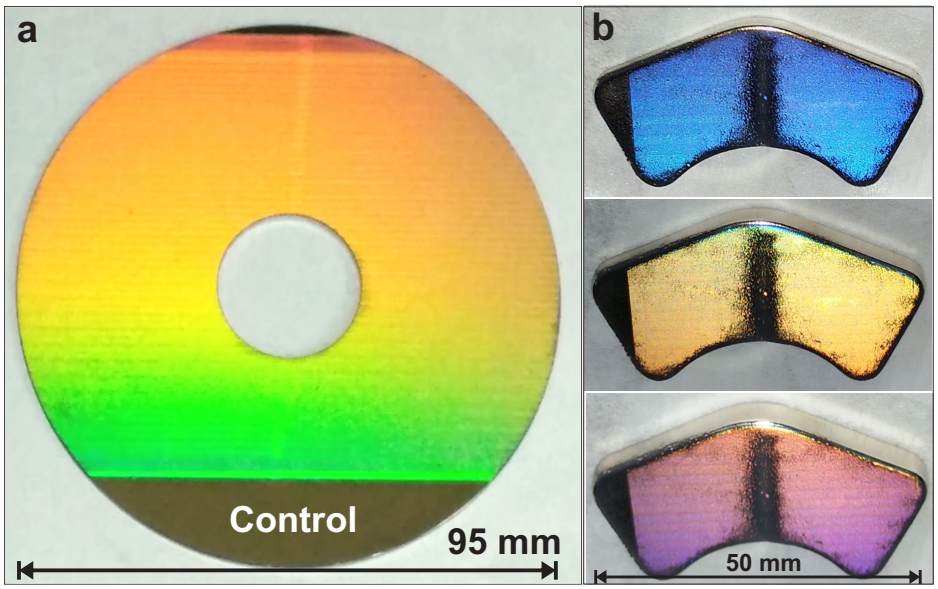

Fig. 4.12 **Examples of large area processing** (a) A magnetic platter of the computer hard disk (b) Nickel-plated Nd magnetic surface. The samples were scanned at $1.0 mm/s$ for 1.5 W average power. Different colors appear due to diffraction of the visible light by LIPSS. The dark band at the centre of the magnetic surface is due to the deposition of the magnetic dust during processing.

We would like to mention couple of remarks on future improvements of our technique. We believe that the homogeneity of the nano-structures could be further increased by employing a light sheet with flat top intensity profile. Our approach is scalable in the sense that one can further expand the beam diameter in order to produce an elongated light sheet to further increase the processing speed.

4.4 Conclusion

We have shown a compact iLens interferometer with twisted light that produces a daisy-flower interference pattern and with single-pixel measurement it yields a self-calibrated picometer displacement. In addition to being compact, the twisted light iLens interferometer enables an interesting possibility to cancel various non-fundamental noises present in an interferometer by multipoint detection. In addition, higher order twisted light enables a real-time averaging of signals that suppresses noise, potentially leading to measurement of weak signals. We also suggest a possible experimental setup to validate our theoretical analysis.

In the second part of the chapter, we demonstrate an application of cylindrical lens to rapidly generate large area, homogeneous patterns on silicon surface. The shape of the nano-structures was controlled by varying the scan speed of the sample. Analysis of SEM images

indicated an emergence of second order spatial periodicity for faster scan speeds. The large area homogeneous patterning may find many applications in designing functional interfaces, optical devices and in tissue regeneration. We expect that tailoring polarization, orbital angular momentum and spectrum of the light-sheet may lead to diverse nano-patterning of solid surfaces. It will be worth attempting to also study the role of light sheets consisting of few-cycle (sub-10 fs) pulses.

Chapter 5

General Conclusions and Perspectives

In this thesis, we have established and demonstrated a novel single-lens universal interferometer capable of probing everyday materials including paper, wood, plastic, rubber, skin, hair, etc., with picometer precision. The key idea was to integrate three different functions of the beam splitter, reference mirror, and collection optics into single iLens which when combined with any arbitrary surface produced high-contrast fringes. We demonstrated the iLens interferometer with 25 different materials and established a framework to make self-calibrating picometer resolved measurement by detecting the interference intensity through an iris. The interferometer was compact and enabled a real-time self-referencing precision of ~ 20 *pm* under ambient conditions without averaging. We also demonstrated that the interferometer can be 3d-printed and can be made as a stand-alone device for precision measurement in remote conditions.

The invention of iLens interferometer opened a new paradigm of universal interferometry with everyday materials enabling fabrication of frugal optical devices with unmatched precision. We have demonstrated three different kinds of optical devices, namely a paper-based pico-balance, a cloth-based ultra-sensitive and broadband acoustic sensor, and a nano-Newton resolved force sensor using bio-fibers. These frugal devices were compared with their high-tech counterparts and were shown to match or outperform in terms of sensitivity and speed.

Besides, the iLens interferometer enabled fundamental non-invasive measurement on the dynamics of candle-flame plasma with picometer precision. By placing the flame inside the iLens cavity, we scanned various regions of the flame and measured their optical properties such as optical thickness, refractive index and flickering dynamics. We observed that when the candle flame is locally subjected to a ns-green laser, a dark-band is created probably due to flame quenching. We have used iLens to probe the single-shot dynamics of the dark-band providing new insight into this intriguing phenomena. The iLens interferometer was also

adapted for probing fluids, therefore, making our iLens as a preferred choice for probing solids, liquids, or gases with ultrahigh precision in real-time.

In the fourth chapter, we have designed and analyzed a twisted iLens interferometer based on cylindrical lens. The interferometer produces high-contrast daisy-flower pattern fringes which rotate clock-wise or counter-clockwise when the sample surface is moved forward or backward. The twisted iLens interferometer is not only compact and yields a picometer resolution but exploits the phase-structure of twisted light for noise-cancellation and real-time averaging rendering detection of weak signals in the noise-background. We have presented a detailed analysis of various noises and also suggested an experimental scheme to realize our noise-compensating compact twisted light interferometer. In another line of work, we have exploited the cylindrical lens to generate a femtosecond light sheet and demonstrated that it produced high-fidelity large area surface nanostructures for various sensing and measurement applications.

It is worth comparing our interferometer with the well established Michelson [1], Mirau [5] or Fizeau interferometers [29] which essentially require precise stabilization and alignment of its multiple components like beam-splitter, reference mirror and light collector. No interferometer has been shown to work directly with rough surfaces and achieve pm precision probably due to their multiple components. Although the Mirau interferometer is compact [5], its reference mirror not only clips the incident beam but also require a fixed working distance. In contrast, our interferometer design offers fully clear view, flexible working distance within several times Z_R. A detailed comparison of iLens interferometer with the state-of-the art interferometers has been discussed in Appendix 1. Furthermore, we verified its robustness by purposefully tilting the iLens ($\pm 10^{\circ}$) and yet retaining the fringes, which could be used for further miniaturization. Importantly, the universal applicability of our interferometer on any scrap material, ultra-affordability and easy operation with self-calibrating pico-level precision makes it attractive for wide variety of applications.

The sensitivity and speed of our current measurement can be further improved. The precision of few hundred picometers of the current apparatus is only limited by the set-up components. If frequency stabilized lasers and electronic signal processing is also used, one can obtain thermal-noise limited precision similar to the sophisticated interferometers [7, 8]. In addition, using high-speed avalanche detectors one should achieve sub-*ns* time-resolution. In applications demanding compactness, one can design a micro-iLens with micro-lasers and detectors on 3d printed substrate.

We envision a broad variety of new applications of our technique. One can design variety of frugal optical devices using iLens, the iLens can be used as an ultra-sensitive probe to not only measure the properties of light but can also unravel nature of mechanical effects in

light-matter interaction. We envision application of iLens in probing properties of complex fluids, pristine bio-materials, and flame plasma with unprecedented precision.

Appendix A

Comparison of iLens interferometer with the existing interferometers

A.1 Design comparison of iLens interferometer

The compactness in the design of the iLens interferometer can be compared with the existing well known interferometers such as Mirau interferometer, Fizeau-type interferometer, Fizeau-type equal path interferometer (EPI). These commercial interferometers require a special optical element called Transmission sphere to test the various curved and rough surfaces. Here, we also show a detailed comparison of our iLens with the transmission shpere and describe the advantages of using iLens interferometers over its commercial counterparts.

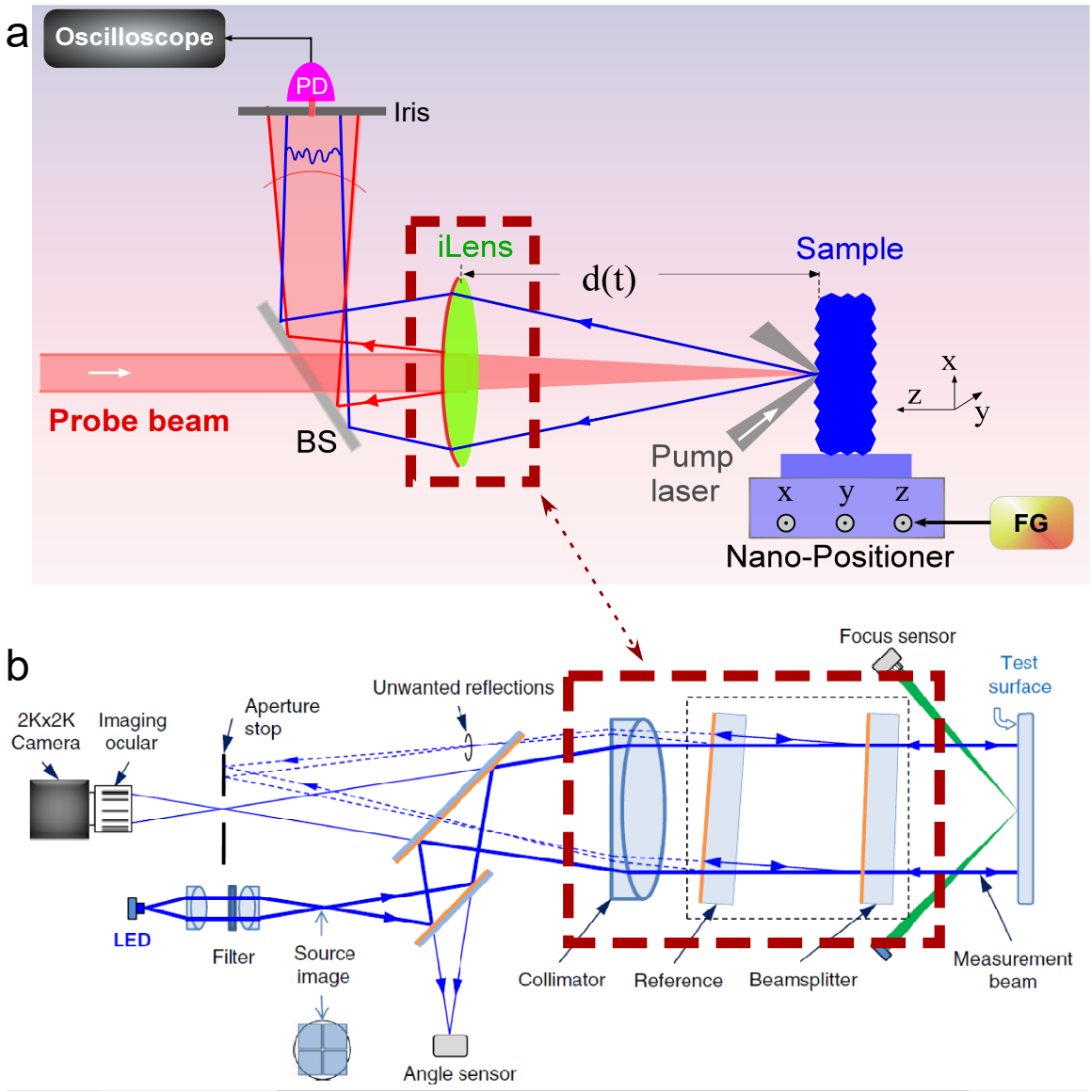

Fig. A.1 **Design comparison of iLens interferometer setup with Fizeau-type interferometer setup. a,** iLens interferometer setup, **b,** Fizeau-interferometer setup. Dotted red box encloses Collimator, Reference and the Beamsplitter which is functionally equivalent to single iLens. In Fizeau setup Reference and Beamsplitter must be tilted, and sensed by Angle sensor, to remove unwanted reflections by Aperture stop. Whereas, in iLens interferometry no unwanted reflection is produced, besides, alignment and stabilization is simplified. Nano-positioner is only used for initial validation of pm resolution and is not necessary. iLens can work on any in situ surface of common materials.

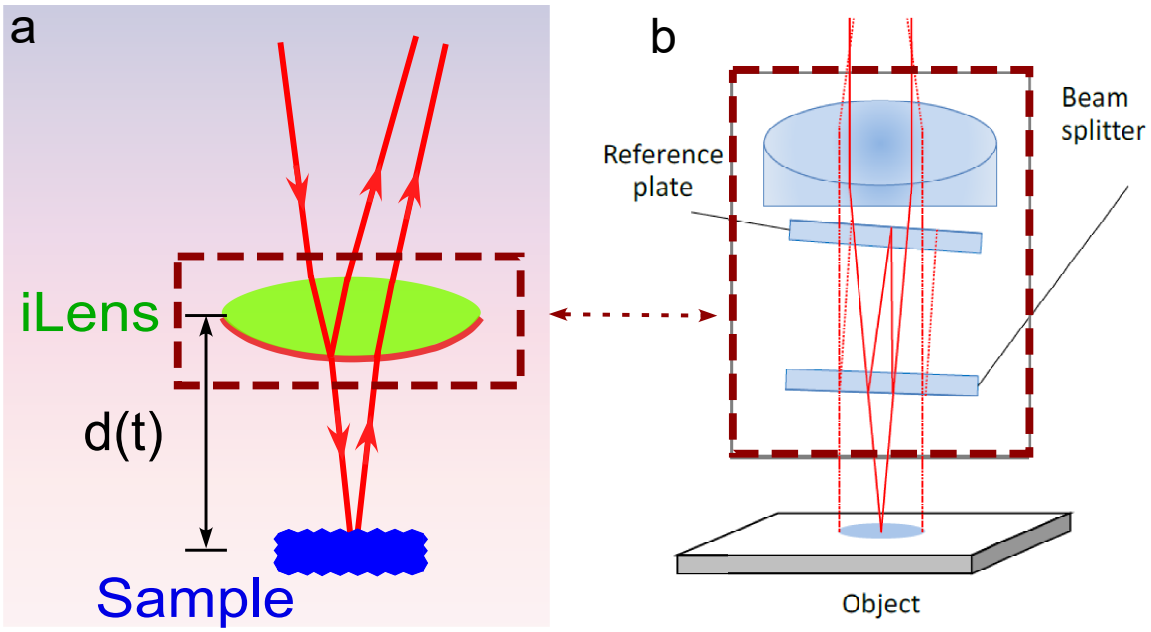

Fig. A.2 **Comparison of optical assembly of iLens with Fizeau-type equal path interferometer (EPI). a,** iLens interferometer **b,** Optical assembly of EPI (Ref. 1). Comparing the two red boxes, the function of collimator, reference plate, and beam splitter in EPI has been combined in one single iLens. The compact geometry makes iLens interferometer stable, robust, and easy to align and enables direct interferometry on any sample.

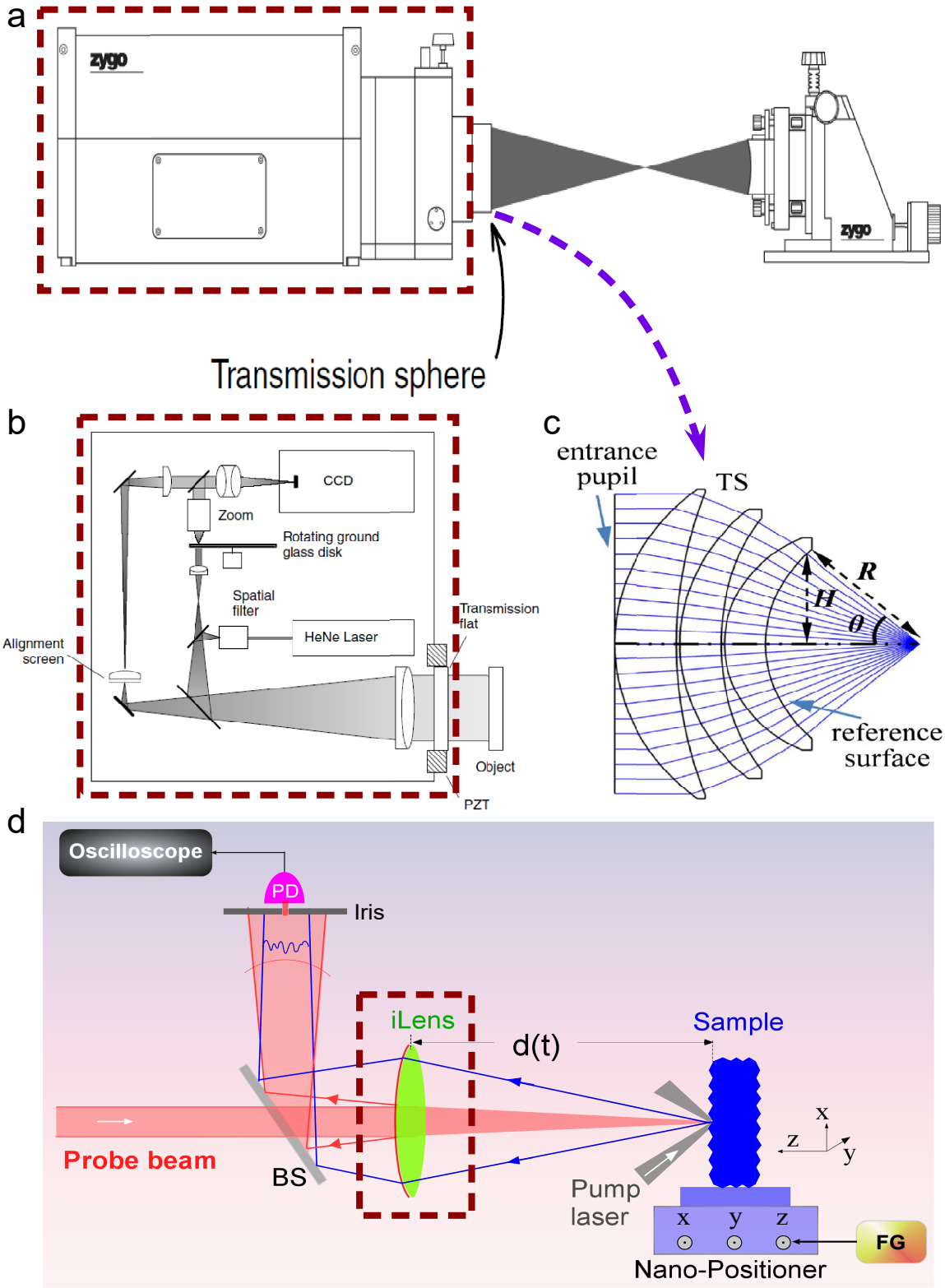

Fig. A.3 **Comparison of our iLens with Transmission sphere.** (a) Commercial laser Fizeau interferometer for testing the deviation from spherical of a concave object (courtesy of Zygo corporation) . (b) Geometry of commercial laser Fizeau interferometer. Inside optical elements of the red box in a. (c) Optics required to make Transmission sphere . (d) iLens interferometer.

Equal Path Interferometer	**iLens Interferometer**
1. Require 3 elements (Focusing lens, Reference element, and Beam splitter) to probe the sample surface.	Only one iLens is required to probe the sample surface.
2. Reference element and the BS need to be at a perfect angle to obscure the unwanted reflections.	No such particular requirement.
3. Used to evaluate the form and texture of flat surfaces only.	All flats, curved or rough surfaces can be probed.
4. Tedious alignment and requires to stabilize more number of components.	Only one iLens needs to be aligned and stabilize.
5. Not suitable for probing arbitrary samples.	Can probe any arbitrary surface of size from sub-micron to cm.

Table A.1 Comparison of Equal path interferometer with iLens interferometer.

Transmission Sphere (TS)	**iLens**
1. Used in Conjunction with an interferometer such as Fizeau Interferometer.	It is in itself is an interferometer when combined with a sample.
2. It's a combination of lenses. Generally made up of more than three pieces of lenses with spherical surfaces.	It's just one single lens from which the interference fringes are obtained.
3. Specially designed to test a concave or convex spherical surface only..	Suitable to test any given arbitrary rough surface.
4. The reflectivity of the surface has been fixed to 4% only.	The reflectivity may vary according to the sample under test. The various reference reflectivity values are shown in Table A.1.
5. The interference pattern result when the measurement wave front (reflected from the test surface) passes through the TS and into the interferometer where it interferes with the reference beam.	The iLens splits the incoming beam into two beams, reference beam and the object beam. It then collects the object beam reflected back from the sample surface, which then interferes with the reference beam to form interference fringes.
6. The sample size should be in between the radius of the TS and its focal point.	No such limitation.
7. A zoom feature in the interferometer is required for obtaining better results from TS.	It does not require any such feature.

Table A.2 Comparison of Equal path interferometer with iLens interferometer.

Appendix B

Theoretical verification of iLens interferometer

B.1 Theoretical verification of iLens interferometer

The Gaussian laser-beam interferometers are precision devices for various measurements. To exploit their full potential and to understand their operating mechanism, a through design analysis with Gaussian beam is necessary.

While standard interferometers design are based on either amplitude division or phase division, such as Michelson [1], Fabry-Perot [4], Mirau [5], Fizeau interferometer [6], etc. Some of these have been analyzed in detail with single or multiple Gaussian beams or with structured light, in particular for analyzing fringe contrast, precision, and error analysis.

Recently, we have designed a single iLens interferometer [60] and that was shown to produce universal fringes with most common (flat and rough) surfaces and offered a precision of $< 20pm$ in real time. However, a detailed analysis of iLens interferometer with Gaussian beam to theoretically understand the working range, role of iLens-to-sample distance, and fringe contrast was missing.

B.1.1 *ABCD* matrix method for paraxial beam propagation

A Gaussian beam propagating through different optical components can be analyzed using ABCD matrices. A linearly polarized Gaussian beam propagating along the z-axis is expressed as [144, 145]:

$$E_{in}(r,z) = E_0 \frac{w_0}{w(z)} \exp\left[-\frac{r^2}{w^2(z)}\right] \exp\left[-ikz + i\arctan\left(\frac{z}{z_0}\right)\right] \exp\left[-ik\frac{r^2}{2R(z)}\right] \quad \text{(B.1)}$$

where, $r = \sqrt{x^2+y^2}$; E_0 is field amplitude; z_0 is the Rayleigh range; and $w_0 = \sqrt{\frac{\lambda z_0}{\pi}}$; $w(z) = w_0\sqrt{1+\left(\frac{z}{z_0}\right)^2}$; $R(z) = z\left[1+\left(\frac{z_0}{z}\right)^2\right]$; are the beam waist, beam radius, and the radius of curvature of the wave front respectively.

The intensity of the Gaussian beam at a given point can be given by the square modulus of its electric field as:

$$I(r,z) = |E_0|^2 \left(\frac{w_0}{w(z)}\right)^2 \exp\left[-\frac{2r^2}{w^2(z)}\right]. \quad \text{(B.2)}$$

We will use the ABCD matrix formalism to describe the propagation of Gaussian beam through optical elements of iLens interferometer where each optical element is represented by a simple 2x2 ABCD matrix. The determinant of the matrix is unity, i.e. AD-BC=1, if the input and the output plane are in the same optical medium. For a lossless system, the matrix elements are real, but complex otherwise. The relation between the output (q2) and input (q1) complex beam parameter is expressed as:

$$\begin{pmatrix} q_2 \\ 1 \end{pmatrix} = \begin{pmatrix} A & B \\ C & D \end{pmatrix} \begin{pmatrix} q_1 \\ 1 \end{pmatrix} \quad \text{(B.3)}$$

The output complex beam parameter is determined using the matrix formalism as [146, 147]:

$$q_2 = \frac{Aq_1 + B}{Cq_1 + D} \quad \text{(B.4)}$$

The complex radius of curvature of the Gaussian beam propagating through the *ABCD* optical system transforms according to the *ABCD* law. However the product of the minimum beam width (ω_0) and the divergence of the beam (θ_0) remains invariant throughout the beam propagation given by

$$\omega_0\theta_0 = \frac{\lambda}{\pi}$$

In this paper our objective is to analyze the Gaussian beam propagation in our single-lens interferometer for detailed working for two cases of a flat sample surface and a rough sample

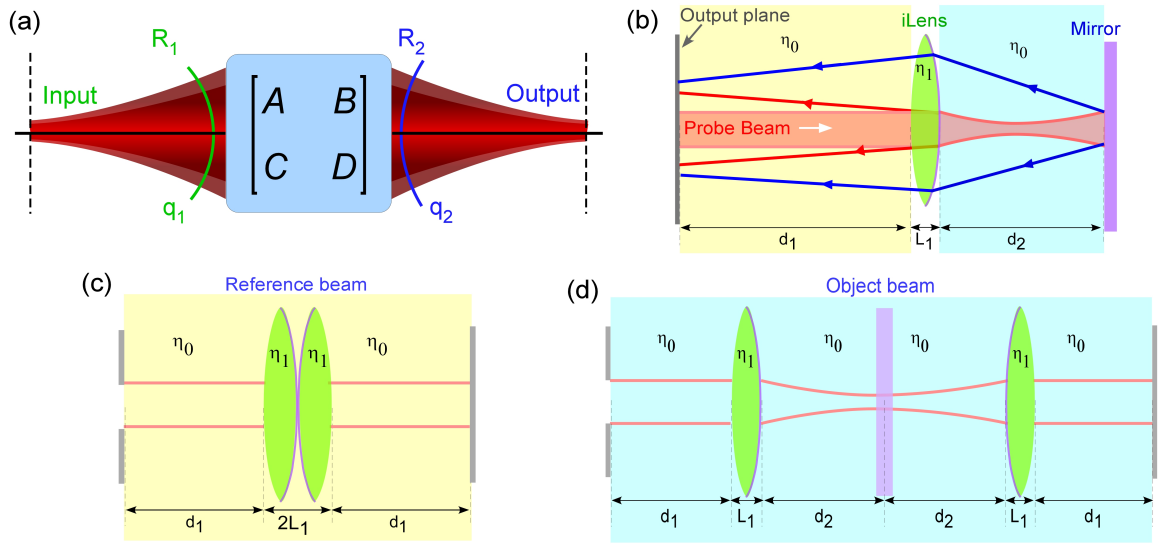

Fig. B.1 **ABCD analysis of iLens interferometer.** (a) Gaussian beam propagation through an optical system described by ABCD matrix. (b) schematics of iLens interferometer. (c) Beam propagation in the reference arm of the interferometer. (d) Propagation of beam in the object arm of the iLens interferometer.

surface using *ABCD* matrix formalism. An analysis of error and misalignment of sample tilt will be presented. We will validate our theoretical prediction with the experimental data.

Figure B.1(a) shows the Gaussian beam propagation through an optical system described by ABCD matrix. We consider the iLens of focal length f (radius of curvature R) and central thickness L_1 which is kept at a distance d_1 from the beam splitter (BS) on the optical axis of the system (see Figure B.1(b)). The rear surface of the iLens is coated with a beam splitter coating having T:R intensity coefficient, where, T stands for Transmission coefficient and R for Reflection coefficient. The plasma sample is placed at a distance d2 from the iLens. For the analysis of our system we have used the thin lens approximation i.e. the iLens thickness is much smaller than its focal length ($L_1 << f$).

B.1.2 Equivalent schematic of iLens interferometer for the reference and the object arm

The various optical elements used in our interferometer setup can be represented using ABCD matrices (Figure B.1(b)). The propagation path of input Gaussian beam through the reference and the object arms of the interferometer is shown in Figure B.1(c,d), respectively. The ABCD matrix for the various optical components of iLens system are given by:

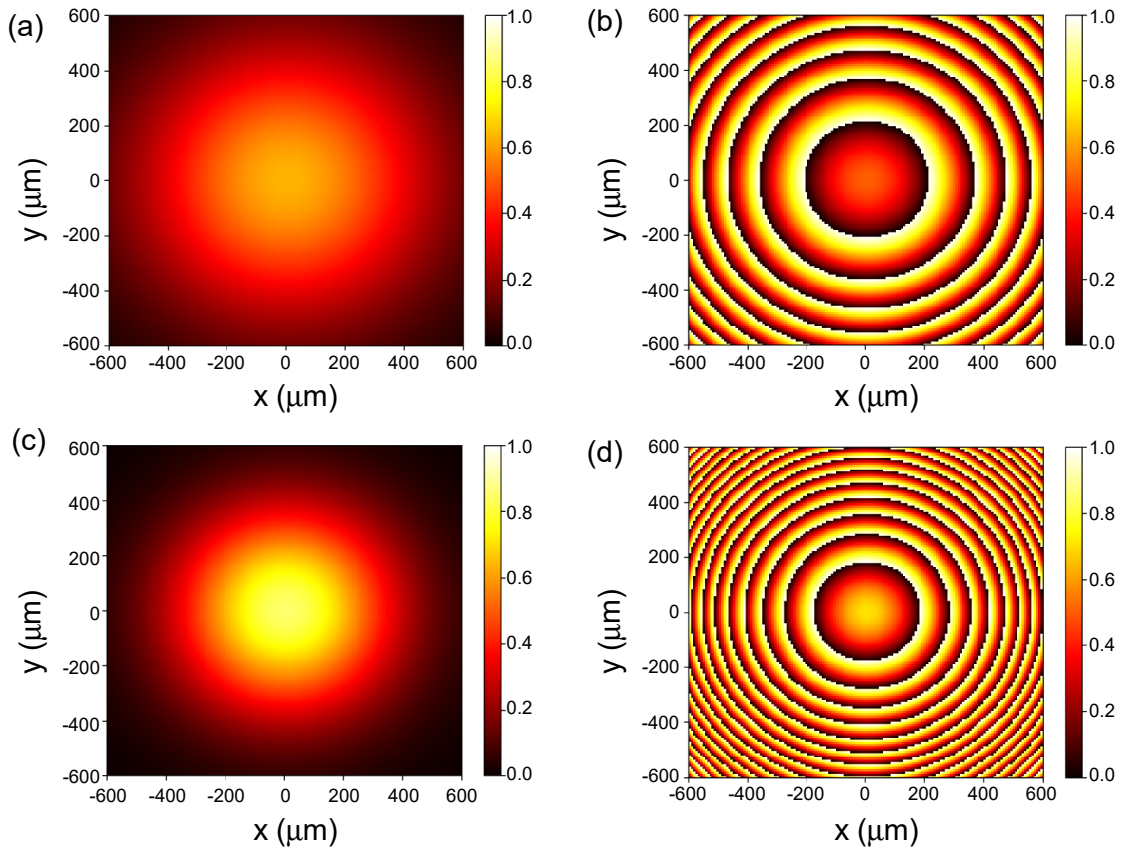

Fig. B.2 **Intensity and phase plots.** (a,b) Intensity and phase plot of the reference beam respectively, (c,d) Intensity and phase plot of the object beam respectively.

The free space propagation of the beam from BS to iLens is

$$M_1 = \begin{pmatrix} 1 & d_1 \\ 0 & 1 \end{pmatrix}$$

The matrix for thin lens approximation of iLens is

$$M_2 = \begin{pmatrix} 1 & 0 \\ -\frac{1}{f} & 1 \end{pmatrix}$$

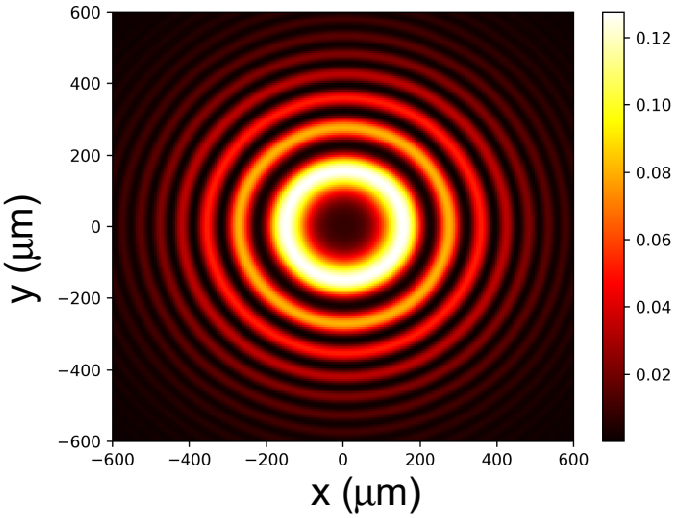

Fig. B.3 Interference fringes from flat surface.

The matrix for the beam reflected from the partially coated rear surface of the iLens (serving as a concave mirror) is:

$$M_3 = \begin{pmatrix} 1 & 0 \\ -\frac{2}{R} & 1 \end{pmatrix}$$

The free space propagation of the beam between iLens and sample is:

$$M_4 = \begin{pmatrix} 1 & d_2 \\ 0 & 1 \end{pmatrix}$$

The matrix M_4 is applicable if the sample under test is a smooth surface or a mirror. For a rough sample the matrix elements *B&C* will be complex numbers. The global matrix for the reference and the object arm is then given by:

$$M_{ref} = M_1 \times M_3 \times M_2 \times M_1 \tag{B.5}$$

$$M_{obj} = M_1 \times M_2 \times M_4 \times M_4 \times M_2 \times M_1 \tag{B.6}$$

The order in which the matrices are multiplied, to obtain the global matrix for each arm, is reversed when the Gaussian beam is propagated through the interferometer system. After the Gaussian beam (TEM_{00} mode) propagation through the system, the electric field of the beam from each arm is then superimposed to obtain fringes on the output plane. The electric field

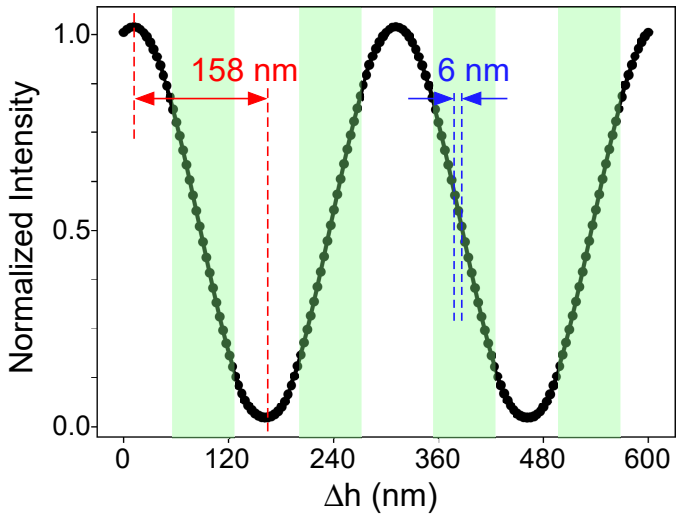

Fig. B.4 **Calibration curve of sample displacement in the z-direction.** The curve shows the collapse (or evolving) of two fringes at the center of the pattern by displacing the sample by one wavelength. The green shaded regions denote the linear regime of the interferometer.

of the reference arm $E_{ref}(x,y)$ and the object arm $E_{obj}(x,y)$ in the output plane (on screen) can be obtained using the transfer matrices Eq. (B.5)-(B.6). The interference intensity is then given by:

$$I = \left|E_{ref} + E_{obj}\right|^2 \tag{B.7}$$

B.1.3 Results

B.1.3.1 Electric field intensity and phase plots of the reference and the object beam

Figure B.2(a-d) shows the electric field intensity and the phase profile of the reference and the object beam at the screen respectively. The interference pattern obtained from these two beams consists of high contrast circular fringes as simulated in Figure B.3. We measure the single pixel intensity using a photodiode at the centre of the interference pattern which shows a cosine squared dependence shown in Figure B.4. The curve shows the collapse (or revival) of two fringes at the centre of the pattern when displacing the sample by a distance equal to one wavelength.

To establish the self-calibration of our setup [28] we gave an input displacement $\Delta h = h(t) - h(0)$ to the mirror using a nano-positioner and compared it with the corresponding shift in the interference intensity as shown in Figure B.4. The interference condition of half fringe collapse corresponding to $\Delta h = \lambda/4$, governs the self-calibration of our setup and is

independent of time scale at which interference fringes evolve or collapse. The intensity can be further resolved in sub-fringe regime to measure the nanometer resolved displacements by taking N intensity points in between the minima and maxima of the central fringe which elevates the precision of the interferometer to $\Delta h = \lambda/4N$. For example, in Figure B.4, $N = 50$ yields a precision as low as a few *nm* (3 *nm*). In an experiment, the actual resolution is determined by the intensity resolution of photodiode and oscilloscope system, which for a typical case of $N = 1000$, reaches picometer regime. The actual resolution of the device is limited by the experimental noise floor.

Appendix C

Python Program for noise self-compensating single-lens twisted interferometer

---

```
def sub(list1,list2):
   list3 = [x1-x2 for (x1,x2) in zip(list1,list2)]
   return list3

z=0.5*1e9
w0=0.3*1e6
r = np.linspace(0.0,1500*1e3,500)
theta=np.linspace(0.0, 2*np.pi,361)
l=3*np.ones_like(r)
p=0*np.ones_like(r)
R,THETA=np.meshgrid(r,theta)
l1=l[0]
p1=p[0]
A = np.sqrt(2*math.factorial(p1)/(np.pi*math.factorial(np.abs(l1)+p1)))
lamda=632.0
k= 2*np.pi/lamda
zr=np.pi*w0**2/lamda
Rz = z*((zr/z)**2 +1)
wz= w0*np.sqrt(1+(z**2/zr**2))
phi = np.pi*R**2/(lamda*Rz) - (np.abs(l)+(2*p)+1)*np.arctan(z/zr)
L = scipy.special.eval_genlaguerre(p,l,2*R**2/wz**2)
Rl=(1/wz)*((np.sqrt(2)*R/wz)**np.abs(l))*np.exp(-R**2/wz**2)*np.exp(1j*phi)*L
```

```
dh=0.0
dh2=0.0
N = 10
x_axis=[]
y_axis=[]
y_axis1=[]
h=0.0
h1 = 0.0

for i in range(0,N+1):

   h1+=dh
   h = h1
   dh2 = dh2 + (dh)
   x_axis.append(dh2)
   E1=(Rl)*np.exp(1j*(l*THETA+k*h))
   E2=(Rl)*np.exp(-1j*l*THETA)
   I1 = np.abs((E1 + E2)**2)
   I1 = I1/I1.max()

   fig = plt.figure(figsize=(10,8))
   ax = fig.add_subplot(111,polar=True)
   cb = ax.scatter(THETA, R,c=I, alpha=1, s=3, vmin=I1.min(), vmax=I1.max())
   xpix = I.shape[0]/361
   ypix = 1000*I.shape[1]/1500

   y_axis.append(I[90*xpix, ypix].mean())
    y_axis1.append(I[297*xpix, ypix].mean())
   diff = sub(y_axis,y_axis1)

   fig3,ax3 = plt.subplots(1,1)
   ax3.plot(x_axis,diff,linewidth=2.5,color='b')
```

References

[1] A. A. Michelson and E. W. Morley. Michelson-morleys experiment. *The London, Edinburgh, and Dublin Philosophical Magazine and Journal of Science*, 24:449, 1887.

[2] J Jamin. Neuer interferential-refractor. *Ann. Phys*, 98:345–349, 1856.

[3] L. Zehnder. Zeitachrift fur listrumentenkund6. *Zeitschr. F. Instrkde.*, 11:275, 1891.

[4] Gonzalo Hernández. *Fabry-perot interferometers*, volume 3. Cambridge University Press, 1988.

[5] Mirau Andre Henri. Interferometer, September 30 1952. US Patent 2,612,074.

[6] L. L. Deck, P. J. de Groot, and J. A. Soobitsky. Large-aperture, equal-path interferometer for precision measurements of flat transparent surfaces. *Appl. Opt.*, 53:1546, 2014.

[7] K. G. Libbrecht and E. D. Black. A basic michelson laser interferometer for the undergraduate teaching laboratory demonstrating picometer sensitivity. *Am. J. Phys.*, 83:409, 2015.

[8] B. P. Abbott, R. Abbott, T. D. Abbott, M. R. Abernathy, F. Acernese, K. Ackley, C. Adams, T. Adams, P. Addesso, R. X. Adhikari, and V. B. Adya. Observation of gravitational waves from a binary black hole merger. *Phys. Rev. Lett.*, 116:061102, 2016.

[9] E. D. Black, A. Villar, and K. G. Libbrecht. Thermoelastic-damping noise from sapphire mirrors in a fundamental-noise-limited interferometer. *Phys. Rev. Lett.*, 93:241101, 2004.

[10] Peter J de Groot. A review of selected topics in interferometric optical metrology. *Reports on Progress in Physics*, 82(5):056101, 2019.

[11] BP Abbott, R Abbott, R Adhikari, P Ajith, Bruce Allen, G Allen, RS Amin, SB Anderson, WG Anderson, MA Arain, et al. Ligo: the laser interferometer gravitational-wave observatory. *Reports on Progress in Physics*, 72(7):076901, 2009.

[12] W. J. Peng, C. F. Ho, W. L. Lin, Z. R. Yu, C. Y. Huang, C. H. Kuo, and W. Y. Hsu. Design, tolerance analysis, fabrication, and testing of a 6-in. dual-wavelength transmission sphere for a fizeau interferometer. *Opt. Eng.*, 56:035105, 2017.

[13] M. C. Shellabear and J. R. Tyrer. Application of espi to three-dimensional vibration measurements. *Opt. Lasers Eng.*, 15:43, 1991.

[14] Nandigana Krishna Mohan and Pramod Rastogi. Recent developments in digital speckle pattern interferometry, 2003.

[15] Bruno Pouet and Sridhar Krishnaswamy. Noise reduction techniques for electronic speckle interferometry. pages 435–442, 1993.

[16] D. A. Boas, D. H. Brooks, E. L. Miller, C. A. DiMarzio, M. Kilmer, R. J. Gaudette, and Q. Zhang. Imaging the body with diffuse optical tomography. *IEEE Signal Process. Mag.*, 18:57, 2001.

[17] Jaime Ortega-Arroyo and Philipp Kukura. Interferometric scattering microscopy (iscat): new frontiers in ultrafast and ultrasensitive optical microscopy. *Physical Chemistry Chemical Physics*, 14(45):15625–15636, 2012.

[18] V. Arroyo, D. Cole, and P. Kukura. Interferometric scattering microscopy and its combination with single-molecule fluorescence imaging. *Nat. Protoc.*, 11:617, 2016.

[19] G. Young, N. Hundt, D. Cole, A. Fineberg, J. Andrecka, A. Tyler, A. Olerinyova, A. Ansari, E. G. Marklund, M. P. Collier, and S. A. Chandler. Quantitative mass imaging of single biological macromolecules. *Science*, 360:423, 2018.

[20] AF Fercher, Hong Zhang Hu, and U Vry. Rough surface interferometry with a two-wavelength heterodyne speckle interferometer. *Applied optics*, 24(14):2181–2188, 1985.

[21] J. N. Butters and J. A. Leendertz. Holographic and video techniques applied to engineering measurement. *Meas. Control*, 12:349, 1971.

[22] J. C. Wyant. Computerized interferometric surface measurements. *Appl. Opt.*, 52:1, 2013.

[23] J. S. Cybulski, J. Clements, and M. Prakash. Foldscope: origami-based paper microscope. *PLoS One*, 9:e98781, 2014.

[24] M. S. Bhamla, B. Benson, C. Chai, G. Katsikis, A. Johri, and M. Prakash. Hand-powered ultralow-cost paper centrifuge. *Nat. Biomed. Eng.*, 1:9, 2017.

[25] A. W. Martinez, S. T. Phillips, and G. M. Whitesides. Three-dimensional microfluidic devices fabricated in layered paper and tape. *Proc. Natl. Acad. Sci. U. S. A.*, 105:19606, 2008.

[26] Max Born and Emil Wolf. *Principles of optics: electromagnetic theory of propagation, interference and diffraction of light*. Elsevier, 2013.

[27] G. Popescu and A. Dogariu. Optical path-length spectroscopy of wave propagation in random media. *Opt. Lett.*, 24:442, 1999.

[28] Hernan E Grecco and Oscar E Martínez. Calibration of subnanometer motion with picometer accuracy. *Applied optics*, 41(31):6646–6650, 2002.

[29] P. F. Forman. The zygo interferometer system. *Int. Soc. Opt. Photonics*, 192:41, 1979.

[30] Andres W Martinez, Scott T Phillips, George M Whitesides, and Emanuel Carrilho. Diagnostics for the developing world: microfluidic paper-based analytical devices, 2010.

[31] Andreas Metzger, Stephan Baltisberger, Hans-Rudolf Burkhard, Christophe Béguin, and Markus Uster. Weighing cell based on the principle of electromagnetic force compensation with optoelectronic position sensor, July 21 2015. US Patent 9,086,315.

[32] Y. T. Yang, C. Callegari, X. L. Feng, K. L. Ekinci, and M. L. Roukes. Zeptogram-scale nanomechanical mass sensing. *Nano Lett.*, 6:583, 2006.

[33] J. J. Li and K. D. Ka-Di Zhu. Plasmon-assisted mass sensing in a hybrid nanocrystal coupled to a nanomechanical resonator. *Phys. Rev. B*, 83:245421, 2011.

[34] T. P. Burg, M. Godin, S. M. Knudsen, W. Shen, G. Carlson, J. S. Foster, K. Babcock, and S. R. Manalis. Weighing of biomolecules, single cells and single nanoparticles in fluid. *Nature*, 446:1066, 2007.

[35] M. Eidini and G. H. Paulino. Unraveling metamaterial properties in zigzag-base folded sheets. *Sci. Adv.*, 1:e1500224, 2015.

[36] M. Antognozzi, C. R. Bermingham, R. L. Harniman, S. Simpson, J. Senior, R. Hayward, H. Hoerber, M. R. Dennis, A. Y. Bekshaev, K. Y. Bliokh, and F. Nori. Direct measurements of the extraordinary optical momentum and transverse spin-dependent force using a nano-cantilever. *Nat. Phys.*, 12:731, 2016.

[37] G. Sitters, D. Kamsma, G. Thalhammer, M. Ritsch-Marte, E. J. Peterman, and G. J. Wuite. Acoustic force spectroscopy. *Nat. Methods*, 12:47, 2015.

[38] J. L. Arlett, E. B. Myers, and M. L. Roukes. Comparative advantages of mechanical biosensors. *Nat. Nanotechnol.*, 6:203, 2011.

[39] V. Koskinen, J. Fonsen, K. Roth, and J. Kauppinen. Progress in cantilever enhanced photoacoustic spectroscopy. *Vib. Spectrosc.*, 48:16, 2008.

[40] FL Degertekin, B Hadimioglu, T Sulchek, and CF Quate. Actuation and characterization of atomic force microscope cantilevers in fluids by acoustic radiation pressure. *Applied Physics Letters*, 78(11):1628–1630, 2001.

[41] Massimo Antognozzi, CR Bermingham, RL Harniman, S Simpson, J Senior, R Hayward, H Hoerber, MR Dennis, AY Bekshaev, KY Bliokh, et al. Direct measurements of the extraordinary optical momentum and transverse spin-dependent force using a nano-cantilever. *Nature Physics*, 12(8):731–735, 2016.

[42] Shigeyoshi Osaki and Rie Ishikawa. Determination of elastic modulus of spider's silks. *Polymer journal*, 34(1):25–29, 2002.

[43] Jian Zhou and Ronald N Miles. Sensing fluctuating airflow with spider silk. *Proceedings of the National Academy of Sciences*, 114(46):12120–12125, 2017.

[44] Yong Yang, Xin Chen, Zhengzhong Shao, Ping Zhou, David Porter, David P Knight, and Fritz Vollrath. Toughness of spider silk at high and low temperatures. *Advanced Materials*, 17(1):84–88, 2005.

[45] Changyao Chen, Sunwoo Lee, Vikram V Deshpande, Gwan-Hyoung Lee, Michael Lekas, Kenneth Shepard, and James Hone. Graphene mechanical oscillators with tunable frequency. *Nature nanotechnology*, 8(12):923–927, 2013.

[46] Mehra S Sidhu, Bhupesh Kumar, and Kamal P Singh. The processing and heterostructuring of silk with light. *Nature materials*, 16(9):938–945, 2017.

[47] Joseph I Goldstein, Dale E Newbury, Joseph R Michael, Nicholas WM Ritchie, John Henry J Scott, and David C Joy. *Scanning electron microscopy and X-ray microanalysis*. Springer, 2017.

[48] Bertram Eugene Warren. *X-ray Diffraction*. Courier Corporation, 1990.

[49] Shaochen Chen, Costas P Grigoropoulos, Hee K Park, Pieter Kerstens, and Andrew C Tam. Photothermal displacement measurement of transient melting and surface deformation during pulsed laser heating. *Applied physics letters*, 73(15):2093–2095, 1998.

[50] Cheryl R Blanchard. Atomic force microscopy. *The chemical educator*, 1(5):1–8, 1996.

[51] Achim Hartschuh, Erik J Sánchez, X Sunney Xie, and Lukas Novotny. High-resolution near-field raman microscopy of single-walled carbon nanotubes. *Physical Review Letters*, 90(9):095503, 2003.

[52] Atsushi Wada, Makoto Kato, and Yukihiro Ishii. Multiple-wavelength digital holographic interferometry using tunable laser diodes. *Applied optics*, 47(12):2053–2060, 2008.

[53] Yong K Kim, B Rami Reddy, TG George, and Ravindra B Lal. Optical heterodyne interferometry technique for solution crystal growth rate measurement. *Optical Engineering*, 37, 1998.

[54] Toru Yoshizawa. *Handbook of optical metrology: Principles and Applications*. CRC Press, 2017.

[55] Fabrice Meriaudeau. Real time multispectral high temperature measurement: Application to control in the industry. *Image and Vision Computing*, 25(7):1124–1133, 2007.

[56] Carlton W Farley III and B Rami Reddy. Interferometric measurement of laser heating in praseodymium-doped yag crystal. *Applied optics*, 50(4):526–531, 2011.

[57] Mansoor Sheik-Bahae and Richard I Epstein. Laser cooling of solids. *Laser & Photonics Reviews*, 3(1-2):67–84, 2009.

[58] Denis V Seletskiy, Seth D Melgaard, Stefano Bigotta, Alberto Di Lieto, Mauro Tonelli, and Mansoor Sheik-Bahae. Laser cooling of solids to cryogenic temperatures. *Nature Photonics*, 4(3):161–164, 2010.

[59] Galina Nemova and Raman Kashyap. Laser cooling of solids. *Reports on Progress in Physics*, 73(8):086501, 2010.

[60] Pooja Munjal and Kamal P. Singh. A single-lens universal interferometer: Towards a class of frugal optical devices. *Applied Physics Letters*, 115(11):111102, 2019.

[61] AS Usmani, JM Rotter, S Lamont, AM Sanad, and Martin Gillie. Fundamental principles of structural behaviour under thermal effects. *Fire Safety Journal*, 36(8):721–744, 2001.

[62] BS Yilbas and N Al-Aqeeli. Analytical investigation into laser pulse heating and thermal stresses. *Optics & Laser Technology*, 41(2):132–139, 2009.

[63] Jorge N Hernandez-Charpak, Kathleen M Hoogeboom-Pot, Qing Li, Travis D Frazer, Joshua L Knobloch, Marie Tripp, Sean W King, Erik H Anderson, Weilun Chao, Margaret M Murnane, et al. Full characterization of the mechanical properties of 11–50 nm ultrathin films: Influence of network connectivity on the poisson's ratio. *Nano letters*, 17(4):2178–2183, 2017.

[64] H Kleimann, Y Fetiveau, M Richard, L Eyraud, C Eyraud, and J Elston. Thermal diffusivity of solids. Technical report, Institut National des Sciences Appliquees, 1969.

[65] Wing P Leung and Andrew C Tam. Thermal diffusivity in thin films measured by noncontact single-ended pulsed-laser-induced thermal radiometry. *Optics letters*, 9(3):93–95, 1984.

[66] HK Park, CP Grigoropoulos, and AC Tam. Optical measurements of thermal diffusivity of a material. *International journal of thermophysics*, 16(4):973–995, 1995.

[67] J Unsworth and FJ Duarte. Heat diffusion in a solid sphere and fourier theory: an elementary practical example. *American Journal of Physics*, 47(11):981–983, 1979.

[68] Shizuka Kawasaki, Yuichiro Yamashita, Nobuto Oka, Takashi Yagi, Junjun Jia, Naoyuki Taketoshi, Tetsuya Baba, and Yuzo Shigesato. Thermal boundary resistance of w/al2o3 interface in w/al2o3/w three-layered thin film and its dependence on morphology. *Japanese Journal of Applied Physics*, 52(6R):065802, 2013.

[69] Chan Kok Sheng, Mat Yunus, and W Mahmood. Thermal diffusivity measurement of the commercial papers using photoacoustic technique. *Pertanika J Sci & Technol*, 10(2):161–166, 2002.

[70] Mark Walker, Martin Gröger, Kirsten Schlüter, and Bernd Mosler. A bright spark: open teaching of science using faraday's lectures on candles. *Journal of chemical education*, 85(1):59, 2008.

[71] Michael Faraday. *The chemical History of a Candle: a course of lectures delivered before a juvenile audience at the royal institution*. Chatto & Windus, 1886.

[72] A Van Maaren, DS Thung, and L R H DE GOEY. Measurement of flame temperature and adiabatic burning velocity of methane/air mixtures. *Combustion Science and Technology*, 96(4-6):327–344, 1994.

[73] Madhuri Thakur, AL Vyas, and Chandra Shakher. Measurement of temperature and temperature profile of an axisymmetric gaseous flames using lau phase interferometer with linear gratings. *Optics and lasers in engineering*, 36(4):373–380, 2001.

[74] Chandra Shakher and Anil Kumar Nirala. A review on refractive index and temperature profile measurements using laser-based interferometric techniques. *Optics and Lasers in Engineering*, 31(6):455–491, 1999.

[75] Tomohiro Shirai. Phase difference enhancement with classical intensity interferometry. *Optics Communications*, 380:239–244, 2016.

[76] Harald Kleine, Hans Grönig, and Kazuyoshi Takayama. Simultaneous shadow, schlieren and interferometric visualization of compressible flows. *Optics and Lasers in Engineering*, 44(3-4):170–189, 2006.

[77] Depang Yan and Soyoung S Cha. Single-path interferometer for measuring fluid flows in real time with low-quality optics. *Optics and lasers in engineering*, 29(1):33–40, 1998.

[78] David L Reuss. Temperature measurements in a radially symmetric flame using holographic interferometry. *Combustion and Flame*, 49(1-3):207–219, 1983.

[79] G Paul Montgomery and DL Reuss. Effects of refraction on axisymmetric flame temperatures measured by holographic interferometry. *Applied optics*, 21(8):1373–1380, 1982.

[80] Shobhna Sharma, Gyanendra Sheoran, and Chandra Shakher. Digital holographic interferometry for measurement of temperature in axisymmetric flames. *Applied optics*, 51(16):3228–3235, 2012.

[81] N Barakat, H El-Ghandoor, AM Hamed, and S Diab. Refractive index profiling across a candle flame using speckle techniques. *Experiments in fluids*, 16(1):42–45, 1993.

[82] V Bergmann, W Meier, D Wolff, and W Stricker. Application of spontaneous raman and rayleigh scattering and 2d lif for the characterization of a turbulent ch4/h2/n2 jet diffusion flame. *Applied Physics B*, 66(4):489–502, 1998.

[83] Christian Brackmann, Joakim Bood, Per-Erik Bengtsson, Thomas Seeger, Martin Schenk, and Alfred Leipertz. Simultaneous vibrational and pure rotational coherent anti-stokes raman spectroscopy for temperature and multispecies concentration measurements demonstrated in sooting flames. *Applied optics*, 41(3):564–572, 2002.

[84] Jean-Michel Desse, Pascal Picart, and Patrice Tankam. Digital three-color holographic interferometry for flow analysis. *Optics express*, 16(8):5471–5480, 2008.

[85] KB Sahu, A Kundu, R Ganguly, and A Datta. Effects of fuel type and equivalence ratios on the flickering of triple flames. *Combustion and Flame*, 156(2):484–493, 2009.

[86] DL Dietrich, HD Ross, Y Shu, P Chang, and JS T'ien. Candle flames in non-buoyant atmospheres. *Combustion science and technology*, 156(1):1–24, 2000.

[87] H Sato, K Amagai, and M Arai. Flickering frequencies of diffusion flames observed under various gravity fields. *Proceedings of the Combustion institute*, 28(2):1981–1987, 2000.

[88] Pooja Munjal and Kamal P Singh. Optically probing picometer-resolved photodynamics of solid surfaces. *URSI Radio Science Bulletin*, 2019(370):12–16, 2019.

[89] AM Hamed, F Sharaf, and H El-Ghandoor. Study of the refractive index distribution of air around a candle flame. *Optics & Laser Technology*, 25(2):113–116, 1993.

[90] Gopal Verma, James Nair, and Kamal P Singh. Comment on "low-power laser deformation of an air-liquid interface". *Physical review letters*, 110(7):079401, 2013.

[91] Gopal Verma and Kamal P Singh. Universal long-range nanometric bending of water by light. *Physical review letters*, 115(14):143902, 2015.

[92] Gopal Verma and Kamal P Singh. Time-resolved interference unveils nanoscale surface dynamics in evaporating sessile droplet. *Applied Physics Letters*, 104(24):244106, 2014.

[93] Olivier Emile and Janine Emile. Naked eye picometer resolution in a michelson interferometer using conjugated twisted beams. *Optics letters*, 42(2):354–357, 2017.

[94] Alberto Gatto, Matteo Tacca, F Kéfélian, C Buy, and M Barsuglia. Fabry-pérot-michelson interferometer using higher-order laguerre-gauss modes. *Physical Review D*, 90(12):122011, 2014.

[95] Erika D'Ambrosio. Nonspherical mirrors to reduce thermoelastic noise in advanced gravitational wave interferometers. *Physical Review D*, 67(10):102004, 2003.

[96] Benoît Mours, Edwige Tournefier, and Jean-Yves Vinet. Thermal noise reduction in interferometric gravitational wave antennas: using high order tem modes. *Classical and Quantum Gravity*, 23(20):5777, 2006.

[97] A Allocca, Alberto Gatto, Matteo Tacca, RA Day, Matteo Barsuglia, Gabriel Pillant, C Buy, and Gabriele Vajente. Higher-order laguerre-gauss interferometry for gravitational-wave detectors with in situ mirror defects compensation. *Physical Review D*, 92(10):102002, 2015.

[98] Liping Zhou, Jianghong Gan, Xiaojun Liu, Long Xu, and Wenlong Lu. Speckle-noise-reduction method of projecting interferometry fringes based on power spectrum density. *Applied optics*, 51(29):6974–6978, 2012.

[99] P Coullet, L Gil, and F Rocca. Optical vortices. *Optics Communications*, 73(5):403–408, 1989.

[100] Les Allen, Marco W Beijersbergen, RJC Spreeuw, and JP Woerdman. Orbital angular momentum of light and the transformation of laguerre-gaussian laser modes. *Physical review A*, 45(11):8185, 1992.

[101] S. Fürhapter, A. Jesacher, S. Bernet, and M. Ritsch-Marte. Spiral interferometry. *Opt. Lett.*, 30:1953, 2005.

[102] M. Padgett, J. Courtial, and L. Allen. Light's orbital angular momentum. *Phys. Today*, 57:35, 2004.

[103] M. Ritsch-Marte. Orbital angular momentum light in microscopy. *Philos. Trans. R. Soc., A*, 375:20150437, 2017.

[104] Jianjun Guo, Banghong Guo, Ronghua Fan, Wenjie Zhang, Yu Wang, Litao Zhang, and Panpan Zhang. Measuring topological charges of laguerre–gaussian vortex beams using two improved mach–zehnder interferometers. *Optical Engineering*, 55(3):035104, 2016.

[105] HI Sztul and RR Alfano. Double-slit interference with laguerre-gaussian beams. *Optics letters*, 31(7):999–1001, 2006.

[106] Olivier Emile and Janine Emile. Young's double-slit interference pattern from a twisted beam. *Applied Physics B*, 117(1):487–491, 2014.

[107] Hernan E Grecco and Oscar E Martínez. Calibration of subnanometer motion with picometer accuracy. *Applied optics*, 41(31):6646–6650, 2002.

[108] Zhen Qiao, Guoqiang Xie, Yuhang Wu, Peng Yuan, Jingui Ma, Liejia Qian, and Dianyuan Fan. Generating high-charge optical vortices directly from laser up to 288th order. *Laser & Photonics Reviews*, 12(8):1800019, 2018.

[109] Tommaso Baldacchini, James E Carey, Ming Zhou, and Eric Mazur. Superhydrophobic surfaces prepared by microstructuring of silicon using a femtosecond laser. *Langmuir*, 22(11):4917–4919, 2006.

[110] Milton Birnbaum. Semiconductor surface damage produced by ruby lasers. *Journal of Applied Physics*, 36(11):3688–3689, 1965.

[111] HM Van Driel, JE Sipe, and Jeff F Young. Laser-induced periodic surface structure on solids: a universal phenomenon. *Physical Review Letters*, 49(26):1955, 1982.

[112] V Zorba, E Stratakis, M Barberoglou, E Spanakis, P Tzanetakis, and C Fotakis. Tailoring the wetting response of silicon surfaces via fs laser structuring. *Applied Physics A*, 93(4):819, 2008.

[113] Niki Koufaki, Anthi Ranella, Katerina E Aifantis, Marios Barberoglou, Stylianos Psycharakis, Costas Fotakis, and Emmanuel Stratakis. Controlling cell adhesion via replication of laser micro/nano-textured surfaces on polymers. *Biofabrication*, 3(4):045004, 2011.

[114] Yuji Sato, Masahiro Tsukamoto, Togo Shinonaga, and Takuya Kawa. Femtosecond laser-induced periodic nanostructure creation on pet surface for controlling of cell spreading. *Applied Physics A*, 122(3):184, 2016.

[115] Valdemar Stankevič, Gediminas Račiukaitis, Francesca Bragheri, Xuewen Wang, Eugene G Gamaly, Roberto Osellame, and Saulius Juodkazis. Laser printed nanogratings: orientation and period peculiarities. *Scientific reports*, 7(1):1–8, 2017.

[116] Zeming Liu, Jan Siegel, Mario Garcia-Lechuga, Thierry Epicier, Yaya Lefkir, Stéphanie Reynaud, Matthieu Bugnet, Francis Vocanson, Javier Solis, Guy Vitrant, et al. Three-dimensional self-organization in nanocomposite layered systems by ultrafast laser pulses. *ACS nano*, 11(5):5031–5040, 2017.

[117] Anatoliy Y Vorobyev, VS Makin, and Chunlei Guo. Brighter light sources from black metal: significant increase in emission efficiency of incandescent light sources. *Physical review letters*, 102(23):234301, 2009.

[118] J Ouyang, W Perrie, OJ Allegre, T Heil, Y Jin, E Fearon, D Eckford, SP Edwardson, and G Dearden. Tailored optical vector fields for ultrashort-pulse laser induced complex surface plasmon structuring. *Optics express*, 23(10):12562–12572, 2015.

[119] Qiwen Zhan and James R Leger. Focus shaping using cylindrical vector beams. *Optics Express*, 10(7):324–331, 2002.

[120] KK Anoop, A Rubano, R Fittipaldi, X Wang, D Paparo, A Vecchione, L Marrucci, R Bruzzese, and S Amoruso. Femtosecond laser surface structuring of silicon using optical vortex beams generated by a q-plate. *Applied Physics Letters*, 104(24):241604, 2014.

[121] Jörn Bonse, Jörg Krüger, S Höhm, and A Rosenfeld. Femtosecond laser-induced periodic surface structures. *J. Laser Appl*, 24(4):042006, 2012.

[122] A Ya Vorobyev and Chunlei Guo. Colorizing metals with femtosecond laser pulses. *Applied Physics Letters*, 92(4):041914, 2008.

[123] Evangelos Skoulas, Alexandra Manousaki, Costas Fotakis, and Emmanuel Stratakis. Biomimetic surface structuring using cylindrical vector femtosecond laser beams. *Scientific reports*, 7(1):1–11, 2017.

[124] Martin E Fermann, Almantas Galvanauskas, and Gregg Sucha. *Ultrafast lasers: technology and applications*, volume 80. CRC Press, 2002.

[125] Frank A Müller, Clemens Kunz, and Stephan Gräf. Bio-inspired functional surfaces based on laser-induced periodic surface structures. *Materials*, 9(6):476, 2016.

[126] A Borowiec and HK Haugen. Subwavelength ripple formation on the surfaces of compound semiconductors irradiated with femtosecond laser pulses. *Applied Physics Letters*, 82(25):4462–4464, 2003.

[127] Mindaugas Gedvilas, Justinas Mikšys, and Gediminas Račiukaitis. Flexible periodical micro-and nano-structuring of a stainless steel surface using dual-wavelength double-pulse picosecond laser irradiation. *RSC Advances*, 5(92):75075–75080, 2015.

[128] Anne-Marie Kietzig, Savvas G Hatzikiriakos, and Peter Englezos. Patterned superhydrophobic metallic surfaces. *Langmuir*, 25(8):4821–4827, 2009.

[129] Marcus Ardron, Nick Weston, and Duncan Hand. A practical technique for the generation of highly uniform lipss. *Applied surface science*, 313:123–131, 2014.

[130] Susanta Kumar Das, Kiran Dasari, Arkadi Rosenfeld, and Ruediger Grunwald. Extended-area nanostructuring of tio2 with femtosecond laser pulses at 400 nm using a line focus. *Nanotechnology*, 21(15):155302, 2010.

[131] Sandra Höhm, Arkadi Rosenfeld, Jörg Krüger, and Jörn Bonse. Laser-induced periodic surface structures on titanium upon single-and two-color femtosecond double-pulse irradiation. *Optics express*, 23(20):25959–25971, 2015.

[132] Olga Varlamova, Christian Martens, Markus Ratzke, and Juergen Reif. Genesis of femtosecond-induced nanostructures on solid surfaces. *Applied optics*, 53(31):I10–I15, 2014.

[133] Jörn Bonse, Sandra Höhm, Sabrina V Kirner, Arkadi Rosenfeld, and Jörg Krüger. Laser-induced periodic surface structures—a scientific evergreen. *IEEE Journal of selected topics in quantum electronics*, 23(3), 2016.

[134] Jürgen Reif, Florenta Costache, Matthias Henyk, and Stanislav V Pandelov. Ripples revisited: non-classical morphology at the bottom of femtosecond laser ablation craters in transparent dielectrics. *Applied Surface Science*, 197:891–895, 2002.

[135] Jörn Bonse and Jörg Krüger. Pulse number dependence of laser-induced periodic surface structures for femtosecond laser irradiation of silicon. *Journal of Applied Physics*, 108(3):034903, 2010.

[136] JE Sipe, Jeff F Young, JS Preston, and HM Van Driel. Laser-induced periodic surface structure. i. theory. *Physical Review B*, 27(2):1141, 1983.

[137] Florence Garrelie, Jean-Philippe Colombier, Florent Pigeon, Svetlen Tonchev, Nicolas Faure, Mourad Bounhalli, Stéphanie Reynaud, and Olivier Parriaux. Evidence of surface plasmon resonance in ultrafast laser-induced ripples. *Optics Express*, 19(10):9035–9043, 2011.

[138] Ričardas Buividas, Mindaugas Mikutis, and Saulius Juodkazis. Surface and bulk structuring of materials by ripples with long and short laser pulses: Recent advances. *Progress in Quantum Electronics*, 38(3):119–156, 2014.

[139] Lei Wang, Bin-Bin Xu, Xiao-Wen Cao, Qian-Kun Li, Wen-Jing Tian, Qi-Dai Chen, Saulius Juodkazis, and Hong-Bo Sun. Competition between subwavelength and deep-subwavelength structures ablated by ultrashort laser pulses. *Optica*, 4(6):637–642, 2017.

[140] Thibault J-Y Derrien, Tatiana E Itina, Rémi Torres, Thierry Sarnet, and Marc Sentis. Possible surface plasmon polariton excitation under femtosecond laser irradiation of silicon. *Journal of Applied Physics*, 114(8):083104, 2013.

[141] JM Pitarke, VM Silkin, EV Chulkov, and PM Echenique. Theory of surface plasmons and surface-plasmon polaritons. *Reports on progress in physics*, 70(1):1, 2006.

[142] Yasuhiko Shimotsuma, Peter G Kazansky, Jiarong Qiu, and Kazuoki Hirao. Self-organized nanogratings in glass irradiated by ultrashort light pulses. *Physical review letters*, 91(24):247405, 2003.

[143] Lei Wang, Qi-Dai Chen, Xiao-Wen Cao, Ričardas Buividas, Xuewen Wang, Saulius Juodkazis, and Hong-Bo Sun. Plasmonic nano-printing: large-area nanoscale energy deposition for efficient surface texturing. *Light: Science & Applications*, 6(12):e17112–e17112, 2017.

[144] Muzammil A Arain and Guido Mueller. On the interference of two gaussian beams and their abcd matrix representation. *Optics Express*, 17(21):19181–19189, 2009.

[145] Harold T Yura and Steen Grüner Hanson. Optical beam wave propagation through complex optical systems. *JOSA A*, 4(10):1931–1948, 1987.

[146] Shixin Pei, Shanshan Xu, Fenping Cui, Qingwei Pan, and Zhaolou Cao. Propagation of a bessel–gaussian beam in a gradient-index medium. *Applied Optics*, 58(4):920–926, 2019.

[147] Herwig Kogelnik and Tingye Li. Laser beams and resonators. *Applied optics*, 5(10):1550–1567, 1966.